

AMERICAN UNIVERSITY OF BEIRUT

NANO-SIZED FABRIC PRODUCED BY ELECTROSPINNING
FOR CLOTHING PROTECTION, VENTILATION AND
COMFORT

by
NAGHAM BILAL ISMAIL

A dissertation
submitted in partial fulfillment of the requirements
for the degree of Doctor of Philosophy
to the Department of Mechanical Engineering
of the Faculty of Engineering and Architecture
at the American University of Beirut

Beirut, Lebanon
April 2017


AMERICAN UNIVERSITY OF BEIRUT

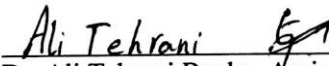
NANO-SIZED FABRIC PRODUCED BY ELECTROSPINNING FOR
CLOTHING PROTECTION, VENTILATION AND COMFORT


by
NAGHAM BILAL ISMAIL


Approved by:



Dr. Nesreen Ghaddar, Professor Advisor
Department of Mechanical Engineering, AUB


Dr. Kamel Ghali, Professor Member of Committee
Department of Mechanical Engineering, AUB


Dr. Ali Tehrani Bagha, Assistant Professor Member of Committee
Department of Chemical Engineering, AUB


Dr. Mohammad Ahmad, Professor Member of Committee
Department of Chemical Engineering, AUB


Dr. Khalil Khoury, Professor Member of Committee
Department of Mechanical Engineering, LU


Dr. Assaad Zoughalb, Professor Member of Committee
Department of Mechanical Engineering, ENSNP

Date of thesis/dissertation defense: [April 21, 2017]

AMERICAN UNIVERSITY OF BEIRUT

THESIS, DISSERTATION, PROJECT RELEASE FORM

Student Name:

Ismail

Nagham

Bilal

Master's Thesis
Dissertation

Master's Project

Doctoral

I authorize the American University of Beirut to: (a) reproduce hard or electronic copies of my thesis, dissertation, or project; (b) include such copies in the archives and digital repositories of the University; and (c) make freely available such copies to third parties for research or educational purposes.

I authorize the American University of Beirut, to: (a) reproduce hard or electronic copies of it; (b) include such copies in the archives and digital repositories of the University; and (c) make freely available such copies to third parties for research or educational purposes after: **One ---- year from the date of submission of my thesis, dissertation, or project.**
Two ---- years from the date of submission of my thesis, dissertation, or project.
Three ---- years from the date of submission of my thesis, dissertation, or project.

Signature

Date

ACKNOWLEDGMENTS

I would like to thank my advisor Prof. Nesreen Ghaddar, co-adviser Prof. Kamel Ghali, Prof. Ali Tehrani for their guidance and support throughout my research work. I had the chance to benefit from their research experience and critical thinking. I would like also to thank the members of my dissertation committee Prof. Assad Zouhaib, Prof. Khalil Khoury, and Prof. Mohamad Ahmad for their valuable comments and recommendations and the faculty members and staff of the Mechanical Engineering Department at the American University of Beirut for their help in the achievement of this work. Furthermore, I would like to thank Prof. Issam Lakkis for his guidance, Prof. Ghanem Oueis, Dr. Hussein Tarhini, Prof. Marwan Darwich for their valuable help.

I am also very grateful to all the lab staff that have taken some time to help me in achieving all the experimental work. They have provided me with a very stimulating environment, and that experience will leave marks beyond this thesis.

I would also like to express cordial gratitude to my colleagues and friends at the American University of Beirut who motivated me to achieve my goal: Carine Habchi, Hanin Hamdan, Alain Makhoul, Mohammad Allouche, Mohammad Baassiri, Mohammad Kanaan, Amer Keblawi, Abed AlKader Al Saidi, Maryam Itani, Manar Younes, Hussein Daoud, Douaa Al Assaad, Abed Saidi, Hajar Fawaz, Hussein Maanieh, Khaled Abou Hweij, Khalid and Walid Abou Hweij, Albert Touma, Omar Hatoum, Mohamad Hout, Jessica Daaboul, and Mohammad Bassel Kazzaz.

Furthermore, I would like to thank all my friends outside AUB: Sara Hajj Chehade, Hussein Ali Hussein, Omar Youness, Samer Youness, Mordiyya Chamaa, Mohamad Hussein, Amani Hajj, Khadija Hajj, Amani Abdallah, Zakaria and Yehia Hajj Hassan ...

Special thanks to my family, my family in law (Mohamad Youness and Nawal saad), my aunts Siham Khatib and Diba Ismail, my uncles Darwich Ismail, Mohamad Ismail, Abed Khatib, Ali Khatib, and Mohamad Khatib. Your presence has always been a source of joy and inspiration, and your empathy is highly appreciated. Words cannot express how appreciative I am for your help and care. Kassem, you were always a major source of support when things would get a bit discouraging, Hala and Yamen you have given me valuable motivation. Mom, thanks for always being there by my side, thanks for all the sacrifices you have made on my behalf.

At the end, I would like to express my appreciation and love to my husband Ali Youness who was always my support in the hard times. I appreciate your understanding, patience and being by my side to achieve our goal successfully.

The last word goes for Hamoudi, my baby boy, who has been the light of my life for the last year and who has given me the extra strength and motivation to get things done.

This PhD is dedicated to the memory of my father Bilal Kassem Ismail.

AN ABSTRACT OF THE DISSERTATION OF

Nagham Bilal Ismail for Doctor of Philosophy
Major: Mechanical Engineering

Title: Nano-sized fabric produced by electrospinning for clothing protection, ventilation and comfort

Conventional protective clothing used to prevent the exposure of workers to hazardous aerosol particles subjects the worker to heat stress because of the low air permeability which reduces clothing air ventilation. A compromise between high contaminant impermeability, and relatively high air permeability is well established by the nanotechnology. Indeed, nanotechnology includes the use of nano-sized materials for fabricating very thin fibers capable of forming a highly porous mesh characterized by a large surface-to-volume ratio to improve the clothing protection for better worker comfort. The fabrication of nanofibers is achieved by the electrospinning process which consists of producing nanofibers fabric by subjecting a polymer solution to an electric field. The nanofiber web produced presents high filtration efficiency and relatively high air permeability (significant ventilation). By varying the processing parameters of electrospinning such as the polymer concentration, the electric field, the time of electrospinning, and the volumetric flow rate, the properties of electrospun fibers can be manipulated. These properties such as the fiber diameter, the fiber thickness, and the porosity affected the filtration performance of the filter as well as its air permeability at some air face velocity. Therefore, optimization of electrospinning process for producing nanoweb with desirable air permeability by investigating the effect of electrospinning parameters on the air permeability presents a great interest. The reason is that this optimization will actually prevents the time cost in investigating the air permeability and the morphology of the nanofiber web, to come up with the desirable filtration efficiency without affecting the wearer thermal comfort. This is achieved by developing a systematic model that relates the electrospinning processing parameters to (i) the filtration of aerosol particles through the electrospun nanofiber for a range of particle diameter and face velocity and to (ii) the air ventilation of the electrospun nanofiber protective clothing. The ventilation model depends on the air permeability of the electrospun fabric and is based on an analogy between the air flow and an electric circuit composed of resistance and inductance. The resistance accounts for the viscous effect due to the air flow inside the microclimate air layer gap while the inductance represents the change of the air flow rate due to pumping/bellows effect resulting from body movements that force the air to enter/leave the microclimate air layer zone. The validation is achieved by conducting several experiments on the electrospinning device to produce the nanofiber web and on the thermal manikin using the tracer gas method to estimate the air ventilation and the segmental heat losses.

CONTENTS

ACKNOWLEDGEMENTS	v
ABSTRACT.....	vi
CONTENTS.....	vii
LIST OF ILLUSTRATIONS	x
LIST OF TABLES.....	xiv

Chapter

I. INTRODUCTION.....	1
II. METHODOLOGY.....	4
..	
A. Simplified modeling of the electrospinning process from stable jet region to unstable region to predict final nano-fiber diameter	6
1. Literature review.....	6
2. Mathematical formulation.....	8
a. Basic equations	8
b. Numerical Solution.....	14
3. Experimental methodology.....	15
a. Materials	15
b. Preparation PAN nanofibers.....	15
c. Electric current measurement.....	15
d. Measuring fiber diameter.....	15
B. Study the effect of processing parameters on the performance of nanofiber filtration efficiency and morphology	17
1. Literature review.....	17
2. Mathematical formulation.....	19

a. Porosity	19
b. Thickness and air permeability.....	20
c. Air filtration model.....	21
3. Experimental approach.....	22
a. Thickness measurement.....	22
b. Thickness measurement	23
c. Air permeability	23
d. Air filtration.....	24
C. Modeling the ventilation of the upper human body part by solving the governing equations inside the microclimate air layer	25
1. Literature review.....	25
2. Mathematical formulation.....	27
a. Clothed Upper Human Body Simplified Mathematical Model.....	29
b. Experimental methodology.....	37
D. Simplified Model of Ventilation and heat losses using an electric circuit analogy	45
1. Literature review.....	45
2. Mathematical formulation.....	47
a. Independent clothed segment.....	48
b. Inter-connected clothed upper human body	54
c. Electric circuit analogy of the heat model	64
3. Experimental methodology.....	70
III. RESULTS AND DISCUSSIONS.....	75
A. Prediction of the fiber diameter	75
1. Effect of flow rate on fiber diameter	77
2. Effect of electric field on fiber diameter.....	78
3. Effect of polymer concentration on fiber diameter.....	78
4. Model validation with published experimental study.....	79
5. Model comparison with published experimental study.....	79
6. Model limitation.....	80
B. Prediction of the web morphology.....	80

1. Effect of processing parameters on porosity and thickness.....	81
a. Electrospinning time.....	81
b. Processing parameters	81
2. Effect of processing parameters on air permeability and filtration	84
a. Electrospinning time.....	84
b. Processing parameters	85
3. Design charts correlation	89
C. Prediction of the ventilation through clothing	93
1. CFD validation.....	93
a. Flow direction validation.....	93
b. Temperature validation	91
2. Model validation with published experimental data.....	99
3. Parametric study	101
4. Experimental validation of IS using bio-heat model.....	106
D. Electric Analogy of the ventilation through clothing.....	113
1. Independent clothed segment.....	113
2. Inter-connected clothed segments.....	122
3. Limitations and recommendations	125
4. Incorporating of natural convection effect.....	127
a. Model validation with experiment.....	127
a. Parametric study	133
 BIBLIOGRAPHY.....	 136

ILLUSTRATIONS

Figure		Page
1.	Flow chart of the complete methodology.....	5
2.	Schematic of the experimental set-up for electrospinning.....	8
3.	Physical model of the electrospinning process (a) stable jet (b) bending instability.....	10
4.	The forces applied to the chosen control volume.....	11
5.	Flow chart of the complete model.....	16
6.	Electrospinning device used.....	17
7.	SEM images chosen as examples for the following processing parameters (Q=900 μ l/hr, E=97222 V/m, C=10% and te=6 hours) showing the measurement of (a) fiber diameter (b) nanofiber web thickness.....	24
8.	Schematic of air filtration experiment.....	25
9.	Physical configuration of the upper part of the human body.....	28
10.	Blow up of the clothed segments.....	29
11.	Plots of (a) front and top view of the upper human body and (b) symmetrical part of the domain that was simulated by ANSYS ..	35
12.	Flow chart of the integration methodology	36
13.	Test set up of the manikin (a) using two large fans and (b) using a testing jacket (c) showing the velocity distribution in m/s at a distance of 0.35 m from the manikin surface	38
14.	Schematic diagram of the experimental set up	41
15.	Schematic diagram of the three unknown parameters	43
16.	Physical configuration of (a) disconnected upper human body segments (b) fabric clothed segment	49

17.	Network representing the analogy of the air flow inside the microclimate air layer of (a) clothed oscillating arm (b) clothed trunk subjected to external wind.....	54
18.	The physical configuration of the upper human body part showing (a) 3 D representation blowing up the clothed segments (b) front view and (c) back view.....	56
19.	Network representing the analogy of the air flow inside the microclimate air layer of clothed upper human body for (a) the front side and (b) the back side.....	58
20.	Schematic of (a) different mechanisms of heat transfer from the independent segment representing the trunk (b) thermal resistance network.....	63
21.	Schematic of thermal resistance network of the shoulder zone	64
22.	Electric circuit composed of inductance, resistance and source of voltage in series.....	66
23.	Network representing the analogy of the air flow inside the microclimate air layer of clothed arm subjected to external wind and oscillating motion taking into account the natural convection....	66
24.	Schematic of (a) different mechanisms of heat transfer from the human body (b) thermal resistance network	67
25.	Schematic of the experimental set up to measure the ventilation of the front side for (a) the clothed trunk and (b) the clothed arm	73
26.	Figures showing (a) the experimental set up (b) the manikin shirt (c) the walking thermal manikin and (d) the argon tank with its flow controller	74
27.	Comparison between theoretical and experimental fiber diameter for (a) different flow rates (b) different electric field (c) different concentrations.....	77
28.	Experimental and theoretical effect of electrospinning time on the porosity and thickness of the nanofiber web	81
29.	Effect of (a) flow rate (b) electric field (c) concentration on porosity and thickness at the nanofiber web.....	83
30.	Effect of the fiber diameter on nanofiber web thickness and porosity.....	84

31.	Effect of electrospinning time on (a) air permeability (b) aerosol filtration for different particle diameters	86
32.	Effect of (a) flow rate (b) electric field (c) concentration on air permeability and filtration efficiency.....	88
33.	Effect of fiber diameter on air permeability and filtration efficiency.....	89
34.	Design chart of the fiber diameter as function of flow rate and electric field at polymer concentration of (a) 8% and (b) 10 %	91
35.	Design chart of the porosity over the thickness as function of fiber diameter for different time of electrospinning	92
36.	Design chart of the air permeability and filtration efficiency as function of porosity over thickness at different fiber	92
37.	CFD simulation plots of the flow (a) leaving the open top of clothed trunk (b) leaving and entering the open bottom clothed arm (c) through the connection	95
38.	Validation of the velocity field (a) leaving the open top of clothed trunk (b) leaving and entering the open bottom clothed arm (c) through the connection.....	96
39.	Distribution of the relative pressure obtained from CFD simulation.....	97
40.	Angular-averaged axial temperature validation obtained from the ventilation model at (a) zone Z1 (b) at zone Z2 (c) at zone Z3 (d) at zone Z4	98
41.	Estimation of the inter-segmental ventilation obtained from the ventilation model as a function of (a) wind speed (b) permeability (c) apertures.....	103
42.	Comparison between the analytical and experimental ventilations in (a) case 1 of low permeable clothing (b) case 2 of high permeable clothing	107

43.	Inter-segmental ventilation (l/min) parity plot for case (a) open bottom and open top (b) closed bottom and open top (c) open bottom and closed top	112
44.	Comparison between the ventilation obtained by the simplified model and the published experiments ⁸ for the clothed trunk at different wind velocity and aperture geometries for (a) impermeable open aperture and (b) permeable open and closed apertures	116
45.	Comparison between the ventilation obtained by the simplified model and a published experiment for the impermeable clothed arm at different conditions (walking with wind, walking without wind and wind without walking)	118
46.	Comparison between the ventilation obtained by the simplified model and the published experiments for the permeable clothed arm at different frequencies and aperture geometries for (a) no wind speed and (b) 1 m/s wind speed	119
47.	Comparison between the measured and predicted ventilation rate of the (a) clothed arm (b) clothed trunk and (c) inter-segmental ventilation	126
48.	Comparison between measured and predicted segmental ventilation rate of clothed arm (a) without natural convection ($T_{env} = 34^{\circ}\text{C}$, $T_{skin} = 34^{\circ}\text{C}$) and (b) with natural convection effect ($T_{env} = 25.5^{\circ}\text{C}$, $T_{skin} = 34^{\circ}\text{C}$).....	130
49.	Ventilation rate of the clothed arm segment for different (a) wind speeds (b) walking speeds (c) air permeability ($T_{env} = 25.5^{\circ}\text{C}$, $T_{skin} = 34^{\circ}\text{C}$)	132
50.	Percentage increase in ventilation rate and heat losses of clothed arm when the natural convection is included for (a) different wind and walking speed (b) air permeability ($T_{env} = 25.5^{\circ}\text{C}$, $T_{skin} = 34^{\circ}\text{C}$) ...	133

TABLES

Table	Page
1. Basic dimensions of the upper human body and the jacket	34
2. Properties of the jackets used in the experiments	39
3. Definition of the resistances and inductances in each direction	58
4. Thermal resistance equations corresponding to the thermal network that represents the heat transfer from the clothed trunk.....	61
5. Thermal resistance equations corresponding to the thermal network that represents the heat transfer of the clothed oscillating arm	68
6. Fabric properties of the thermal manikin ensemble	71
7. Set of experiments performed	75
8. Validation of the model ventilation at different wind speeds	100
9. Validation of the model total ventilation at different wind speeds ..	101
10. Percentage increase of trunk ventilation at different conditions....	104
11. Percentage change of arm ventilation at different conditions	105
12. Comparison between predicted and experimentally measured values of segmental ventilation and heat losses between open and closed connection	109
13. Overall air exchange rate (min ⁻¹) for a permeable coverall ($\alpha=0.415$ m/s) with closed and opened aperture in various conditions	122
14. The geometrical inputs of air gap	123
15. Comparison between the measured and predicted heat losses	127
16. Segmental heat losses of the arm at different body postures	129
17. Comparison between the clothed arm ventilation results	131
18. Clothed segmental heat losses	135

CHAPTER I

INTRODUCTION

Clothing ensemble presents a barrier between the environment and the skin. This barrier acts as protective material especially in hazardous environment. On the other hand, the porous characteristic of clothing helps the human body to get rid from the heat stress in hot environments by ventilation. Nevertheless, ventilation and protection phenomena are contradictory. Indeed, Conventional protective clothing system needed for minimizing the exposure of workers to hazardous aerosol particles are characterized by their low porosity and air permeability. Therefore, it subjects the worker to heat stress by reducing clothing air ventilation [1]. A compromise between high contaminant impermeability, good breathability and relatively high air permeability is well established by the nanotechnology. Nanotechnology includes the use of nano-sized materials for fabricating very thin fibers capable of forming a highly porous mesh characterized by a large surface-to-volume ratio to improve the clothing protection for better worker comfort [2]. A number of processing techniques have been used to prepare polymer nanofibers in recent years. However, electrospinning process is the most effective technique that does not only produce polymer fibers with nanometer scale diameters, but it is simple and convenient compared to other forming methods [3]. Electrospinning is based on accelerating a polymer solution in an electric field between a charged nozzle and a ground collector [4]. The electrospun nanofibers are usually deposited on a high permeable and porous substrate covering the collector of the electrospinning device. The result is a nanofiber web of high porosity, large surface-to-volume ratio, light weight and relatively high air permeability. In order to study the performance of nanofiber web in air filtration, different studies were held in the literature. Chattopadhyay et al. [5] studied the aerosol filtration of electrospun cellulose acetate filters with different mean fiber diameters, and compared the results with two conventional filters (glass fiber and microfiber filters). Kuo et al. [6] investigated the performance of ultrafine nanofibers against nanoparticles, and showed that this type of filter is advantageous especially when high filtration efficiency is required and low weight is desired. Therefore, many studies confirmed the efficiency of nanofibers in the air filtration. However, researchers related the performance of the electrospun nanofiber web, and its morphology to the electrospinning processing parameters, the air face velocity, and the aerosol particle diameter.

By varying the processing parameters of electrospinning such as the polymer concentration, the electric field, the time of electrospinning, and the volumetric flow rate, the properties of electrospun fibers can be manipulated [7, 8]. These properties such as the fiber diameter, the fiber thickness, and porosity affected the filtration performance of the filter as well as its air permeability [9]. Air face velocity is also a parameter that affects the performance of filters with nanofibers [7]. Because the electrospun nanofiber is used in protective garment, air permeability is considered as one of the desirable properties of the electrospun nanofiber filter. Therefore, optimization of electrospinning process for producing nanoweb with desirable air permeability by investigating the effect of electrospinning parameters on the air permeability presents a great interest [9].

Thus, the objective of this study is to present a useful method to study the effect of processing parameters of electrospinning on the performance of nanofiber filter and its properties. This is achieved by developing a systematic simplified model based on several models that relate the electrospinning processing parameters to (i) the penetration of aerosol particles through the electrospun nanofiber for a range of particle diameter and face velocity and to (ii) the ventilation of the electrospun nanofiber that usually depends on the air permeability of the electrospun nanofiber. The coupled models begin with the prediction of the electrospun fiber diameter. Then the morphology properties of the electrospun nanofiber web are deduced by coupling different models (porosity, thickness, and air permeability). In the filtration model, analytical expressions for the filtration or the penetration efficiency are used to assess the filter performance (Kirsh et al. 1975). Finally, the air permeability is used to study the ventilation of air provided by using the nanofiber material. The ventilation model is simplified using an electric circuit analogy. This simplified ventilation model is coupled with a human body thermal resistance network that simulated the thermal human responses.

For each step, a model is developed and validated by the corresponding experiment. The experiments performed starts by the fabrication of the electrospun nanofiber web by the electrospinning device, afterwards; the fiber diameter and the thickness of the electrospun nanofiber web are measured SEM device. Then, the porosity is deduced by weighting the nanofiber web by a microbalance. Moreover, the air permeability is measured by a capillary flow porometer. The filtration efficiency is measured by performing an experiment on the electrospun nanofiber web by generating aerosol particles and measuring the upstream and downstream concentrations. The ventilation is measured by performing an experiment on a thermal manikin using tracer gas method. The novelty of this study arises from developing a

design charts that allows the researcher to know, for desirable ventilation and protection, the air filtration provided, and to go backward to exactly know are the processing parameters of electrospinning that lead to these characteristics of the nanofiber web. On the other hand, this study permits to investigate the effect of using the nanofiber web in protective clothing on the thermal human body response and thermal comfort. This thesis work aims towards investigating the performance of incorporating the nanofiber web in the protective clothing to present a compromise between protection and thermal comfort of the wearer. This thesis mainly focuses on the following objectives:

- Predicting by modeling of the electrospinning process the final fiber diameter of the electrospun nanofiber web generated.
- Predicting by modeling the morphology of the nanofiber web including the fiber diameter, the porosity, the thickness, and the air permeability of the nanofiber web as well as the behavior of this web on filtering the air from the hazardous particles.
- Developing simplified ventilation models of clothing, coupling them to a bio-heat model and thermal resistance network that simulated the human body response, and validating them experimentally.
- Incorporating the nanofiber web in a clothing ensemble and study the effect of the nanofiber web on increasing the ventilation for the a significant filtration compared to conventional protective clothing.

CHAPTER II

METHODOLOGY

In order to achieve the objectives of this study, the flow chart of Fig. 1 is adopted.

First, a simplified model is developed to predict the final diameter of the fiber produced in electrospinning process. This is achieved by developing a mathematical model of the electrospinning process that combines both the stable and the unstable region and connects them by means of the stable jet outputs (radius and surface tension). Several experiments are performed to validate the model. For each experiment, the electric current and the final fiber diameter are measured to be compared with the value predicted by the model for each input set. Second, the morphological properties of the nanofiber web are predicted using different published models. These morphological properties are: porosity, thickness, and air permeability. After exploring the morphological properties of the nanofiber web, the filtration efficiency can be obtained from the classical filtration theory at a range of aerosol particle diameter and air face velocity. Different experiments are conducted to validate predictions of porosity, thickness, filtration efficiency, and air permeability. The performed experiments start by the fabrication of the electrospun nanofiber web using the electrospinning device, afterwards; the porosity and the thickness of the electrospun nanofiber web are measured using microbalance and SEM device respectively. The air permeability is measured by a capillary flow porometer, while the filtration efficiency is measured by performing an experiment on the electrospun nanofiber web through generating aerosol particles and measuring their upstream and downstream concentrations.

Finally, a model for predicting the ventilation through clothing is developed. This model differs from other models in taking into account the inter-connection between arms and segments. Different methods are used in this section as well as different experimental equipment. As a first step in this modeling, the clothed segment is modeled by solving the mass, momentum, and energy conservation in the microclimate space that separates the skin from the arm. Then, the segments are connected and the model is validated using Ansys. The validated model is then integrated to a bio-heat model that simulated the thermal response of the human body segment. In the other hand, an improved experimental approach is developed on the thermal manikin using tracer gas method to validate the integration. In a further study, the oscillating motion of

the human body is modeled by a simplified model that establishes the analogy between the ventilation model and the electrical circuit.

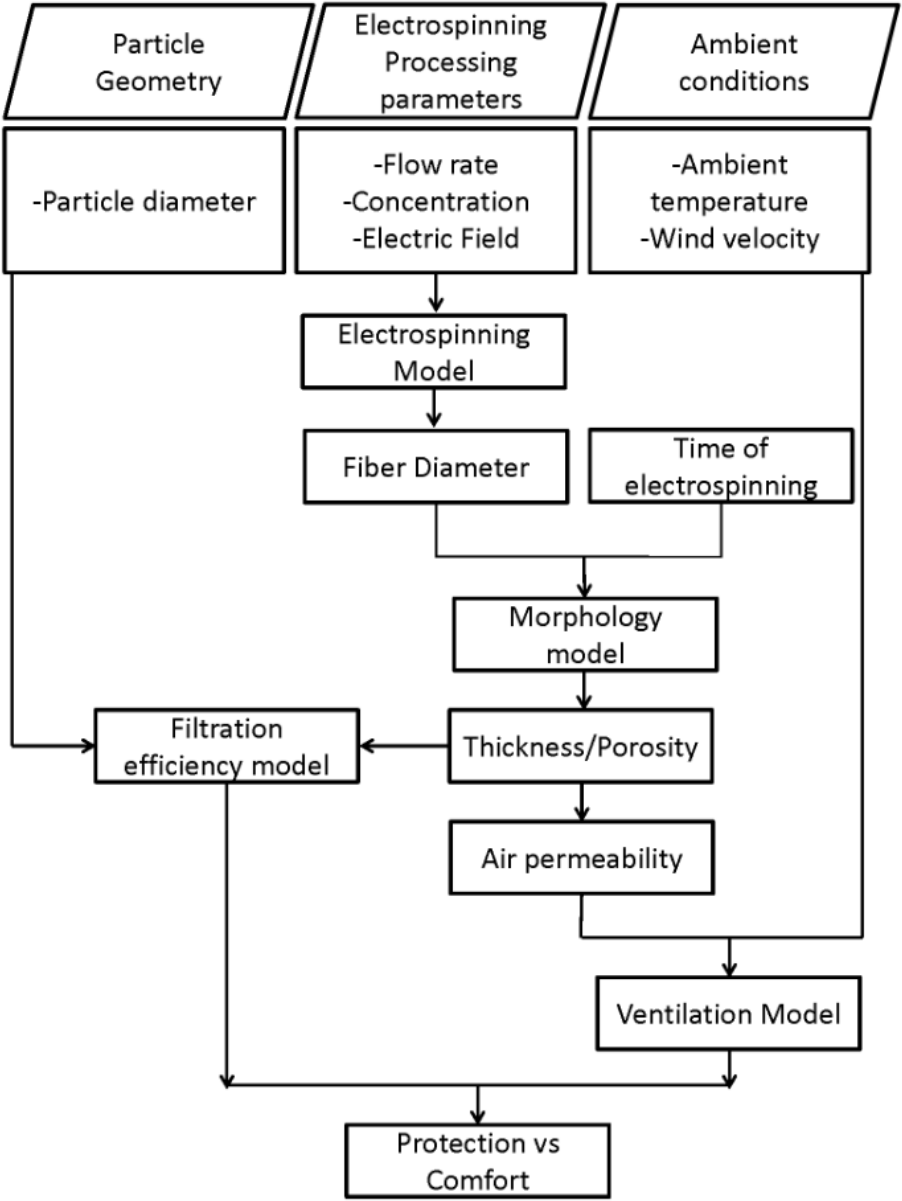


Figure 1: Flow chart of the complete methodology

A. Simplified modeling of the electrospinning process from stable jet region to unstable region to predict final nano-fiber diameter

1. Literature review

Electrospinning is a promising technique for producing nanofibers by subjecting a polymeric solution to an electric field [10]. In recent years, various polymers such as Nylon, Polyurethane and Polyacrylonitrile were successfully electrospun into ultrafine fibers [11-13]. Indeed, the increased popularity of electrospinning arises from the simplicity of the process as well as the ability to produce relatively thin non-woven mesh/membrane [14]. Electrospun nano-fibrous mesh has a large surface area due to the nano-diameters of their fibers which allow their use in filtration of sub-particles as well as in the adsorption of biological and chemical warfare gases, protective clothing, medical industry, and jet printing [15,16]

Since the purpose of electrospinning is to produce nano-fibrous mesh, it is of interest to predict via modeling the final fiber diameter of single-nozzle electrospinning. A model that predicts the final fiber diameter can be used to control the electrospinning process to achieve some desired fiber morphology, porosity, and physical characteristics and to improve the electrospinning efficiency.8 Recently, different models were developed for the electrospinning process. The modeling approaches in the literature [18-26] divided the jet into stable and unstable regions where different governing equations are attributed. The focus of the literature modeling was more on the portion of the electrified jet beyond the stable region where the jet became no more visible [18].

The stable jet region was modeled as an electrified jet subjected to stretching by an external electric field. The basic principles for modeling electrified jets were developed by Taylor [19] who discovered that it is impossible to account for most electrical phenomena under the assumption that the fluid is either a perfect dielectric or a perfect conductor. The reason is that any perfect dielectric fluid still contains a non-zero free charge density that lives on the interface between the fluid and the surrounding gas. The Taylor model is then improved by accounting for the effects of jet stretching, charge transport, and the electric field which is called the slender body model [20]. In the slender body model, regular perturbations for long jets can be expanded by using the integral formulations, Taylor's series expansions, weighted residuals, and variational principles. Feng [21] derived a modified model to avoid the instability issues of the slender body model. In Feng's model, the jet was represented by four steady-state equations: the

continuity equation, the momentum conservation, the charge conservation and the Coulomb's law. However, the generalized Newtonian constitutive relations were used for the viscous normal stress difference. Roozmond [22] expanded Feng's model to account for the viscoelastic properties of the polymer solution fluid. Recently, Helgeson et al. [23] derived a simplified approach for the first electrospinning stable stage and developed a correlation that predicts the electrospun fiber diameter. However, the models of Roozmond [22], Feng [21], and Helgeson et al. [23] are only applicable in the stable region of the electrospinning where the jet is still straight. The stable region is relatively a small distance compared to the total distance from the needle (nozzle) tip to the collector but the stable region affects the prediction of the final fiber diameter. Moreover, limiting the electrospinning process to the stable region cannot produce nanometer fiber diameter and the fibers leaving the stable region normally have diameters in the order of micrometers. Thus, it is of interest to connect the stable region model to the second jet flow stage of electrospinning in which bending instability region occurs to predict the final fiber diameter.

However, the model of the second stage of electrospinning (unstable region) presents a major challenge in the physics of electrically driven jet [24]. In order to model the bending instability region, Hohman et al. [16] performed a linear stability analysis of the slender charged fluid jet with the leaky dielectric properties in a tangential electric field. However, the linear stability analysis covers only the early stages of the evolution of the instability which is not usually the case for single-nozzle electrospinning [24]. Another model of electrospinning is developed by Yarin et al. [26, 27] who modeled a segment of the jet by a viscoelastic dumbbell. In their model, significant assumption is taken where bending is assumed to be driven by charge repulsion and resisted by the solution elasticity. However, their model did not include any asymptotic analysis to predict the magnitude of the terminal diameter that the whipping jet can reach. In addition, their model necessitated a high computational cost because of its complex numerical solution [27,28].

Therefore, there is a need to derive a simple and accurate model that relates the process parameters to the final fiber properties. Fridrikh et al. [29] derived a simple expression of the final fiber diameter in electrospinning based on the forces dominating the final stages of bending instabilities in electrospinning. However, Fridrikh et al. [29] expression of the final fiber diameter included a characteristic length parameter χ that was not calculated. Fridrikh et al. [29] reported an arbitrary range for χ and did not provide the method of its calculation. It is of interest to note that the characteristic length χ is related to the first electrospinning stage which is the

stable jet. By neglecting the relation between the characteristic length χ and the stable jet, Fridrikh et al. model [29] reported an average relative error of 20% for polyacrylonitrile solution.

The objective of this section is to develop a combined simplified model that covers the two connected stages of electrospinning: stable and unstable jets. Such a predictive model will help in predicting the behavior of different polymer-solvent solutions and different processing parameters as well as guiding the experimental studies. The novelty of such approach arises from the prediction of the final fiber diameter by modeling the straight jet and relating the stable properties of the stable jet to the unstable region model. The combined model incorporates all the physics of the jet during electrospinning process.

2. Mathematical formulation

a. Basic Equations of Electro-spun Polymer Jet

A scheme showing the horizontal electrospinning setup can be seen in Figure 2. The electrically conducting polymer solution, characterized by its density ρ , surface tension γ , dynamic viscosity η , electrical conductivity k , dielectric constant, is pumped at a volumetric flow rate Q out of an orifice of a metal syringe with a radius r_0 . A high voltage (2-20 KV) is applied between the needle and the grounded collector separated by a distance equal to L , where $L \gg r_0$. Upon applying a high voltage, the electrodes generate homogenous electric field of strength E_∞ directed horizontally from the needle towards the collector [30]. This electric field generates a tangential force on the charges distributed at the jet surface. The tangential force causes the jet to emanate from the tip of a needle as a charged liquid cone. Afterwards, it is transformed into a thin straight jet for a relatively short distance L_{sj} and then becomes erratic and unstable due to bending instability.

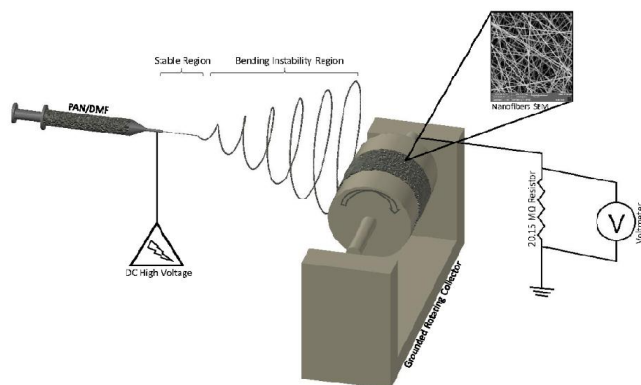


Figure 2: Schematic of the experimental set-up for electrospinning

The behavior of the electrospun polymer is generally described by the electro hydrodynamics equations that include the mass, momentum, charge conservation and Coulomb's law inside the fluid jet. These equations relate the radius r , the jet velocity v , the surface charge density ζ , and the electric field E to axial distance z . The physical model of the electrospun jet is shown in Figure 2 and divides the jet into two regions: (a) stable region and (b) bending instability region. The physical parameters that influence the behavior of the electrospun jet in both regions include both the jet solution properties and the electrospinning process parameters. The solution properties are mainly related to the polymer and solvent and to the polymer concentration in the solution which determines then the effective solution viscosity η , the electrical conductivity k , the surface tension γ , the electrical permittivity $\bar{\epsilon}$, and the density ρ . The electrospinning processes parameters are the jet flow rate Q , the electric field E_∞ (computed from the ratio of the difference in voltage ΔV to the distance L from the tip to the collector $\Delta V/L$), and the initial radius r_0 of the nozzle. The processing parameters E_∞ and Q and the solution electrical conductivity can be used to determine the electric current I flowing through the jet using current-voltage relationships reported for electrospinning experiments [25, 30-34]. Although I can be measured experimentally [32] by connecting a resistor between the collector and the ground, Bhattacharje *et al.* [34] reported that the electric current measured in electrospinning scales as the product $E_\infty Q^{0.5} k^{0.4}$ for wide polymer solutions in organic solvent and can be expressed as

$$I = a * E_\infty * Q^{0.5} * k^{0.4} \quad (1)$$

where a is an empirical constant predicted as a function of the polymer solution and the geometrical characteristics of the electrospinning device. Equation (1) eliminates the need to perform measurements for the current once the coefficient a is determined for a given polymer solution. In what follows, the governing equations of both jet regions are presented, followed by the combined numerical/analytical solution methodology.

i. Stable jet region

In the stable jet region shown in Figure 2(a), the liquid is liquid is characterized by weak conduction and therefore the “leaky electric model” applies [21]. The slender-body approximations is adopted to model the stable viscoelastic electrospun jet where the flow is simplified to a non-uniform elongation with all quantities depending only on the axial position z . In addition, negligible effect of solvent evaporation from the jet is assumed. Moreover, the viscoelastic Giesekus constitutive laws are used in order to find a relation between the viscous

stresses in the momentum equation. The Giesekus model adds quadratic nonlinearity and considers that the deviatoric stress as the sum of solvent and polymer stresses [31].

The current model for the stable jet region is based on Feng's model [21] where the jet is governed by four steady-state equations representing the conservation of mass, electric charges, the linear momentum balance, and Coulomb's law. By using the stated assumptions, the equations governing the stable jet are applicable for a specific length which is the stable length L_{sj} . However, the stable length is a function of the stable model output parameters [36]. In order to calculate the stable length, He *et al* [36]. provide a rational theory considering a steady state flow of an infinite viscous jet pulled from a capillary orifice and accelerated by a constant external electric field. Since the electrical force is dominant over other forces in the stable jet, then the bending instability occurs when the conductive and convective electric currents are equal. He *et al.* [36] derived the equation of the stable jet length based on this criterion as follows:

$$L_{sj} = \frac{4kQ^3}{\pi\rho^2 I^2} \left(\left(\frac{2\zeta_{sj}Q}{\pi K\rho E_{sj}} \right)^{-2/3} - r_0^{-2} \right) \quad (2)$$

Therefore, the model electro-hydrodynamic equations will be derived for an arbitrary assumed stable length L_{sj} which would be corrected iteratively based on model output as will be described in the methodology following Feng's model [21].

The complete derivation of the stable jet model can be found in the work of Feng [21] and Reneker *et al.*[24].

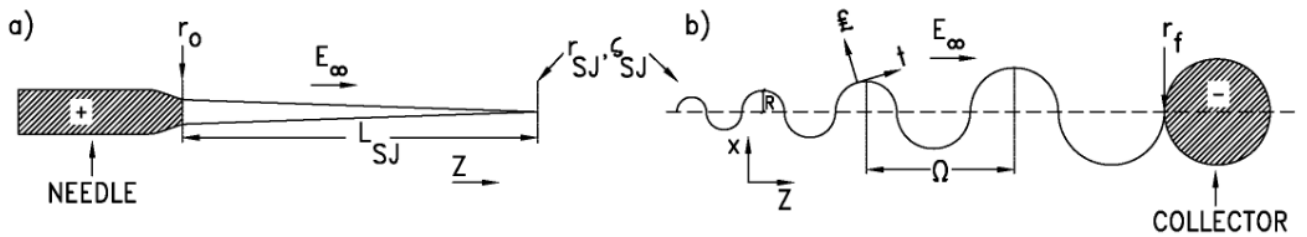


Figure 3: Physical model of the electrospinning process (a) stable jet (b) bending instability

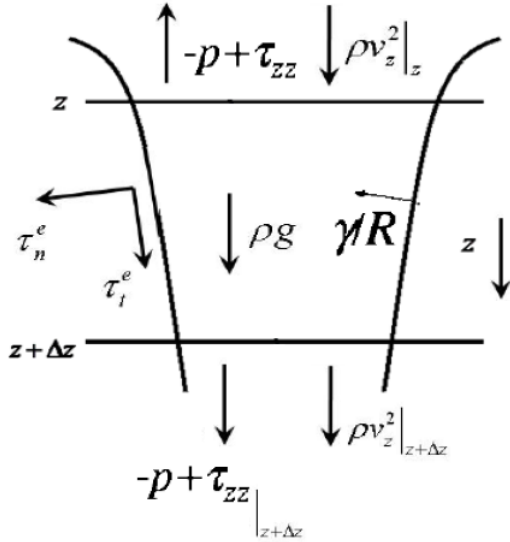


Figure 4: The forces applied to the chosen control volume

- Boundary conditions

At the onset of the electrospinning, the jet just outside of the nozzle has a radius r_0 and a velocity v_0 . Surface charge density boundary condition has been a long standing problem in previous studies of electro-spraying and electrospinning [21]. Hohman *et al.*[35] solved this problem by fitting the model predictions to the measurements and found that a steady solution is attained if only the surface charge density tends to zero at the onset of electrospinning. Thus, the zero charge density at the onset of the jet is adopted in this model. Since the surface charge density is null, the electric current is only limited to the conductive part at the onset of the jet. Therefore, the electric field is deduced from equation (4) by neglecting the convective part. Finally, the shear inside the nozzle is assumed ineffective in stretching polymer molecules as compared with the elongation downstream, such that the stress at the onset of the jet is purely Newtonian [22]. At the final stage, the jet thinning is no longer considerable and zero gradients is then applied to the radius, the velocity, the surface charge density, and the electric field.

By solving the stable jet governing equations for the charge density, velocity, electric field as function of z , then the stable radius and the surface tension can be calculated. These two outputs will be used in the governing equations of the unstable jet.

ii. Bending instability

While electrospinning is a simple process to perform, the bending instability involves a complex interplay between fluid dynamics, electrodynamics, and rheology. Given this complexity, it is difficult to derive a mathematical model for the bending instability [28]. Therefore, it is

indispensable to make few assumptions that allow the derivation of the expression that relates the final fiber diameter to electrospinning process and parameters. The jet is mainly treated as a slender viscous object. In addition, at the final stage of the whipping mode, the radius is decreasing, and the competition is viewed between the surface tension and the surface charge repulsion. Moreover, the electric current equation (7) is reduced to the convective term at the final stage of electrospinning and the conductive term is neglected. Based on the above assumptions, Frifrikh *et al.* [39] presented a simple expression that relates the final fiber diameter to the influencing parameters based on the equation of motion for the normal displacement derived from Hohman *et al.* work [31].

The model prediction arises from a force balance between the surface tension and the electrostatic charge repulsion. The expression is then corrected by the concentration of the polymer in the solution. The model treats the jet as a slender viscous object. The equation of motion for the normal displacement x (see Figure 2) of the jet centerline is presented by Hohman *et al.* [31] as follows:

$$\rho\pi r^2 \ddot{x} = 2\pi\zeta E_\infty \hat{\xi} + \left(\pi\gamma + \frac{r\bar{\epsilon}}{2} \beta(E_\infty \hat{t})^2 + \frac{2\pi^2 r\zeta^2}{\bar{\epsilon}} (3 - 2\ln \chi_{bi})\right) \frac{r}{R} \quad (3)$$

where ξ and t are respectively the normal and the tangential direction of the bending instability curvatures and R is the radius of curvature of the bending instabilities. The first term of equation (9) accounts for the effect of electric field on the surface free charges of the jet. The second term is the surface tension. The third term originates from the bending motion. The last term is the electrostatic repulsion. At the final stage of the whipping mode, the radius is decreasing, and the competition is viewed between the surface tension and the surface charge repulsion. Furthermore, at the late stage of whipping, equation (3) is reduced as following:

$$2\pi r\zeta v = I \quad (4)$$

By using equation (3) and (4), the final fiber diameter at the final whipping stage lead to the expression of Frifrikh *et al.*[39] given by

$$r_f = 0.5 * C^{0.5} \left(\gamma \bar{\epsilon} \frac{Q^2}{I^2} \frac{2}{\pi(2\ln \chi_{bi} - 3)} \right)^{1/3} \quad (5)$$

where χ_{bi} is the ratio of the characteristic axial length scale. The above expression is mostly limited to selective polymer-solvent system [28] and is applicable to the final stage of electrospinning when the competition is between the surface tension force and the electrostatic repulsion [29]. The expression of Frifrikh *et al.* [39] is not applicable to relatively high polymer solution concentration higher than 12% because of the relatively large viscous force dampers.

Therefore, the viscous force cannot be neglected and the bending instabilities that occur are quite smooth.

The ratio of the characteristic axial length scale χ_{bi} was defined by Hohman *et al.*[25, 31] and is determined in practice by the shape of a jet as it thins away from the nozzle to the stable radius of the jet. Thus, the characteristic axial length scale is the wavelength Ω (in meters) estimated from the fastest growing mode of the spinning jet that leads to the maximum thinning [24]. Therefore, the dimensionless parameter χ_{bi} appearing in equation (5) is given by

$$\chi_{bi} = \frac{\Omega}{r_{sj}} \quad (6)$$

where r_{sj} is the final radius of the jet at the stable region and it is obtained from solving the governing equations of the stable jet region. The maximum growth rate [27] w_{max} of the bending instabilities radius R is:

$$w_{max} = \left(\frac{9\pi^4 \zeta_s}{r^2 \mu}\right)^{1/3} \left(\frac{2\pi\rho}{\bar{\epsilon}} (2 \ln \chi_{bi} - 3)\right)^{1/6} \quad (7a)$$

On the other hand, the wavelength, shown in the characteristic axial length scale equation (equation 12), is estimated from the wave number \mathcal{K} of the instabilities occurring in the stable jet [24] as follows:

$$\Omega = \frac{2\pi}{\mathcal{K}} \quad (7b)$$

The equation of the wavenumber \mathcal{K} is derived by Reneker *et al.*[24] by balancing the forces resulting from the surface charge density and the viscosity of the solution. This equation corresponds to the maximum growth rate of the bending instabilities and presents a strong link between the stable and the unstable regions. The reason is that the wavenumber equation \mathcal{K} is function of the two stable jet output: r_{sj} (final radius) and ζ_{sj} (the final surface charge density) at L_{sj} . The wave number \mathcal{K} equation¹⁵ becomes

$$\mathcal{K} = \left(\frac{\pi^2 \zeta_{sj}}{r_{sj}^2 \mu}\right)^{1/3} \left(\frac{2\pi\rho}{\bar{\epsilon}} (2 \ln \chi_{bi} - 3)\right)^{1/6} \quad (7c)$$

As the wave number \mathcal{K} depends on χ_{bi} parameter, iterations are needed to find the convergent χ_{bi} required to determine the final diameter r_f , to find the final fiber diameter. The coupling between the stable jet and the bending instability stage occurs by using the stable jet radius r_{sj} and the stable surface charge density ζ_{sj} in order to find the ratio χ_{bi} . The novelty of the method arises from this coupling that combined several validated models to generate a simplified model that relates the electrospinning parameters to the final fiber diameter. In other words, the model of

Frifrikh *et al.* [21] is modified by calculating the characteristic length χ_{bi} based on Hohman *et al.*[25, 31] definition and using the equations developed by Reneker *et al.* [24]. These equations are related to the first stage of electrospinning (the stable jet) based mainly on the work of Feng [21].

b. Numerical solution

Figure 5 shows the flow chart of the model numerical approach. The coupled equations with associated boundary conditions are discretized using a finite volume methodology, where the electrospinning jet is divided into N_z grids of circular cross section and size Δz . Central differencing is used for second order terms. The input set divided on solution properties and processing parameters are used in the model. The stable length L_{sj} value is assumed, the size of grid Δz is calculated based on a constant number of grids $N_z=366$. Afterwards, an initial guess for the radius r , surface charge density ζ , electric field E , and velocity v for all nodes is assumed and iterated until convergence is achieved to a maximum relative error of 10^{-5} . Once all these unknowns are predicted for all nodes, the stable r_{sj} , surface charge density ζ_{sj} , electric field E_{sj} , and velocity v_{sj} are used to calculate the stable length L_{sj} . Thus, the calculation is repeated and an updated stable length is predicted. The calculation of the stable length is also repeated until convergence is achieved to a maximum relative error of 10^{-5} . The numerical solution is repeated for grid sizes to ensure that a grid-independent solution is obtained. In the presented simulations, the number of grid points was 366 in the jet direction with Δz depending on the stable length. The coupling between the stable jet and the bending instability region occurs by using the stable radius r_{sj} and surface tension ζ_{sj} in the bending instability equations. First, the wavelength Ω is assumed, then the dimensionless parameter χ_{bi} is calculated using the stable radius r_{sj} . After that the wave number is calculated based on the dimensionless parameter χ_{bi} and the stable surface tension ζ_{sj} . Then, the corresponding wavelength is re-calculated and compared to the assumed one. The calculation is repeated until the wavelength convergence is achieved to a maximum relative error of 10^{-5} . Finally, the terminal jet fiber radius of equation (4) is calculated.

3. Experimental methodology

a. Materials

Polyacrylonitrile (PAN) with an average molecular weight of 150,000 g/mol and N, N-dimethylformamide (DMF) ($\geq 99.8\%$, A.C.S. spectrophotometric grade) were purchased from Sigma-Aldrich and used as received without further purification.

b. Preparing PAN nanofibers

PAN polymeric solutions at different concentrations were prepared by dissolving PAN powder in DMF under constant magnetic stirring of 900 rpm for 24 hr at room temperature [37]. In order to remove the entrapped air bubbles, the polymeric solutions were sonicated in Cole-Parmer 8851 sonication bath at 47 KHz for about 20 min prior to electrospinning process. A laboratory scale electrospinning machine (FLUIDNATEK LE-10, BIOINICIA, Spain) was used for preparation of PAN nanofibers (Figure 6). The inner and outer diameters of spinneret nozzle were 0.6 mm, and 0.9 mm, respectively. The collector was a rotating drum (100 mm diameter x 200 mm length) made of anodized aluminum covered by a piece of aluminum foil, with a variable rotational speed from 200 rpm to 2000 rpm. By specifying the flow rate, applied voltages (0-30 KV), the tip-to-collector distance, and the velocity of the collector drum a horizontal electric field was generated between the nozzle and the collector. This electric field allows the jet to leave the nozzle and to be stretched horizontally. The electrospun nanofibers were collected at controlled room temperature of 20 °C and 30% RH [38].

c. Electric current measurement

In order to find the current correlation, the electric current should be measured for different electrospinning conditions. For this measurement, one can measure the voltage drop across a resistor that is in series with the grounded collector using Ohm's law [32]. As the electric current during electrospinning is in the order of nano to micro amperes, therefore, a resistance of high impedance (20 M Ω) and a regular voltmeter (FLUKE 117 multi-meter) were used.

d. Measuring fiber diameter

Morphological observation of electrospun samples was performed with Scanning Electron Microscope (MIRA 3 LMU tescan) operating at an acceleration voltage of 15 kV, working distance of 3 mm and using an InBeam detector at a magnification range from 3 KX to 50KX. For each electrospun web, 5 circular specimens were cut from different places, 20 fibers measurements each. Accordingly, 100 measurements were averaged with their proper standard deviation using MIRA built in measurement software.

PAN solutions at various concentrations were electrospun under the ambient conditions of 20°C and a relative humidity of about 30%. A different set of experiments was performed where one parameter was varied in each set as shown in Table I. In the first set, the flow rate was varied from 900 to 1320 $\mu\text{l/hr}$ while the electric field and the polymer concentration were kept constants

at respectively 97222 V/m and 10%. The aim of this set is to figure out the effect of solution flow rate on the final fiber diameter. In the second set, the electric field was varied from 88,889 to 113,889 V/m, while the flow rate and the polymer concentration were kept constants at respectively 900 $\mu\text{l/hr}$ and 10%.

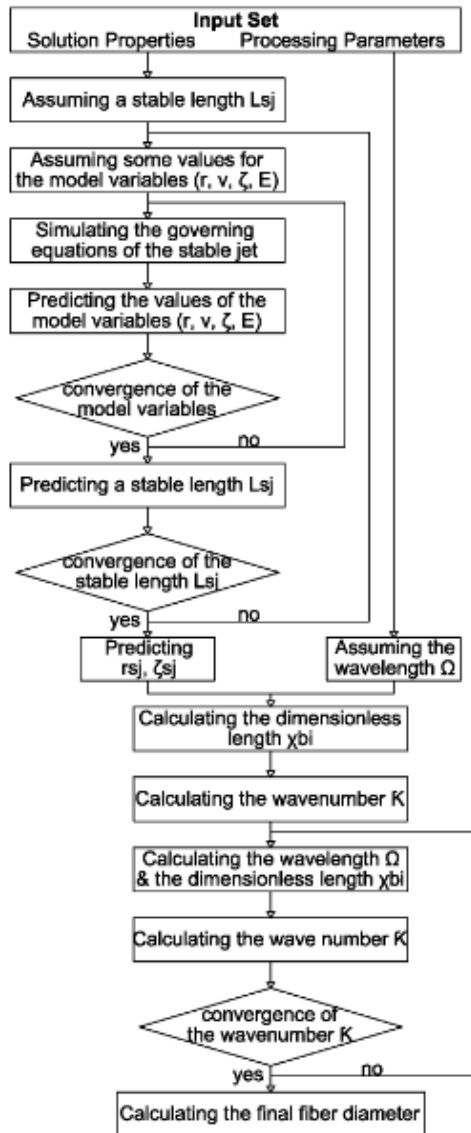


Figure 5: Flow chart of the complete model

These experiments will examine the influence of increasing the electric field on the final fiber diameter. Finally, in the third set, the polymer concentration was varied from 8% to 11% while the electric field and the flow rate were kept constants at respectively 97,222 V/m and 900 $\mu\text{l/hr}$. These experiments aim to establish the profile of the final fiber diameter against the polymer concentration. It is of interest to note that all the electrospinning parameters are chosen in a range that ensures generation of a continuous jet without droplets [38].

For each experiment, the electric current was measured and five different samples from different parts of the final web were studied by SEM to measure the final fiber diameter and its distribution (see Figure 7). The measured electric current was used to calculate the empirical constant a in equation (1). The electric current equation (equation 1) was used in the model.

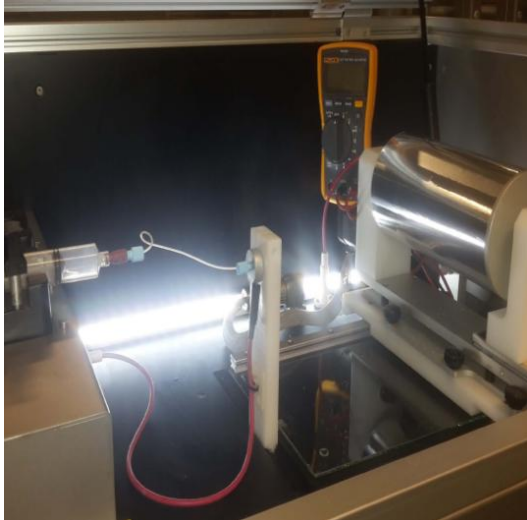


Figure 6: Electrospinning device used

B. Study the effect of processing parameters on the performance of nanofiber filtration efficiency and morphology

1. Literature review

Over the last two decades, the rapid development of the nanotechnology resulted in great progress not only in the preparation of nanofibers, but also in their functional applications [48]. The unique characteristics of nanofibers such as the high surface-to-volume ratio, high porosity, and light weight are considered desirable for many applications [49-51]. Currently, the most interesting applications are identified in the following functional areas: biomedical, energy harvest and storage, and environmental protection [48]. The last functional area is considered of great importance since current environmental problems have serious negative impacts on human health [52]. Due to their high specific surface area, nanofibers are expected to be used in the filtration of pollutant substances from air or liquid [53]. Furthermore, the high porosity, the low basis weight, and the small pore size make the nanofibers appropriate to be used in garments for protective clothing [54]. Another important feature of nanofibers in protective garment is its

high air permeability compared to most of conventional protective clothing material currently available [54].

A number of processing techniques have been recently used to prepare polymer nanofibers [55]. However, electrospinning process is the most effective technique that does not only produce polymer fibers with nanometer scale diameters, but it is simple and convenient compared to other forming methods [54]. Electrospinning is based on accelerating a polymer solution in an electric field between a charged nozzle and a ground collector [4]. The electrospun nanofibers are usually deposited on a high permeable and porous substrate covering the collector of the electrospinning device [54]. The result is a nanofiber web of high porosity, large surface-to-volume ratio, light weight and relatively high air permeability.

In order to study the performance of nanofiber web in air filtration, different studies were reported in the literature. Chattopadhyay et al. [5] studied the aerosol filtration of electrospun cellulose acetate filters with different mean fiber diameters, and compared the results with two conventional filters (glass fiber and microfiber filters). Kuo et al. [6] investigated the performance of ultrafine nanofibers against nanoparticles, and showed that this type of filter is advantageous especially when high filtration efficiency is required and low weight is desired. These studies confirmed the efficiency of nanofibers in the air filtration. However, researchers related the performance of the electrospun nanofiber web, and its morphology to the electrospinning processing parameters, the air face velocity, and the aerosol particle diameter. The properties of electrospun fibers can be manipulated by varying the processing parameters of electrospinning such as the polymer concentration, the electric field, the time of electrospinning, and the volumetric flow rate [7,8]. These properties such as the fiber diameter, the fiber thickness, and porosity affect the filtration performance of the filter as well as its air permeability [9]. Air face velocity is also a parameter that affects the performance of filters with nanofibers [7]. Because the electrospun nanofiber is used in protective garment, air permeability is considered as one of the desirable properties of the electrospun nanofiber filter. Therefore, optimization of electrospinning process for producing nanoweb with desirable air permeability is of great interest [9]. Such optimization has been dependent on empirical methods to deduce processing parameters that result in given nanoweb properties. The use of a modeling approach of electrospinning process to predict nanofiber morphology would serve as an important design tool in such processes.

Thus, the objective of this study is to present a useful method to study the effect of processing parameters on the performance of nanofiber filter and its properties. This is achieved by

developing a systematic simplified model based on coupled published models that relates the electrospinning processing parameters to (i) the penetration of aerosol particles through the electrospun nanofiber for a range of particle diameter and face velocity and to (ii) the air permeability of the electrospun nanofiber that usually depends on the porosity and the thickness of the electrospun nanofiber. The coupled published models begin with the prediction of the electrospun fiber diameter using Ismail the recent model developed. Then the electrospun nanoweb porosity is computed by a numerical model based on randomly distributed fibers [45]. Furthermore, the thickness which is strongly related to the time of electrospinning process and the porosity helps in finding the air permeability of the nanofiber web [46]. In the filtration model, analytical expressions for the filtration or the penetration efficiency are used to assess the filter performance [47].

2. Mathematical formulation

The morphological properties of the electrospun nanofiber web are mainly related to the fiber diameter and the basis weight. The basis weight in turn is related to the electrospinning time and it is defined as the mass of the fiber per unit area. The morphological properties described in this section are the porosity, the thickness, and the air permeability.

a. Porosity

In order to theoretically predict the porosity of the electrospun nanofiber, the algorithm of Lowery et al. [45] is adopted. This algorithm is based on treating the mat as quantized planes of overlapping fibers and creating a randomly oriented fibers grid. The algorithm is converted to a numerical model written in Matlab language. The input variables to the numerical model are the sample dimensions, the fiber diameter, and the number of fibers generated [45]. The output variables of this numerical model include the number of pores, the mass density vector defined as the number of fibers localized in each node of the studied mat, the size for inner and outer pores (wall pores), and the overall porosity of the mat. Before executing the simulation, the number of fibers is predicted depending on the processing parameters. Lowery et al. [45] presented a method to measure the number of fibers as following. First, the mass deposition rate of fibers \dot{m}_f is calculated as a function of the solution volumetric flow rate Q , the solution density ρ_s , and the polymer concentration C :

$$\dot{m}_f = Q \rho_s C \quad (8)$$

Using the electrospun fiber diameter computed from equation (5), the length of fiber deposited per time is given by [45]:

$$v_f = \frac{4 \dot{m}_f}{\rho_f \pi d_f^2} \quad (9)$$

where ρ_f is the fiber density which is assumed equal to the polymer density.

It is of interest to note that the rate of deposition of the fiber on the rotating collector is related to the rotation speed and the collector radius [45] as follows:

$$v_T = 2\pi R_T \omega \quad (10)$$

where v_T is the velocity of the deposition point on the rotating collector, R_T and ω are respectively the radius of the rotating collector and is the rotation rate. Finally, the number of fibers during a single rotation is computed by dividing the length of the fiber deposited per time to the rate of fiber deposition. Thus the total number of fibers N_f for the complete electrospinning process is calculated as

$$N_f = \frac{v_f}{v_T} 2\pi\omega t_e \quad (11)$$

where t_e is the electrospinning process time. After computing the number of fibers generated during the electrospinning process, a small sample of the nanofiber mat is chosen and its dimensions are used as the sample dimensions input to the numerical model. The fiber diameter is computed using equation (5), and the number of fibers generated for this sample is predicted by multiplying the total number of fibers by the geometrical ratio of the sample to the collector surface area. In order to compute the porosity p , the numerical model counts the number of void nodes unoccupied by the fibers over the total number of nodes.

b. Thickness and air permeability

In order to calculate the average thickness \bar{z} of the nanofiber mat, a common relation between the basis weight w , the fiber density ρ_f , and the porosity p is used [56]:

$$\bar{z} = \frac{w}{\rho_f (1-p)} \quad (12)$$

The prediction of the air permeability through the nanofiber is somehow complicated. This is due to the fact that the air flow around the electrospun nanofiber is no longer in the continuum flow regime. This implicates that the use of the so-called no-slip velocity boundary condition at the fiber surface is not justified [46]. Instead, significant slip occurs when air flows around a nanofiber. Therefore, the air permeability equation is developed from the model of Hosseini et

al. [46] in which the effect of slip flow on the air permeability is taken into account. The air permeability is given by the following expression:

$$AP = \frac{3d_f^2 \Delta p}{80\alpha \mu_{air} \bar{z}} [-\ln(\alpha) - 0.931] C_r \quad (13)$$

Where α is the solidity ($1-p$) of the nanofiber web, C_r is the correction factor that is used to modify the original permeability that is based on the no-slip boundary condition in order to incorporate the slip effect. Δp is the standard pressure drop for testing fabric (124.5 Pa). C_r is basically the ratio of the pressure drop when considering the no-slip boundary condition to the pressure drop across a conventional slip boundary condition. Thus C_r is given by the following equation:

$$C_r = \frac{ku(1 + 1.966 Kn_f)}{(Ku + 1.996 Kn_f (-0.5 \ln \alpha - 0.25 + 0.25\alpha^2))} \quad (14)$$

Where ku is the Kuwabara number ($ku = -0.5 \ln \alpha - 0.75 + \alpha - 0.25\alpha^2$) and Kn_f is the fiber kundsens number defined as the ratio of the air molecules mean free path and the fiber diameter ($kn_f = 2\lambda / d_f$).

c. Air filtration model

It is based on the calculation of the filtration efficiency η , of a filter with a solidity α , fiber diameter d_f , and thickness \bar{z} . The model begins by the calculation of the single fiber efficiency η_Σ represented as a sum of efficiencies due to diffusion η_D , interception η_R , and a combination term η_{DR} as following [47]:

$$\eta_\Sigma = \eta_D + \eta_R + \eta_{DR} = 2.7Pe^{-2/3} (1 + 0.39ku^{-1/3} Pe^{1/3} kn_f) + 0.624Pe^{-1} + \frac{1}{2k} \left\{ \frac{1}{1+R} - (1+R) + 2(1+R) \ln(1+R) + \frac{2.86kn_f(2+R)R}{1+R} \right\} + 1.24ku^{-1/2} Pe^{-1/2} R^{2/3} \quad (15)$$

where Pe is the Peclet number which is the ratio of advective to diffusive transport rate of aerosol particles, ku is the Kuwabara number, kn_f is the fiber Kundsens number, R is the interception number calculated as the ratio of particle diameter over the fiber diameter ($R = d_p / d_f$). The Peclet number is given by the following equation:

$$Pe = \frac{3\pi\mu u_0 d_p d_f}{k_b T C_c} \quad (16)$$

Where u_0 , d_p , k_b , and T are the filter face velocity, particle diameter, Boltzmann's constant (1.38×10^{-23} J/K), and temperature, respectively. C_c is the Cunningham slip correction factor, which depends on the ratio of the mean free path of air molecules to the particle diameter and it is the result of the slip flow of the fluid at the surface [57].

Based on the single fiber collection efficiency η_Σ , the fiber diameter d_f , the filter thickness \bar{z} , and the filter solidity α , the filter efficiency η is given by the following equation of Hill et al. [58]:

$$\eta = 1 - \exp\left(\frac{-4\alpha\eta_\Sigma\bar{z}}{\pi d_f}\right) \quad (17)$$

3. Experimental approach

a. Thickness measurement

The measurements of thickness of electrospun samples were performed using a Scanning Electron Microscope (MIRA 3 LMU Tescan) operating at an acceleration voltage of 15 kV, working distance of 3mm and using an InBeam detector. Scale given on the magnification bar was used to measure the fiber diameter. The examination of the nanofiber web thickness was somehow complex. This is due to the compression of the nanofiber web edge when it is cut [59]. One way to overcome this issue is to adopt the freeze-fracturing technique which consists of cutting the web while it is immersed and frozen in liquid Nitrogen. Once the technique is implemented, the web is exposed vertically with the help of a vertical holder in the SEM machine and sputter coated with gold for 90 seconds using a sputter current of 10 mA (Q150T ES Turbo-Pumped Sputter Coater/Carbon Coater, Quorum Technologies). Fifty readings were taken from several places and averaged to get the mean nanofiber web thickness. Because the thickness measurement of the nanofiber web was critical and influenced the porosity measurement, another method was used to ensure the validity of the nanofiber web thickness measurement. This measurement was done using Brunswick Instrument TMS-1 gage equipped with MP-1 Metrology Processor with a thickness measurement resolution of 0.2 μm . This experiment was repeated for 45 different locations of the electrospun nanofiber web. Good agreement was shown between the SEM and TMS-1 gage measurements. Figure 7 shows an example of the SEM measurements of (a) the fiber diameter and (b) the nanofiber web thickness.

b. Porosity measurement

In order to measure the porosity of the electrospun nanofiber web, XS Microbalance (Mettler Toledo) is used [60]. This device has an accuracy of 1 μg . The microbalance measures the mass of a unit squared centimeter area which is, in other words, the basis area w . Thirty samples were chosen to be weighted from different locations of the nanofiber web and the average basis area \bar{w} is found. By computing the volume of the weighed sample ($V = \bar{w} * \bar{z}$), the bulk density ρ is deduced. Therefore, the porosity, p , is computed as function of bulk density, ρ , and fiber density ρ_f and is given by [45]:

c. Air permeability

For each nanofiber web, nine different samples of 2.32 cm diameter disk were cut from different locations for the air permeability analysis. A capillary flow porometer (CFP-1100 AH, American PMI) was used to measure the Frazier air permeability. Both the wet up and dry up modes are used. The wet up mode allows the pores to be filled with Galwick liquid of known surface tension (15.9 mN/m). The dry up allows the air to displace the liquid from the pores. The capillary flow porometer measures the air pressure required to flush out the liquid from the pores as well as the air flow rate that passes through the nanofiber web [61]. From the measured air pressure and flow rate, the capillary flow porometer calculates the Frazier air permeability at a pressure of 125 Pa (12.7 mm H₂O) for each sample.

$$p = \left(1 - \frac{\rho}{\rho_f}\right) \quad (18)$$

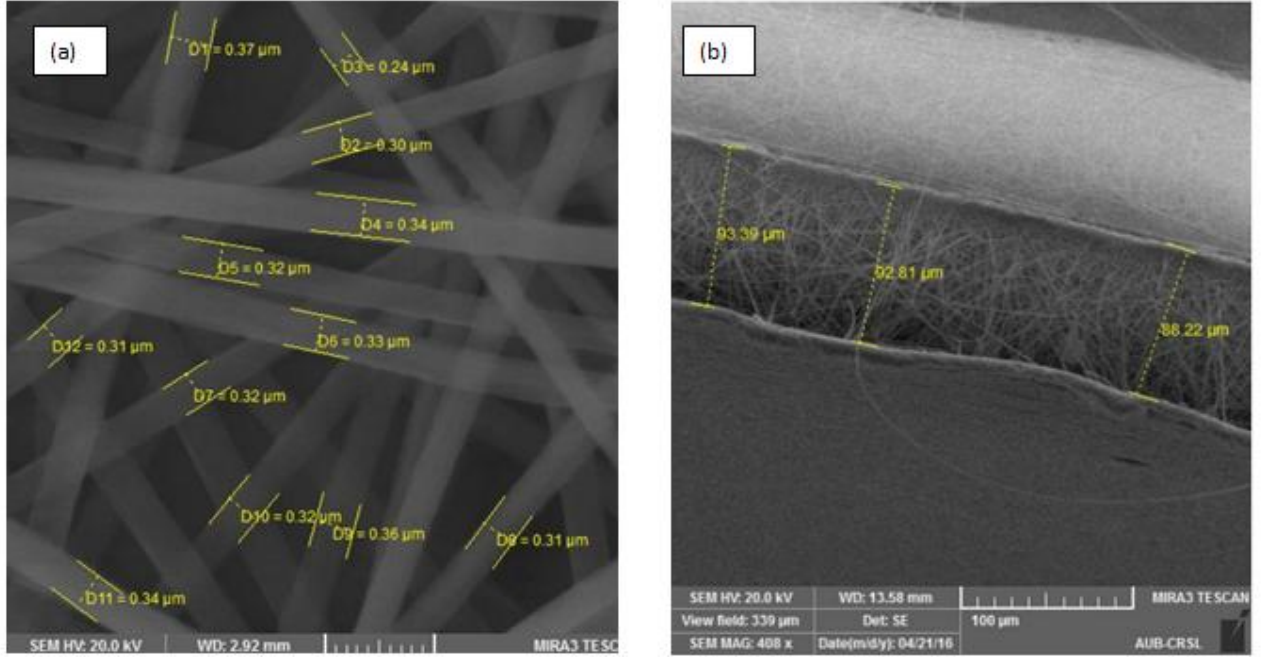


Figure 7: SEM images chosen as examples for the following processing parameters ($Q=900 \mu\text{l/hr}$, $E=97222 \text{ V/m}$, $C=10\%$ and $t_e=6 \text{ hours}$) showing the measurement of (a) fiber diameter (b) nanofiber web thickness

d. Air filtration (Aerosol collection efficiency)

A schematic diagram of the experimental set up used for the air filtration efficiency measurement is illustrated in figure 8. The system consists of a condensation aerosol generator, an injector, a filter holder, and sampling instruments. The experiment was performed in a small wind tunnel of $15 \times 15 \text{ cm}$ cross section and 1 m length. The wind tunnel fan is used for mixing purpose. The filter holder is a $50\text{cm} \times 50\text{cm}$ cross section channel and 40 cm length. The condensation aerosol generator was used to produce poly-disperse aerosol particles of concentration greater than $10^6 \text{ particles/cm}^3$ in a diameter range of 0.1 to $1 \mu\text{m}$. The generated aerosol particles are injected into the wind tunnel using five injection ports of 1 cm diameter close to the wind tunnel fan. The particles were then carried to the filter holder by the wind. The filter holder is a $5\text{cm} \times 5\text{cm}$ cross section channel and 40 cm length placed at the end of the wind tunnel. Particle concentrations were measured upstream and downstream using two instruments: an engine exhaust particle sizer (3090 EEPSTM) for particles in the diameter range less than 500 nm and an optical particle sizer for the other range larger than $0.5 \mu\text{m}$. Both instruments have a fast-response and high size resolution. Finally, the aerosol filtration efficiency η of the electrospun nanofiber web is given by the following equation:

$$\eta = (C_u - C_d) / C_u \quad (25)$$

where C_u and C_d are the upstream and downstream concentration of the electrospun nanofiber web respectively.

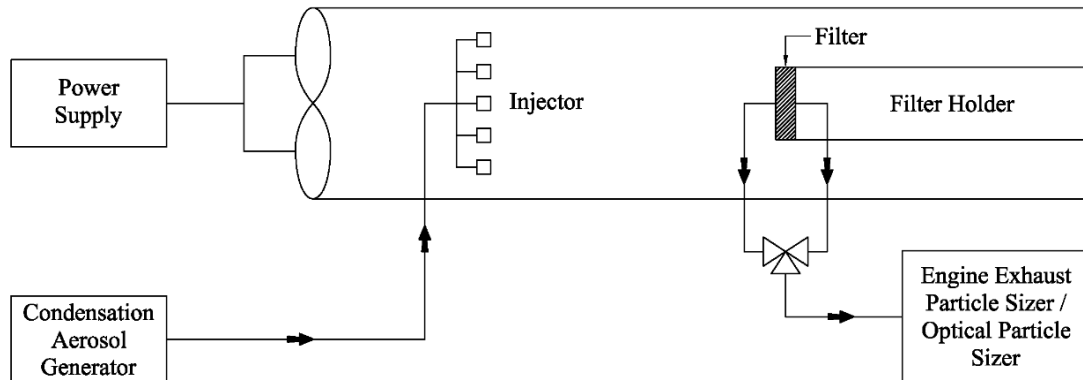


Figure 8: Schematic of air filtration experiment

C. Modeling the ventilation of the upper human body part by solving the governing equations inside the microclimate air layer

1. Literature review

Over the years, researchers were interested in measuring local ventilation of human body through clothing. Clothing ventilation is an effective way for human body to lose heat in hot environments [64]. Most literature research focused on experimentally measuring ventilation using the trace gas dilution method [64-66] and reported the average ventilation value for the clothed body surface area. Available experimental data on clothing ventilation were mainly for whole ensemble or for independent unconnected segments [67-71].

Predicting segmental clothing ventilation is important for improving garment design by modifying design parameters to enhance or decrease local ventilation rate depending on the type of clothing including protective clothing. This is why researchers have been interested in developing mathematical models from the first principles to predict local clothing ventilation. Modeling approach has mainly been based on representing the human body as a number of independent cylindrical segments covered with garment material in cross air flow [70-73]. Each clothed segment is formed by an inner cylinder representing the body skin and the outer cylinder representing the clothed garment. The segmental skin temperature is predicted from a finite element model of human thermal physiology such as a bioheat model [69-74] and is set as the

boundary condition for the ventilation model. Clothed cylinder models mimicked a limb or a trunk and the overall ventilation rate of an ensemble was obtained by summing the segmental ventilation rates[69]. However, these methods assume that segments are not connected and there is no air that flows from one segment to another which is not the case in real physical situations. Indeed, Ying et al.¹ prescribed the microclimate ventilation as the air exchange between a specific garment and the environment including three parts: air exchange between local body parts' microclimates, air exchange through the fabric with the environment, and air exchange through garment apertures with the environment. Despite the fact that ventilation includes these three processes, research focused on the effect of air exchange through fabric [66] and air exchange through garment apertures [66,69]. The ventilation through fabric is studied by modeling the flow characteristics of air penetrating through permeable jacket or by finding the overall ventilation rate experimentally by using a permeable jacket without evaluating the segmental ventilation rate⁴. Furthermore, the ventilation through garment apertures with the environment was predicted empirically by experimentation where the garment used is usually impermeable and the connections between segments were closed [64]. However, to the author's knowledge, no published experimental or analytical work has examined the impact of the air exchange between local parts on the flow characteristics of air and on the segmental ventilation rate. The studying of air flow across annular segmental connection is important when considering protective clothing design. In fact, some contaminants and toxic particles adhere with air and are transported with it. For instance, toxic aerosol particles handled by air can enter the arm from its bottom opening and can be transported upward toward the connection with the trunk. Therefore, the novelty of this work arises from studying the impact of body segment connections on the air flow characteristics in the microclimate layer and thus on estimating local ventilation rates.

In this work, the coupled mass, momentum, and heat balances including buoyancy effect are solved for the upper human body formed by three connected cylinders in cross wind. The flow over side-by-side cylinders of different diameters in cross flow for the upper trunk connection with arm was modeled as a single cylinder. The segmental skin temperature used as boundary condition is considered constant. The predicted flow characteristics and segmental ventilation rates were respectively validated by 3-D CFD analysis and by published experiments. The flow in the microclimate annuli of the trunk, sleeves and connection is simulated using the commercial software ANSYS FLUENT to validate the segmental ventilation predicted by the model. In addition segmental ventilation rates are summed and validated with published

experimental overall ventilation data. A parametric study followed to determine the design factors that enhance inter-segmental ventilation between clothed trunk and arm.

The validated model will be integrated with a multi-segmental bio-heat model to obtain accurate segmental skin boundary conditions for a given metabolic rate. Although many bio-heat models exist in the literature, a multi-segment thermally responsive bio-heat model with low computational cost is selected to accurately predict segmental skin temperature and heat losses [74, 104]. The validation of the integrated model requires developing of an improved experimental approach that finds the local clothing ventilation rate and the inter-segmental ventilation rate. The improved approach is based on a modified experimental protocol for tracer gas method to determine segmental and inter-segmental ventilation rate. Afterwards, an inter-segmental ventilation rate correlation is established as function of the influencing parameters, air permeability, wind velocity, mean air gap size between skin and clothing, and the upper clothing aperture design. Because of the facts that (1) the literature presented extensive data [101-102] on the estimation of the local ventilation rates without taking into account the inter-connection between human body segments and that (2) it is easier to experimentally measure the local ventilation while ignoring interconnection air exchanges, this study introduced a correction factor for these local ventilation rates. The relevance of this correction factor arises from the fact that estimating the local ventilation rates either analytically or experimentally requires more complexity when taking into account the inter-connection between clothed segments.

2. Mathematical Formulation

Fabric-covered cylinders provide a convenient geometry to provide the physical representation of clothed human body segments subject to cross wind. However, upper body connection through the shoulders needs to be incorporated as a connecting geometry for the microclimate air flow between the arm and trunk segments. The physical model is shown in figures 16 and 17 where the upper human body part is assumed symmetrical and is subject to external relative crosswind. The physical model is divided into four annular zones Z1, Z2, Z3, and Z4 associated with the lower human clothed arm, the upper clothed arm, the clothed trunk, and the clothed shoulder part (figure 9 and 10).

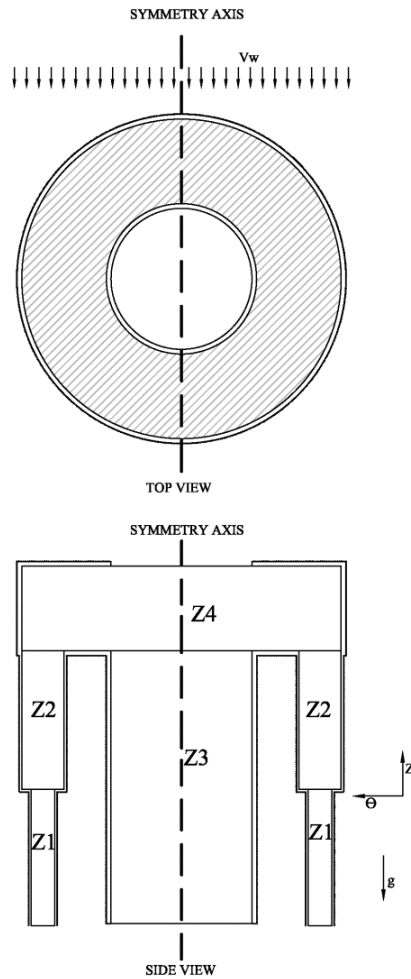


Figure 9: Physical configuration of the upper part of the human body

Forced convection around the two adjacent vertical clothed cylinders is studied according to the spacing between them. When air penetrates into clothing, it is going to flow in angular and axial directions in the air annulus separating the inner heated cylinder and the clothing. However, because of the temperature difference between the skin and the inner cylinder, natural convection plays also an important role in the air flow characteristics besides the forced convection [69, 75,76]. Mixed convection will then be studied by solving the mass, momentum and heat balances of the micro climate air annuli. The mathematical model predicts the impact of the connection between segments on the flow characteristics.

To assess the impact of the segmental connections on the flow characteristics, 3-D detailed *CFD* model is also developed using *ANSYS Fluent* 14.5 [77]. The aim of the *CFD* model is to investigate the flow of air in the microclimate air layer between the skin and the clothing and particularly in the interconnection region. The skin temperature is held constant and the flow

characteristics will be used to validate the simplified mathematical model at isothermal skin temperature.

The ventilation rates of the connected segments are compared with published experiments that aim to find the overall ventilation rates through ensembles where the connections between segments are left open [66,78].

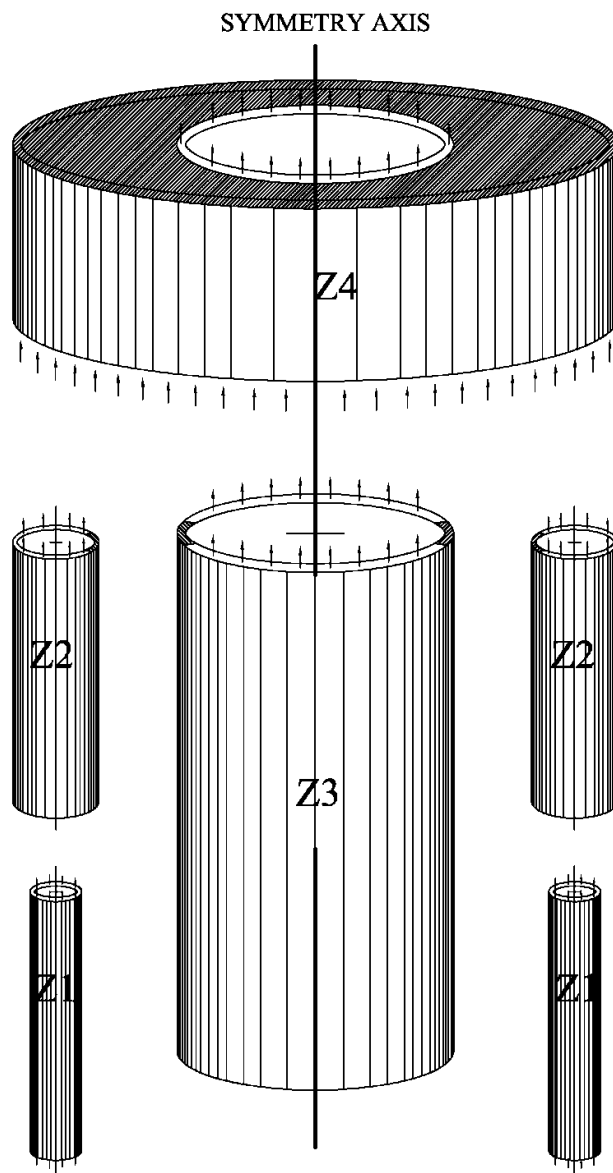


Figure 10: Blow up of the clothed segments

- a. Clothed Upper Human Body Simplified Mathematical Model
 - i. External wind flow and clothed body representation

In order to model the heat and moisture transfer of the upper part of the human body, it is important to understand the external flow field around the two adjacent vertical and clothed cylinders (see figure 9 and figure 10). Forced convection around side by side circular cylinders of same diameter is studied thoroughly in literature [78-81]. However, the human arm and human trunk present cylinders with different diameters with a diameter ratio of 0.25 between the small cylinder and the large one.

Although few studies in the literature discuss the flow past two circular diameters of different diameters [82,83], a numerical simulation of viscous flow past two circular cylinders of different diameters with similar diameter ratio was reported by Zhao et al.[84] In their work, the diameter ratio between the small cylinder and the large one was also 0.25. The gap between the small cylinder and the large cylinder ranged from 0.05 to 1.0 times the diameter of the large cylinder. They concluded that the flow behind the two cylinders can be classified into three types [84], for the very small gap ratio, there is only one wake behind the two cylinders so they are considered as a bluff single body; for the medium gap ratios, the interaction mode occurs: strong interactions exist between the vortex shedding from the large cylinder and the shedding from the small cylinder; and for very large gap ratios, the interaction between the shedding from the two cylinders becomes very weak thus the cylinders are considered as independent cylinders. According to finding of Zhao et al. [84], the flow over the arms and the trunk depended on the height considered. The gap between the small cylinder and the large cylinder ranges from 1/12 above the shoulder level to 2/3 below the shoulder level times the diameter of the large cylinder (figure 9 and 10). Therefore, the flow is considered similar to the flow around a single bluff body above the shoulder level and similar to the flow around independent cylinders below the shoulder level. For this reason, one large cylinder represents the two arms and the trunk above the shoulder level, and three independent cylinders extend downward from the large cylinder (figure 9 and 10). Each of the arm and the trunk is formed by two co-axial annuli of different inner and outer radii. The inner solid cylinder represents the heated skin and an outer cylinder represents the permeable fabric. The two cylinders are separated by few millimeters of microclimate air annulus where the flow and heat characteristics are modeled and studied.

ii. Adopted fabric model

The outer clothing cylinder is assumed to consist of a layer of fibers containing air voids. Air penetrates fabric through pores and entered to the microclimate space between skin and clothing. Water vapor is assumed to diffuse through air void space to be absorbed or desorbed by fibers

depending on the type of the fabric. In order to accurately model the fabric, we adopt the model of Ghali et al.[85] which divided the fabric into three nodes: void node representing the air within the fabric; outer node which is exposed to ambient conditions, air in void node and in microclimate air layer, inner node surrounded by the outer node. This modeling from first principles captured the heat and moisture transport in fabrics as detailed in references [68, 72, 86]. Note that the fabric three-node model lumped fabric into outer, inner and air void node. The outer node is in direct contact with the penetrating air in the void space (air void node); the inner node represented the inner portion of the solid yarn, surrounded by the fabric outer node and exchanging heat and moisture transfer by diffusion only with the outer node. Outer node exchanges heat and moisture transfer with the flowing air in the air void node and with the inner node. However, volume changes of fibers due to the sorption process are small enough and can be neglected [85]. In addition, the water vapor is assumed dilute in the air mixture.

In this work, skin is assumed exchanging heat and moisture with the microclimate air layer and radiation heat transfer with the outer node. Thus skin is considered as an interface so that there is no storage term (transient term) to be considered. As in previous researches, fully developed Poiseuille flow in both angular and axial directions were used [69] due to the small microclimate air annuli thickness which reduces the mathematical model to 1-D flow problem in two directions (angular and axial) while the radial direction is lumped.

iii. Heat and mass transport in air annulus sheathed by porous fabric

The mass, momentum, and energy balances are presented for the thin microclimate air layer trapped between the skin and clothing while taking into consideration the lumped flow in the radial direction. The mathematical formulation will be based on coupled pressure equation of mass and momentum for narrow annular flow reported in the previous work [75] that assumes fully- developed Poiseuille flow in the horizontal angular direction and fully-developed mixed buoyant upward flow [70, 72]. With these assumptions and under conditions of incompressible Boussinesq fluid of constant thermo-physical properties, the formulation of the 3-D problem of the coupled momentum and heat transfer in the vertical annulus is transformed into 1-D problem of coupled energy balance and pressure equation derived from mass and momentum equations [73, 75].

The steady state energy balance on the microclimate air layer is a balance of the convective heat and mass transfer due to the flow of air in axial, angular and radial directions, the evaporative heat transfer from the surface of the inner cylinder representing the skin, the heat

and mass diffusion from void air of the thin fabric to the air layer and the axial and angular conduction of heat in the air layer.

The water vapor mass and energy balances in the fabric void node, outer node and inner node are adapted from Ghali et al. model [85] and their derivation can be found in the published work [68, 72, 85]. The coupling to the fabric model leads to 6 equations for the fabric and air void nodes in terms for P_{v-void} , P_{v-o} , P_{v-i} which is the partial pressure of the inner vapor pressure (kPa), and the temperatures of void node, inner fabric node and outer node T_{void} , T_o , and T_i , respectively.

iii. In steady state conditions, the inner cylinder representing the skin is uniformly heated at constant heat flux representing the segmental metabolic rate with wet skin condition, w_{skin} , corresponding to saturation pressure (P_{skin}) at skin temperature (T_{skin}).

In order to solve these equations coupled to fabric nodes balances, a relation between the humidity ratio, the vapor pressure and the total pressure is needed. This relation is extracted from ASHRAE standards [88].

iv. Boundary conditions

The thermal and pressure boundary conditions at the open apertures of the arm lower end and the trunk upper side are similar to those reported by Ismail et al.[69] The main difference between this model and the previous unconnected model is that angular symmetry is no longer valid for the lower and upper arms (Z1, Z2) unlike the trunk (Z3). The cause of this asymmetry is because of the connection of the arm to the trunk modeled as one large cylinder (Z4) where the flow is redistributed.

The physical model connectivity is shown in figure 17 where (Z1) is considered as an open top and bottom annulus and the mass flow rate leaving (Z1) enters (Z2). At the end of the lower arm (Z1), and because we don't know the direction of the flow, two boundary conditions are presented:

(i) If the flow is upward through the opening, the hand can be modeled as a cylinder, thus, the pressure of adjacent layer is similar to the pressure around a solid using a Gaussian fit to the pressure distribution for a cylinder in an air flow was used [89].

(ii) If the flow is downward through the opening, the gradient of pressure is zero since the flow is leaving the domain.

The thermal boundary condition is similar to the condition considered by the literature [69, 90]. At the interface between the lower and upper arms (Z1 and Z2), we apply the continuity of the pressure, temperature, and vapor pressure. The zone Z2 is considered as an open top and bottom annulus where the mass flow rate leaving (Z1) enters (Z2) and the mass flow rate leaving (Z2)

enters (Z4). Zone Z3 is considered as open top and closed bottom cylinder where the mass flow rate leaving (Z3) enters (Z4). Because of the symmetry of (Z3), the model can be divided according to the symmetry axis shown in figure (16 and 17).

The top end of upper arm annulus (Z2) is partially opened because of the under arm region where the temperature and the humidity ratio of the air layer are considered similar to the skin conditions. The zone (Z4) is considered as open top and bottom cylinder, where the mass flow rate leaving (Z2) and (Z3) enters the bottom end while the mass flow rate leaving from the top are subjected to a discharge coefficient because of the area change and the 90° bending [91].

v. Numerical solution of simplified model

The coupled pressure and energy equations of the clothed cylinder with associated boundary conditions are discretized using a finite volume methodology. Thus, the air layer zone is divided into $N_\theta \times N_z \times 3$ grids of size Δz and $R_f \Delta \theta$ with thickness Y . Central differencing is used for second order terms in the air layer pressure and energy equations. To ensure a grid-independent solution and accurate resolution, the numerical solution is repeated for different grid sizes. In the presented simulations, the number of grid points is 100 grids for both (Z1) and (Z2) zones, 200 grids for (Z3) and 40 grids for (Z4) with a maximum $\Delta \theta$ of 1°.

vi. CFD Simulation of the Upper Clothed Human Body

In order to validate the air flow characteristics including the temperature, pressure and velocity direction and magnitude profiles at isothermal condition for the inner cylinder, a 3-D detailed *CFD* model was developed using the commercial ANSYS *Fluent* 14.5 software. The flow is considered laminar, the air is considered as an ideal gas, and the porous media is considered as a porous jump boundary condition where the hydraulic permeability is given as an input to the model.

Computational fluid dynamics (CFD) solves the governing equations for mass, momentum, and heat transfer in fluids [92, 93]. The simulations predict the flow velocity, temperature, and pressure field. To simulate air annuli of the clothed trunk and arms, computational domain has been developed using geometry and grid generation tools and utilizing symmetry to reduce domain size. To mimic the human trunk and arm, two simple cylinders clothed with 0.001 m thickness fabric layer are constructed. In order to mimic the shoulder, a small channel of 7 cm length covered with fabric relates the large diameter cylinder to the small diameter cylinder. In order to be consistent with the human body model, the lower body part is constructed as a large

clothed cylinder extended from the trunk and having the same boundary conditions (skin temperature). The geometrical dimensions of the upper human body and the jacket used in CFD are presented in table 1. The upper clothed human body part is placed in a relatively large room where the wall facing the geometry permits the inlet flow at wind speed of 0.9 m/s (wind condition).

Table 1: Basic dimensions of the upper human body and the jacket

Segment	Circumference				
	Bust cm	Waist cm	Hip cm	Neck line cm	Cuff cm
Human body size	93	74	93	35	11
Jacket size	120	110	116	38	14

Figure 11 (a) shows the geometry drawn before generating the mesh. Figure 11 (b) shows the half of the geometry in the half of the room that has to be meshed. The computational mesh generated uses approximately 1.92 million nodes where small elements (1 mm size) are used for the air gap adjacent to the human skin. The clothing is modeled as porous jump boundary condition for the outer cylinders. In laminar flows, the pressure drop across thin porous layer is typically proportional to velocity. Thus, by ignoring convective acceleration and diffusion, the porous model then reduces to Darcy's law given by

$$\nabla p = \frac{-\mu}{\gamma} \vec{v} \quad (19)$$

where γ is now the hydraulic permeability of the clothing in m^2 ; v is the velocity normal to the porous face; and ∇p is the gradient of pressure over the finite thickness.

The inputs required for the porous jump model are as follows:

- (i) Identify the porous-jump zone
- (ii) Set the hydraulic face permeability of the medium (γ in equation (19))
- (iii) Set the porous medium thickness

In order to define the hydraulic face permeability γ (m^2), the air permeability α (m/s) is used as the velocity v that is normal to the porous face, ∇p is substituted by the standard pressure change over the fabric thickness.

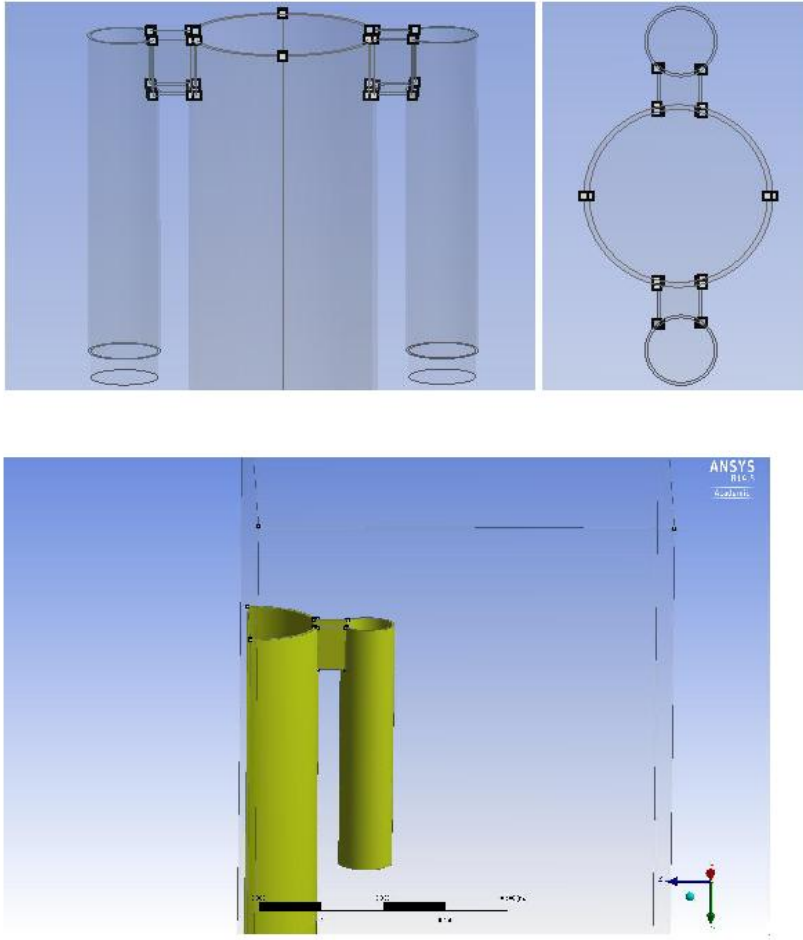


Figure 11: Plots of (a) front and top view of the upper human body and (b) symmetrical part of the domain that was simulated by ANSYS

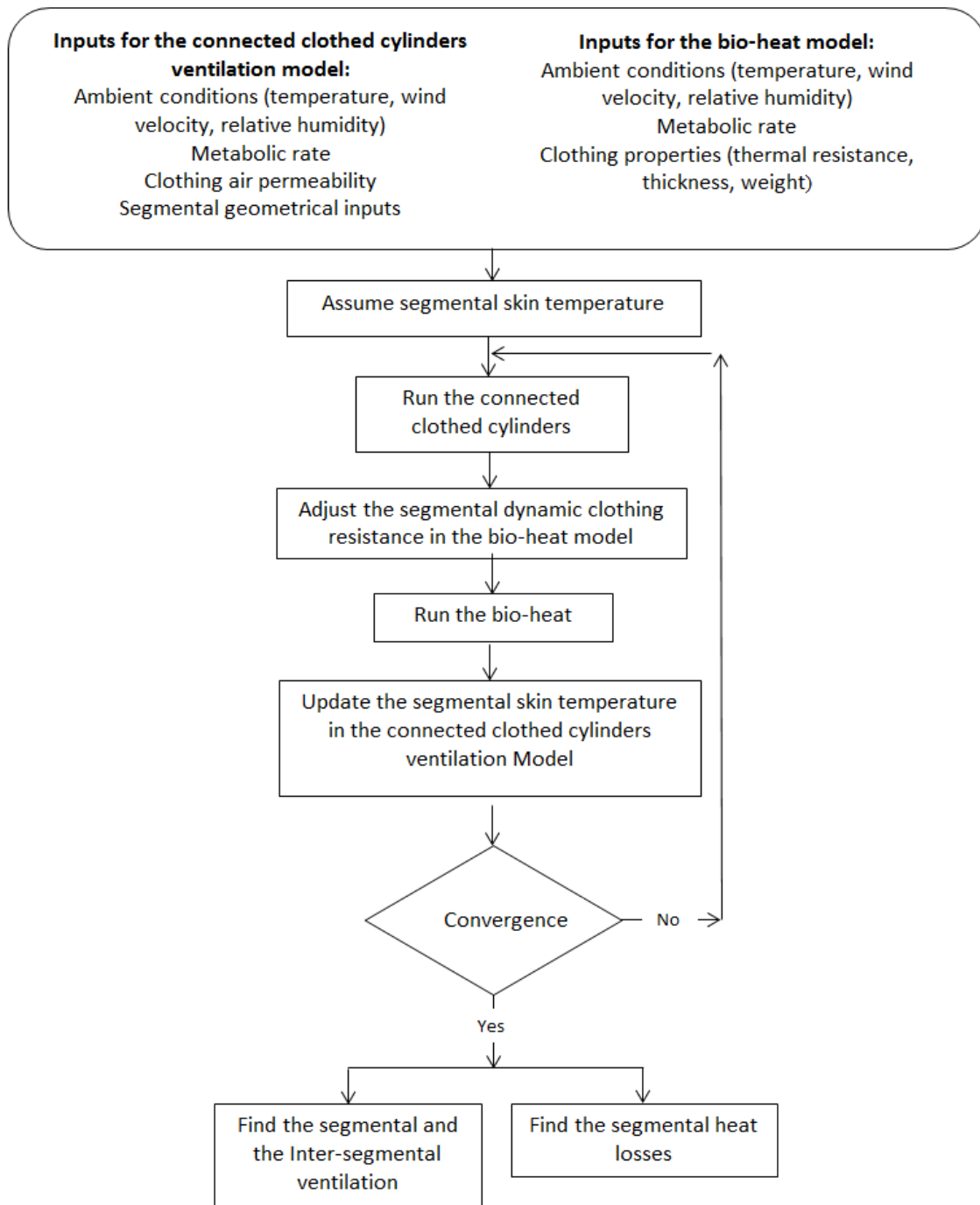


Figure 12: Flow chart of the integration methodology

vii. Integration of connected clothed cylinders' model with bio-heat model

The bio-heat model of Salloum et al. [104] is coupled through the skin boundary condition (temperature) to the connected clothed cylinders model. Each of segments (arms and trunk) has a different skin temperature [74]. The fabric used in each segment is set in the bio-heat model where the thermal properties of each fabric type play an important role in the heat transfer between the environment and the skin. The metabolic rate is set depending on the given activity

level. The ambient conditions (temperature and humidity) and external wind velocity are also required as input to the bio-heat model. After setting all these parameters in the bio-heat model, the calculated skin temperature is then used in the connected clothed cylinders mathematical model. The resulting segmental ventilation rate is entered to the bio-heat model by means of the dynamic resistance for the ventilation through fabric to predict the skin temperature [74]. The new skin temperature is used again in the connected cylinder model to predict segmental ventilation. The alternating solution between the two models is repeated until convergence in skin temperature and segmental ventilation rate is obtained between the bio-heat model and the connected cylinders model. The convergence is attained after 6 iterations and takes about 35 minutes. A flow chart detailing the methodology for solving the integrated ventilation and bio-heat model is shown in **Figure 12**.

b. Experimental methodology

The aim of the experiments is to determine local ventilation of inter-connected segments in the upper part of clothed human as well as the air exchange rate that take place at the inter-connection between the arm and trunk. Experiments are conducted on two types of jackets, one that is highly air permeable and the other is low air permeable.

For each clothing jacket case, three experiments on a thermal manikin for each of the two selected jackets using the tracer gas method with three scenarios of tracer gas injection into (i) both the clothed trunk and the arm simultaneously; (ii) for the clothed arm only; and (iii) for the clothed trunk only. In addition, a fourth experiment was conducted on the highly permeable jacket with closed connection between clothed arms and trunk while injecting the tracer gas in all segments. The purpose of the fourth experiment was to determine the difference in local ventilation when inter-connection was closed compared to values when inter-connection between the two segments was open.

i. Thermal manikin

The integrated ventilation model is validated experimentally using 20-zone “Newton” thermal manikin ¹⁷ (Measurement Technology Northwest, Seattle Washington, USA) as shown in **Figure 13**. The surface temperature or heating power of each body segment of the manikin could be controlled individually. All the thermal zones have embedded wire sensors for providing the requested skin temperature or heat flux with a standard deviation less than 0.01. The heat flux generated and associated surface temperatures are recorded during experiments at each body part by ThermDAC® software.

The system re-computes the set points and adjusts heating power every 9 seconds. The cycle repeats until the convergence of the skin temperature or heat flux requested based on human metabolic rate for a standing person [106]. In the current study, the segmental skin temperatures are extracted from the validated bio-heat model [104] and introduced to the software as was also reported by Yang et al.[107]. The local heat fluxes generated during experiment are recorded from the thermal manikin in order to approach the human body responses so that the ventilation rates are measured at realistic segmental skin temperature.

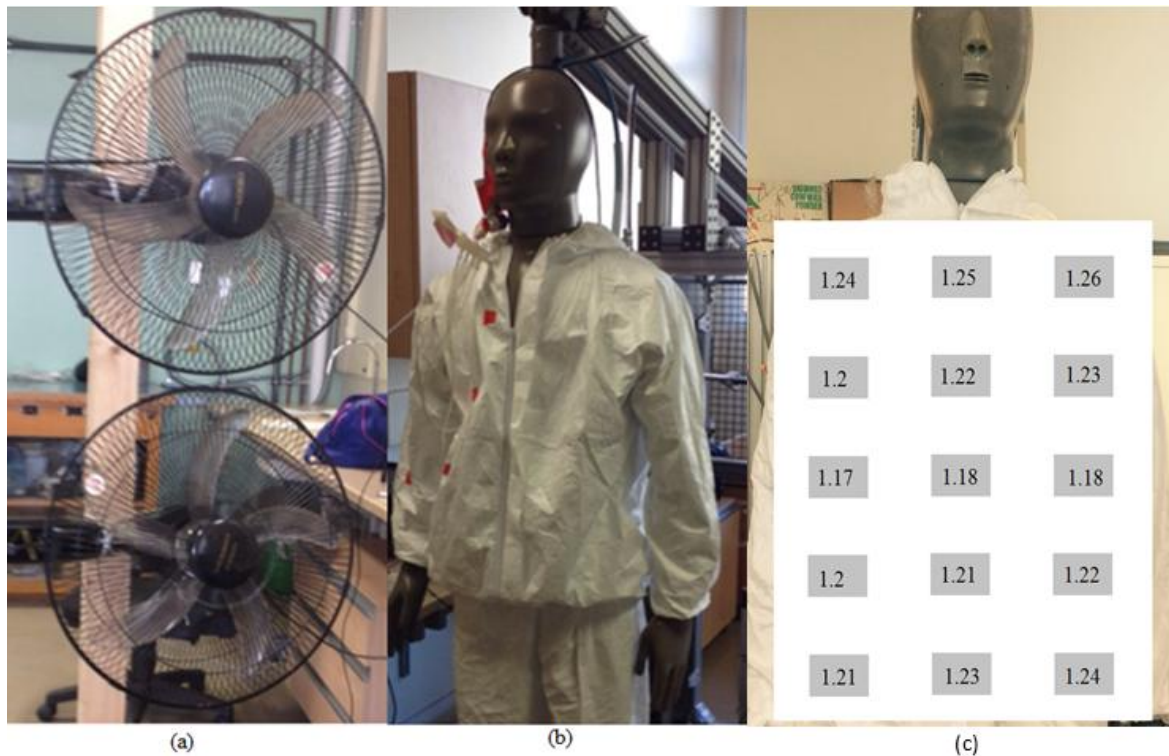


Figure 13: Test set up of the manikin (a) using two large fans and (b) using a testing jacket (c) showing the velocity distribution in m/s at a distance of 0.35 m from the manikin surface

ii. Clothing ensembles

Two commercial jackets of same medium size (Table 1) with high and low air permeability (Table 2) are selected for experimental testing. The air permeability of the fabric for each jacket are measured by SDL MO2IA air permeability tester with a standard deviation in repeated measurements of $\pm 10^{-4}$ and accuracy of $0.1 \text{ l}/(\text{m}^2 \cdot \text{s})$. Their thermal and evaporative resistances are measured using the sweating guarded hotplate (Model 306-200/400). The thermal insulation is also measured by the thermal manikin during the experiment. The lower part of the thermal manikin is dressed with the same clothing material of same properties of the upper part. The lower part is closed at the waist level by a tight belt in order to not allow

any air exchange from the lower part to the upper part. In addition, the gradient in temperature between the upper and lower parts at the waist level is relatively small, so that the conductive effect between these two parts is neglected.

iii. External Wind and Climatic Room Conditions

Two large fans with a diameter of 0.5 m are installed vertically on a stand with controllable wheels to adjust the distance between the manikin and the fans stand for the desired velocity at the front side of the manikin. The stand center is placed on the same horizontal line that passes through the upper body part center (trunk center) to provide a symmetry flow around it. The distribution of wind speed is measured by the manikin wind speed sensor which is an air velocity transducer (model 8475-06) at 3-min intervals at twelve locations as shown in **Figure 13 (c)** at a distance of 0.35 m from the manikin surface. The stand of the fan is moved away from the manikin so that the mean value of the twelve measured wind speed velocities is about 1.2 ± 0.015 m/s. It is shown in **Figure 13(c)** that the wind speed distribution is uniform along the height and the width of the upper human part with a maximum relative error of 7% between the maximum wind speed and the minimum wind speed.

The manikin and the fans are both placed in an environmental chamber. The chamber air temperature is measured by two manikin sensors at different heights (0.9 m and 1.6 m) and the average is about $24 \text{ }^\circ\text{C} \pm 0.2 \text{ }^\circ\text{C}$. The relative humidity is measured at 1.6 m height and it is about $40 \pm 3 \%$.

Table 2: Properties of the jackets used in the experiments

Jacket	Material and composition	Thickness (mm)	Weight (g/m ²)	Air permeability (m/s)	Dry resistance ($^\circ\text{C}\cdot\text{m}^2/\text{W}$)	Evaporative resistance ($\text{Pa}\cdot\text{m}^2/\text{W}$)
Sport jacket	100% polyester	2.3	263 ± 1	0.09 ± 10^{-4}	0.056 ± 10^{-5}	10.48 ± 0.05
Low air permeability jacket	High density polyethylene	0.1	75 ± 1	0.02 ± 10^{-4}	0.018 ± 10^{-5}	22.57 ± 0.05

iv. Tracer Gas Method

The tracer gas method is applied only at the upper clothed part [64]. Nitrogen is the selected tracer gas since it is safe, non-reactive, insensible gas and it has the same properties of dry air. Since dry air is a mixture of nitrogen and oxygen and other components of relatively low percentage ($C_{O_2}(\%) = 100(\%) - C_{N_2}(\%) - C_{other}(\%)$), thus any variation of the Nitrogen concentration affects the Oxygen concentration. Therefore, measuring oxygen concentrations allows us to calculate tracer gas concentration accurately.

Figure 14 shows the schematic diagram of our experimental setup that estimates the ventilation based on the tracer gas methods of Ke et al. [64] for local clothing ventilation measurement. Two oxygen sensors of 2 % accuracy and a standard deviation of ± 0.01 are mounted in line at the inlet and outlet flow to and from the manikin microclimate air layer. A diaphragm pump (2-5 l/min) is used to circulate the extracted air from the manikin. The flow of air is controlled and measured by an air flow controller (0-5 l/min). Another flow controller (0-1 l/min) is mounted at the top of the Nitrogen tank. The current experimental method/protocol to estimate local ventilation differs from that of Ke et al. [64] in the following aspects:

- (i) Nitrogen gas is used as tracer gas instead of Argon tracer gas;
- (ii) the inter-connection openings in the upper human body part are left open; and
- (iii) with the added amount of nitrogen gas, the concentrations of oxygen gas are recorded at the inlet and outlet flow to and from the manikin microclimate.

Taking advantage of symmetry, the distribution flow and the sampling flow are provided using tubes sealed to the right arm (or left), and half of the chest of the thermal manikin and perforated with holes of 1 mm diameter. The inlet flow and outlet flow are controlled to 1.6-2.3 l/min while the added Nitrogen flows are 0.2 l/min and 0.3 l/min. The values of flows are chosen depending on the jacket air permeability in order to be insignificant compared to the clothing ventilation.

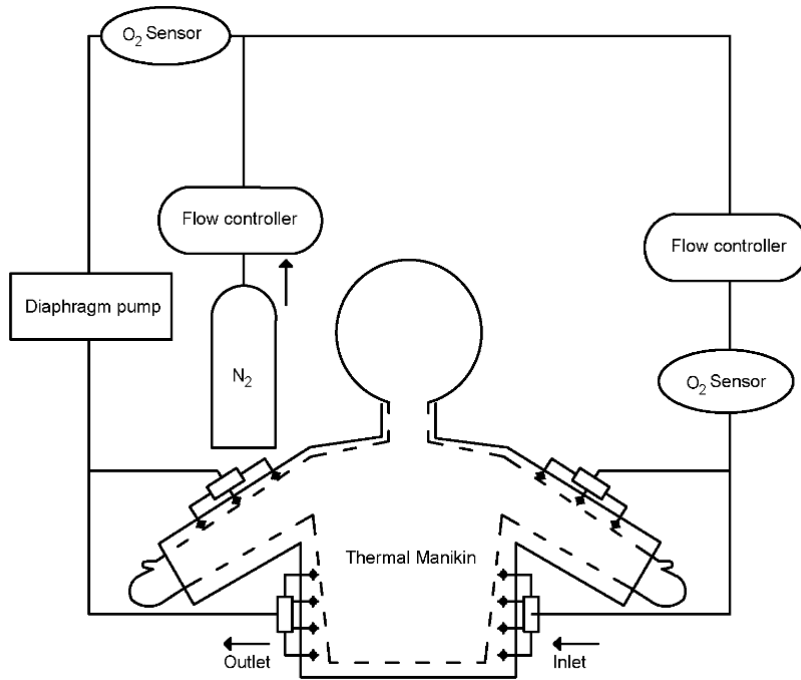


Figure 14: Schematic diagram of the experimental set up

The thermal manikin is turned on at segmental skin temperature extracted from the validated bio-heat model where the metabolic rate of 1.2 MET is given as an input. Once the heat fluxes generated during experiments from each segments stabilized, the Nitrogen tank is opened, and the flow controller mounted at the top of the tank is calibrated to the desired Nitrogen flow. The diaphragm pump is switched on and extracted air depending on the flow rate specified by the air flow controller. The N_2 gas is premixed with air in a small zone chamber before going into clothing microclimate so that the tracer gas injected at ambient condition becomes instantaneously dispersed within the zone [106].

The mixed air and Nitrogen are injected at the front side and extracted at the microclimate conditions from the back side. The experiment is repeated until the steady state conditions of the recorded inlet and outlet concentrations and the heat losses of the thermal manikin are reached. The circulated mass flow rate, the inlet and outlet concentration values are recorded. Their values are used to solve the ventilation rate and inter-segmental ventilation rate equations. For the case of low air permeability fabric, the mass flow rate injected is controlled to be 1.6 l/min including 0.2 l/min of Nitrogen. For the case of high air permeability fabric (sport wear clothing), the mass flow rate injected is controlled to be 2.3 l/min including 0.3 l/min of Nitrogen flow. The steady state is reached after 80 minutes for the high permeable fabric: 20 minutes for the model initialization and 60 minutes for the remaining part of the experimental procedure. In

the case of low permeable fabric, the steady state is reached after about 100 minutes: 20 minutes for the model initialization and 80 minutes for the remaining experimental procedure for N₂ injection. To ensure that results are independent of injection and extraction locations of inlet and outlet tubes, the experiment is repeated on the high air permeable jacket while placing two inlets and two outlets in the front and two inlets and two outlets at the back and concentrations are recorded after steady state conditions are reached in 80 minutes under same ambient nitrogen flow conditions. There was no significant difference between recorded concentrations at steady state when the locations of injection and extraction tubes were changed. The difference in concentration was less than 0.05 %.

Mass balances of tracer gas method, for determining overall and local ventilation through upper human body part were done by either neglecting inter-segmental ventilation rate altogether [66,77] or by closing the connection between human arm and trunk [64]. In this protocol, simultaneous injection of N₂ gas is performed into both the arm and trunk and concentrations of O₂ are measured for inlet and out flows into the microclimate. The tracer gas mass balance for the microclimate ventilation for overall ventilation of upper body [108] or disconnected segment is given by

$$\dot{q}_{in-out} C_{in} - \dot{q}_{in-out} C_{out} + \dot{q}_{vent} C_{air} - \dot{q}_{vent} C_{out} = 0 \quad (20)$$

where \dot{q}_{in-out} is the circulating mass flow rate (*l/min*), C_{in} and C_{out} are the O₂ concentrations of the garment inlet and outlet flow (%), \dot{q}_{vent} is the microclimate ventilation rate (*l/min*), C_{air} is the oxygen concentration of the atmosphere. Then, the microclimate overall ventilation for negligible inter-segmental ventilation rate is then calculated as

$$\dot{q}_{vent} = \frac{\dot{q}_{in-out}(C_{in} - C_{out})}{C_{out} - C_{air}} \quad (21)$$

One experiment is performed on the high permeable fabric ($\alpha=0.09$ m/s) while the inter-connection between the arm and trunk is closed and the experiment is repeated three times to ensure accurate results when inter-segmental ventilation rate is prevented. This provides a baseline measure for the significance of the inter-connection on local ventilation.

v. Measurement and calculation of inter-segmental and local ventilation rates

A modified experimental protocol for tracer gas method is followed to determine segmental and inter-segmental ventilation rates. The method includes three experiments and the calculation

method adds new mass balances to replace equations (20) and (21) since we have three unknown parameters that require estimation. These three parameters are the microclimate ventilation of the trunk ($\dot{q}_{vent-trunk}$), the inter-segmental ventilation rate (IS) due to connection, and the microclimate ventilation of the arm, ($\dot{q}_{vent-arm}$) as shown in Figure 15. In addition to the introduction of the inter-segmental ventilation rate as a new parameter, the direction of inter-segmental ventilation rate (from the trunk to arm or vice versa) is not known. The three experiments are as follows: i) the first one follows the experimental protocol that includes simultaneous injection of Nitrogen with the air flow entering the microclimate air of the arm and the trunk; ii) the second experiment involves injecting the excess nitrogen to the arm and tracks its impact on the concentration of oxygen in the clothed trunk segment; and iii) the third experiment involves injecting the excess nitrogen to the trunk and tracked its impact on the concentration of oxygen in the clothed arm. Each experiment is applied to both ensembles and is repeated at least three times to ensure that the test variability is lower than 5%.

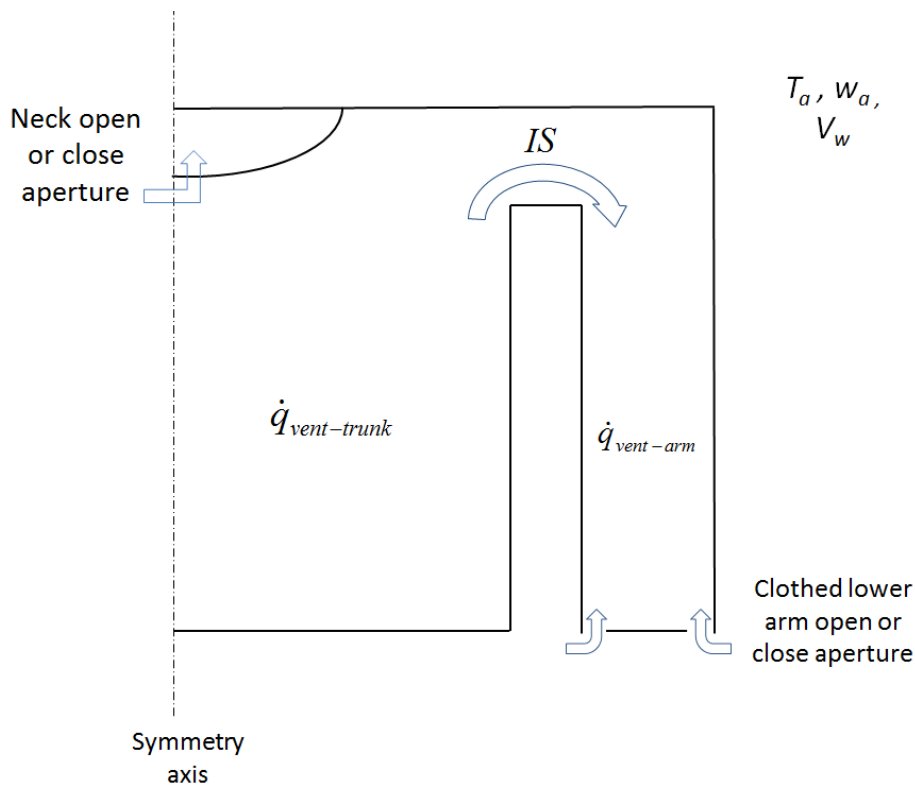


Figure 15: Schematic diagram of the three unknown parameters

In the first experiment, the Nitrogen is injected with the air flow entering both the arm and the trunk microclimate air layers. Since inter-segmental ventilation rate should be accounted for in the calculations, the tracer gas equation (21) for the arm is modified to become as follows:

$$\dot{q}_{in-out} C_{in-arm} + \dot{q}_{vent-arm} C_{air} + [\max(IS,0)] C_{out-trunk} = [\dot{q}_{in-out} + \dot{q}_{vent-arm} + \max(IS,0)] C_{out-arm} \quad (22)$$

where \dot{q}_{in-out} is the circulating mass flow rate (l/min), $\dot{q}_{vent-arm}$ is the microclimate ventilation rate (l/min) of the arm, IS is the inter-segmental ventilation rate (l/min) leaving the trunk to the arm, C_{in-arm} and $C_{out-arm}$ are respectively the O_2 concentrations of the arm inlet and outlet flow (%), C_{air} is oxygen concentration in the atmosphere (%), and $C_{out-trunk}$ is the O_2 concentration of the trunk outlet flow (%). Similarly, the tracer gas equation for the trunk is given by

$$\dot{q}_{in-out} C_{in-trunk} + 0.5\dot{q}_{vent-trunk} C_{air} + [\max(-IS,0)] C_{out-arm} = [\dot{q}_{in-out} + 0.5\dot{q}_{vent-trunk} + \max(-IS,0)] C_{out-trunk} \quad (23)$$

where \dot{q}_{in-out} is the circulating mass flow rate (l/min), $\dot{q}_{vent-trunk}$ is the microclimate ventilation rate (l/min) of the trunk, $C_{in-trunk}$ and $C_{out-trunk}$ are respectively the O_2 concentrations of the trunk inlet and outlet flow (%), and $C_{out-arm}$ is the O_2 concentration of the arm outlet flow (%).

Two additional equations are derived from single segment injection experiments three and four to solve for the three unknowns ($\dot{q}_{vent-trunk}$, IS , and $\dot{q}_{vent-arm}$) and to determine IS direction from arm to trunk or vice versa. Thus, one segment is injected with N_2 while examining the concentration in the other non-injected segment. If the outlet concentration of the non-injected segment is below the atmospheric value, this means that a specific amount of air is being driven from the injected segment to the non-injected segment through the connection of the segments. Otherwise, the inter-segmental ventilation rate is either null or in the opposite direction. Equations are derived for the single segment injection experiment depending on the direction of the flow as follows:

- Trunk tracer gas equation when excess nitrogen is injected in the arm microclimate (second experiment):

$$0.5\dot{q}_{vent-trunk} C_{air} + [\max(-IS,0)] C_{out-arm} = [0.5\dot{q}_{vent-trunk} + \max(-IS,0)] C'_{out-trunk} \quad (24 a)$$

(if $C'_{out-trunk} < C_{air}$)

- Arm tracer gas equation when excess nitrogen is injected at the trunk microclimate (third experiment):

$$\dot{q}_{vent-arm} C_{air} + [\max(IS,0)] C_{out-trunk} = [\dot{q}_{vent-arm} + \max(IS,0)] C'_{out-arm}$$

(if $C'_{out-arm} < C_{air}$)

(24 b)

where $C'_{out-trunk}$ is the O₂ concentration of the trunk in the outlet flow (%) after the injection of the arm, while $C'_{out-arm}$ is the O₂ concentration of the arm in the outlet flow (%) after the injection of the trunk.

Solving equations (22), (23), and (24 a) or (24 b) leads to determining segmental ventilation experimentally in the arm, trunk and the inter-connection ventilation.

D. Simplified Model of Ventilation and heat losses using an electric circuit analogy

1. Literature review

Energy exchange between the human body and its thermal environment have been investigated by several researches interested in human thermal comfort in different applications including physiology, engineering, architecture, psychology and meteorology [113]. The quantification of the energy exchange between the human body and its environment is a complex task since any model developed for this purpose must find a balance between the physiological characteristics of human body and the environment conditions [114]. The heat exchange between human body and the environment is significantly influenced by the way the clothing layers mediate the flow of heat and moisture from the human skin to the environment. This exchange occurs either by diffusion in fabric and air layers or by ventilation induced by relative wind or walking condition resulting in air penetration through the fabric to microclimate air trapped between skin and fabric [115]. In fact, when a person is dressed, the process of heat exchange between human body and the environment becomes complex [116]. When human skin releases heat and moisture, some goes through clothing material, and the other is transferred from the microclimate air layer by ventilation. Since the clothing outer surface is exposed to the environment, conduction, convection and radiation mechanisms help in heat transfer while diffusion, absorption, and evaporation mechanisms help in moisture transfer.

Researchers have modeled the thermal response of the clothed human body by either considering the clothing as static resistance [117] or by considering the dynamic properties of fabrics [118]. Recently, researchers reported that clothing ventilation at elevated speeds played a critical role in removing sensible and latent heat from the body to the environment [115, 119]. Havenith et al. [120] found that clothing ventilation can cause up to 50% reduction in thermal insulation and up to 88% reduction in evaporative resistance depending on the level of activity. Therefore, modeling the heat and mass transfer of the clothed human body to environment necessitates the knowledge of the ventilation rate.

In order to predict the heat and moisture transfer from the human body, Lotens [121] developed a steady-state heat resistance network model that describes all the mechanisms of heat and moisture transfer from the skin to the environment. The network included all the mechanisms in addition to the dynamic resistance that takes into account the change in the dry and evaporative resistance due to clothing ventilation. The heat and moisture heat resistance network has then been used in different studies to find the heat losses in different conditions. For instance, Ghali et al. [122] incorporates the effect of ventilation induced by swinging motion of clothed cylinder in uniform wind to the Loten's simple heat resistance network model to predict the mean steady periodic heat loss from the clothed cylinder. However, the used ventilation model was complex. It was based on solving the mass and momentum conservation equations inside the microclimate air layer between the skin and the clothing [123, 124]. Furthermore, it took into account the effect of walking conditions by investigating the swinging motion of a clothed limb [115, 122, 125-127]. Although these mathematical models succeeded in predicting the segmental ventilation rates through clothing; however, they necessitated significant computational cost which made them difficult to be integrated with other thermal models to predict the segmental heat losses. Therefore, it is of interest to generate a more simplified ventilation model of clothed walking human body that can be used as an interactive tool in different applications related to clothing design and thermal comfort while being easily coupled with bio-heat models. Developing such interactive tool for estimation of static and dynamic clothing ventilation under wind and motion must have the feature of accommodating different wind conditions, different postures (standing or walking), and different clothing apertures (open or closed to environment). Furthermore, such a tool must be represented in a simplified and conceptually understood method that captures the physics to be easily adopted and integrated with other models such as the segmental bio-heat model. In this study, an analogy is adopted between

the air flow inside the air gap and an electric circuit, this analogy has been widely used in the literature. Indeed, researchers have approached the problem of modeling the air flow in channels and complex geometries using an electrical circuit analogy because the electric circuit analogy is easily understood and explained. The analogy is based on considering that the pressure difference and the flow rate are similar to the potential voltage difference and the electric current respectively. To the authors' knowledge, modeling clothing ventilation via electric circuit analogy has not been reported in literature.

In this work, the pressure driven flow is studied in the microclimate air layer of the clothed human segment. This air flow is resisted by the viscous resistance inside the air layer and by a fabric resistance through the clothing layer. Moreover, if the clothed human segment is oscillating and the volume of air inside the microclimate air layer is changing, this will cause a variation of the air flow rate. Therefore, the analogy of the ventilation flow to the electric circuit is represented by an electric resistance describing the resistance to the air flow and by an electrical inductance describing the resistance to the change in air flow rate if oscillation occurs. The fluid flow expressions for resistance and inductance can be derived directly from the mathematical model permitting the use of electrical circuits' analysis tools for their fluid analogies. Therefore, in this work, a simplified model has been developed. This model is based on an analogy between the air flow inside the air gap and through the fabric with an electric circuit. The model considered different conditions of external wind and swinging motion of different clothed fabric segments representing the limb or the trunk. The model is then coupled to the heat resistance network to find the segmental heat losses. The natural convection is then added to study its effect on segmental ventilation. Then, the inter-segmental ventilation is taken into account to find accurately the segmental ventilation.

2. Mathematical Formulation

The upper human body consists of several clothed segments representing the clothed arm (lower and upper), the clothed trunk that could be divided into chest and shoulder. In order to model each clothed segment, fabric-covered cylinders provide a convenient geometry to represent the clothed human body segments subjected to cross wind and walking conditions. However, upper body connection through the shoulders needs to be incorporated as a connecting geometry for the microclimate air flow between the arm and trunk segments.

a. Independent clothed segment

The physical configuration of independent clothed segments consists of a clothed annulus surrounding a heated cylinder representing the clothed arm [116,120] as shown in Figure 16. The fabric covered cylinder has a radius r and height H . The air layer trapped between the concentric fabric and skin cylinder is of thickness Y and it separates the inner solid cylinder maintained at a constant skin temperature T_{skin} and the outer porous cylinder represented by an isotropic fabric layer of permeability α and thickness ef . The clothed cylinder could experience an oscillating motion simulating the swinging motion of arms during walking [132]. The oscillating motion induces air to enter from the segment side exposed to windy condition (front side) and to leave from the other side (back side). Therefore, the physical configuration consists of dividing the microclimate annulus of the clothed segment into two parts: the front side having P_{front} and T_{front} and the back side having P_{back} and T_{back} reducing the pressure and temperature angular variations to two lumped nodes.

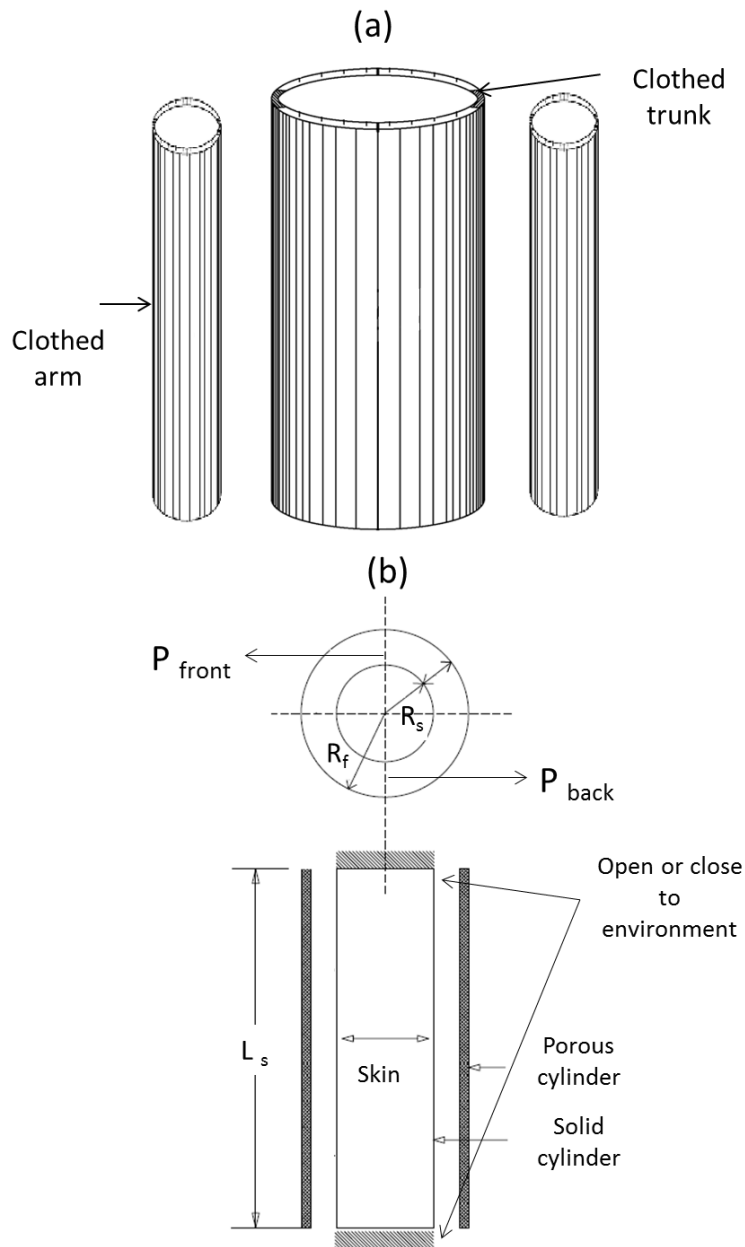


Figure 16: Physical configuration of (a) disconnected upper human body segments (b) fabric clothed segment

In this section, the electric circuit analogy for independent segments is presented. The work is based on Ismail et al. [131] study where a simplified ventilation model of clothed human body segments is generated to estimate the segmental ventilation rates of clothed segment experiencing walking and/or windy conditions by using an analogy with an electric circuit. The clothed arm experiences sinusoidal up and down motion in contrary with the trunk that stays at rest. The oscillating motion of the clothed arm is divided to two phases. In phase I,

the human skin (inner cylinder) swings without touching the porous media (outer cylinder) forming an angle ϕ smaller than the angle at which contact occurs ($\phi_{contact}$) while, in phase II, the human skin and fabric swing together to a maximum angle ϕ_{max} . The contact angle is defined as function of the initial microclimate air layer size of the arm (Y_{a-0}) to the arm height (H_{a-s}) as following:

$$\phi_{contact} = \tan^{-1} \frac{Y_{a-0}}{H_{a-s}} \quad (25)$$

When the angle ϕ reaches $\phi_{contact}$, Phase I terminates. During Phase II, the skin touches the fabric and they swing together reserving the same air layer thickness. In Phase II, the maximum angle that the fabric and skin reach is ϕ_{max} . Therefore, a sinusoidal angular position ϕ can be assumed for the swinging motion at a rotational speed ω related to the frequency of motion f :

$$\phi = \phi_{max} \sin(\omega t) \quad (26)$$

Therefore, the air layer thickness Y at any spatial position is given by:

$$\text{Phase I: } Y_a(x, \theta, t) = Y_{a-0} - (H_a - x) \tan \phi \cos \theta \quad (27a)$$

$$\text{Phase II: } Y_a(x, \theta, t) = Y_{a-0} - (H_a - x) \tan \phi_{contact} \cos \theta \quad (27b)$$

By integrating equations (27 a) and (27 b) over the front side angle ($-\pi/2$ to $\pi/2$) and the back side angle ($\pi/2$ to $-\pi/2$), and over the segment arm length H_s , and by considering that the oscillation angle ϕ is very small in Phase I as well as the contact angle $\phi_{contact}$, the equation of the air layer thickness Y becomes:

$$\text{No-touch region (Phase I): } \bar{Y}_a(t) = Y_{a-0} - \frac{H_a}{\pi} \phi_{max} \sin(\omega t)$$

(27c)

$$\text{Touch region (Phase II): } \bar{Y}_a = Y_{a-0} - \frac{H_a}{\pi} \phi_{contact}$$

(27d)

Phase I: Air gap size changing with time

Because the annulus trapped air thickness Y is small compared to the cylinder length H_a and the inner radius cylinder R_s , the assumption of Plane transient-Poiseuille flow in axial and

angular directions is valid. Thus, the velocity v has also a parabolic profile in the radial direction y given by:

$$v(t) = k(y\bar{Y}_a(t) - y^2) \quad (28)$$

where k is a factor that depends on the initial condition of velocity in each direction (k_x in axial direction and k_θ in angular direction). By integrating over the corresponding cross section, the air flow rate in the axial direction is given by:

$$Q_{a-x}(t) = k_x \pi r_a \frac{Y_a^3(t)}{6} \quad (29a)$$

$$Q_{a-\theta}(t) = k_\theta H_a \frac{Y_a^3(t)}{6} \quad (29b)$$

As mentioned before, k_x and k_θ are factors that depend on the initial condition, thus they are calculated from the fact that at $t = 0$, $Q_{a-x}(0) = Q_{a-0}$ and $Q_{a-\theta}(0) = Q_{a-0}$, and are given by the following:

$$k_x = 6 \frac{Q_{a-0x}}{\pi r_a Y_{a-0}^3} \quad (30a)$$

$$k_\theta = 6 \frac{Q_{a-0\theta}}{H_{a-s} Y_{a-0}^3} \quad (30b)$$

Applying now the Navier-Stokes equation in axial and angular directions will result in the following momentum equations:

$$x\text{-direction: } \rho \frac{\partial v_x}{\partial t} = -\frac{\partial P_{a-x}}{\partial x} + \mu \frac{\partial^2 v_x}{\partial^2 y} \quad (31)$$

$$\theta\text{-direction: } \rho \frac{\partial v_\theta}{\partial t} = -\frac{\partial P_{a-\theta}}{r_a \partial \theta} + \mu \frac{\partial^2 v_\theta}{\partial^2 y} \quad (32)$$

By differentiating the velocity given in equation (29) with respect to t and y , and by substituting the air flow rate of equations 29(a) and 29(b) in the momentum equations after integration over the corresponding cross-section, equations 31 and 32 become respectively as

$$\Delta P_{a-x} = \frac{12\mu H_a}{\bar{Y}_a^3(\pi r_a)} Q_x + \frac{\rho H_a}{\bar{Y}(\pi r_a)} \frac{dQ_{a-x}}{dt} \quad (33)$$

$$\Delta P_{a-\theta} = \frac{12\mu(\pi r_a)}{\bar{Y}_a^3 H_a} Q_{a-\theta} + \frac{\rho(\pi r_a)}{\bar{Y}_a H_a} \frac{dQ_{a-\theta}}{dt} \quad (34)$$

$$\Delta P_{a-r} = Q_{a-r} \frac{\Delta P_m}{\alpha \pi r_a H_a} \quad (35)$$

where ΔP_{a-x} , $\Delta P_{a-\theta}$, ΔP_{a-r} are respectively the pressure drop in the axial, angular and radial directions of the clothed arm; Q_{a-x} , $Q_{a-\theta}$, Q_{a-r} are respectively the air flow rates in the axial, angular and radial directions for the clothed arm; α is the fabric air permeability expressed in m/s tested at a pressure drop $\Delta P_m = 0.1245 \text{ kPa}$ from standard tests on fabrics' air permeability [135]. Eq. (33) and (34) are similar to the voltage equation across a resistance and inductance in series, while Eq. (35) is simply similar to the voltage equation across a resistance.

Applying the conservation of mass, the variation of the volume inside the microclimate air layer $r_a H_a dy_a/dt$ is then equal to the mass flow rates Q_{a-x} , $Q_{a-\theta}$, Q_{a-r} in axial, angular and radial directions respectively as follows:

$$Q_{a-r} + Q_{a-x} + Q_{a-\theta} - r_a H_a \frac{dy_a}{dt} = 0 \quad (36)$$

Eq. (36) is similar to Kirchoff's first law that states the principle of conservation of electric current by declaring that the algebraic sum of currents in a network meeting at a point is zero. The back side of the clothed arm has the same momentum equations except that $Q_{back} = -Q_{front}$; the main reason is that if the air gap size increases at a time t on the front side of the clothed segment, the back air gap size will decrease by the same amount at the same time t .

Independent clothed trunk: In walking conditions, the clothed human trunk air gap size is not changing with time because the trunk does not experience an oscillating motion when the human body is walking; however, the walking speed of the human body affects the relative wind. Therefore, the flow of air is only induced by the relative wind velocity given by the following equation:

$$V_r = V_w \pm V_{walk} \quad (37)$$

By assuming Poiseuille flow model in the angular and axial direction [121], and by integrating the angular and axial Navier-Stockes equations over the corresponding cross-section, the pressure difference equations are given by:

$$\Delta P_{t-x} = \frac{12\mu H_t}{Y_t^3 (\pi r_t)} Q_{t-x} \quad (38)$$

$$\Delta P_{t-\theta} = \frac{12\mu(\pi r_t)}{Y_t^3 H_t} Q_{t-\theta} \quad (39)$$

Moreover, the air flow in the radial direction is through the permeable fabric covering the human body. The radial flow is penetrating or leaving through the fabric depending on the pressure difference between the outside and the microclimate air layer. Thus, the radial pressure difference is given by the following equation:

$$\Delta P_{t-r} = Q_{t-r} \frac{\Delta P_m}{\alpha \pi r_t H_t} \quad (40)$$

On the other hand, given that the microclimate air layer is formulated as an incompressible fluid, the conservation of mass in the microclimate air layer of the clothed human trunk is given by:

$$Q_{t-r} + Q_{t-x} + Q_{t-\theta} = 0 \quad (41)$$

Equations (39-40) are similar to the potential equation of the voltage difference across an electric resistance. Thus, there is an analogy between the air flow inside the microclimate air gap of the trunk subjected to external wind on axial, angular, and radial directions and the resistance electric circuit.

Therefore, the electrical networks representing the air flow inside the microclimate air layer of the clothed segment subject to external wind and oscillating motion for an independent clothed arm and trunk are shown in **Figure 17(a) and 17(b)** where the pressure P_{a-o1} and P_{t-o1} are estimated from the pressure coefficient distribution around a solid cylinder of the arm and the trunk respectively, the pressure P_{a-o2} and P_{t-o2} are estimated from the data of Fransson et al. [136] on the pressure coefficient distribution around a circular cylinder representing the arm and the trunk respectively with suction or blowing in radial direction. $P_{a-front}$ and $P_{t-front}$ are the pressure in the front side of the arm and the trunk respectively, while P_{a-back} and P_{t-back} are the pressure in the back side of the arm and the trunk respectively. In Figure 17 (a), the switches S_1 and S_2 are closed so that the inductance does not have any role in the electric circuit when the inner cylinder representing the skin touches the clothing layer, the two cylinders swing together and the air gap size becomes unchanged with time.

Although this model succeeds in predicting the segmental ventilation [130], the model needs to account for the effect of inter-segmental ventilation where the clothed segment will not

be considered independent and hence the electric circuit of trunk and upper arm are now connected.

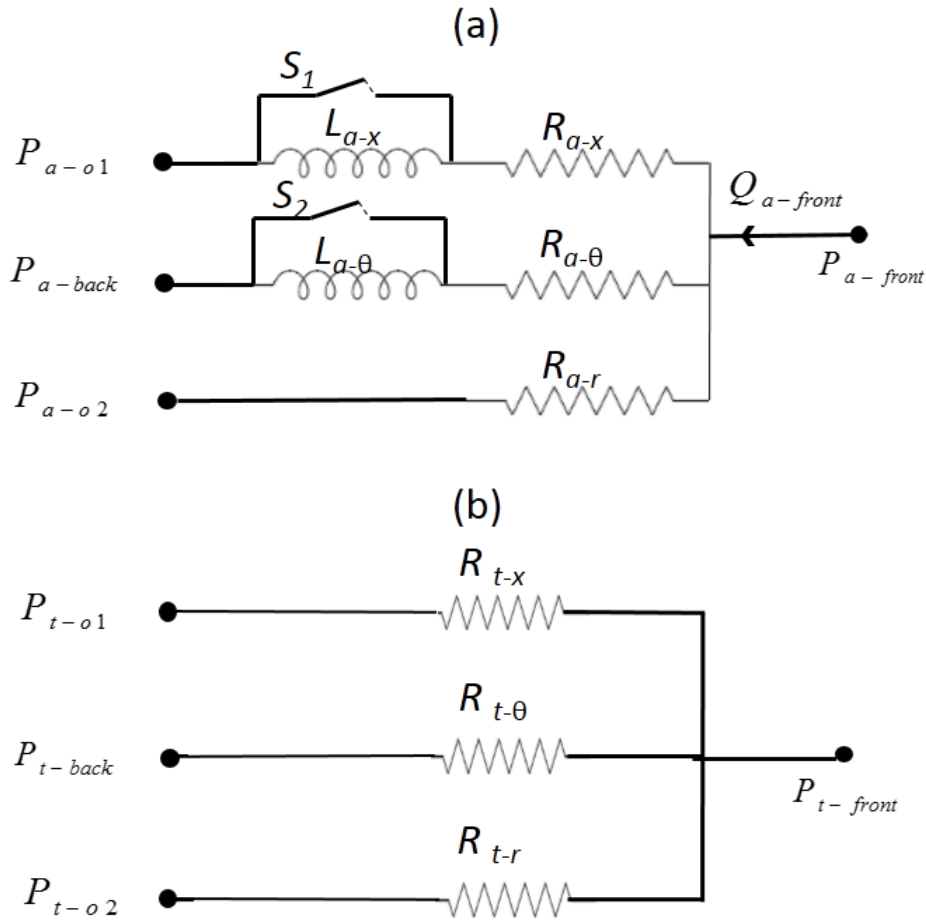


Figure 17: Network representing the analogy of the air flow inside the microclimate air layer of (a) clothed oscillating arm (b) clothed trunk subjected to external wind

b. Inter-connected clothed upper human body

The physical configuration adopted in this section focuses on the upper human body and represents it as one large cylinder representing the two arms and the trunk above the shoulder level, and three independent cylinders extending downward from the large cylinder (**Figure 18**). Ismail et al. [118, 119] adopted this physical configuration after studying the flow past two cylinders of different diameters for sedentary case. Accordingly, they found that the flow is considered similar to the flow around a single bluff body above the shoulder level and similar to the flow around independent cylinders below the shoulder level. This is due to the

gap separating the large cylinder representing the trunk and the small cylinder representing the arm. Thus, in this study, the methodology used by Ismail et al. [118,119] is extended to be more general so that it will be applied to walking conditions. The physical model is shown in **Figure 18** where the upper human body part is assumed symmetrical and is subject to external relative crosswind. The physical model is divided into eight annular zones LF, BF, UF, UB, TF, TB, SF, SB associated respectively with the lower human clothed arm in front and back sides, the upper clothed arm in front and back sides, the clothed trunk in front and back sides, and the clothed shoulder part in front and back. Each annular cylinder consists of a porous cylinder surrounding a heated cylinder representing the clothed arm. The fabric covered cylinder has a radius r and height H . The air layer trapped between the concentric fabric and skin cylinders is of thickness Y and it separates the inner solid cylinder maintained at the skin temperature T_{skin} and the outer porous cylinder represented by an isotropic fabric layer of permeability α and thickness e_f .

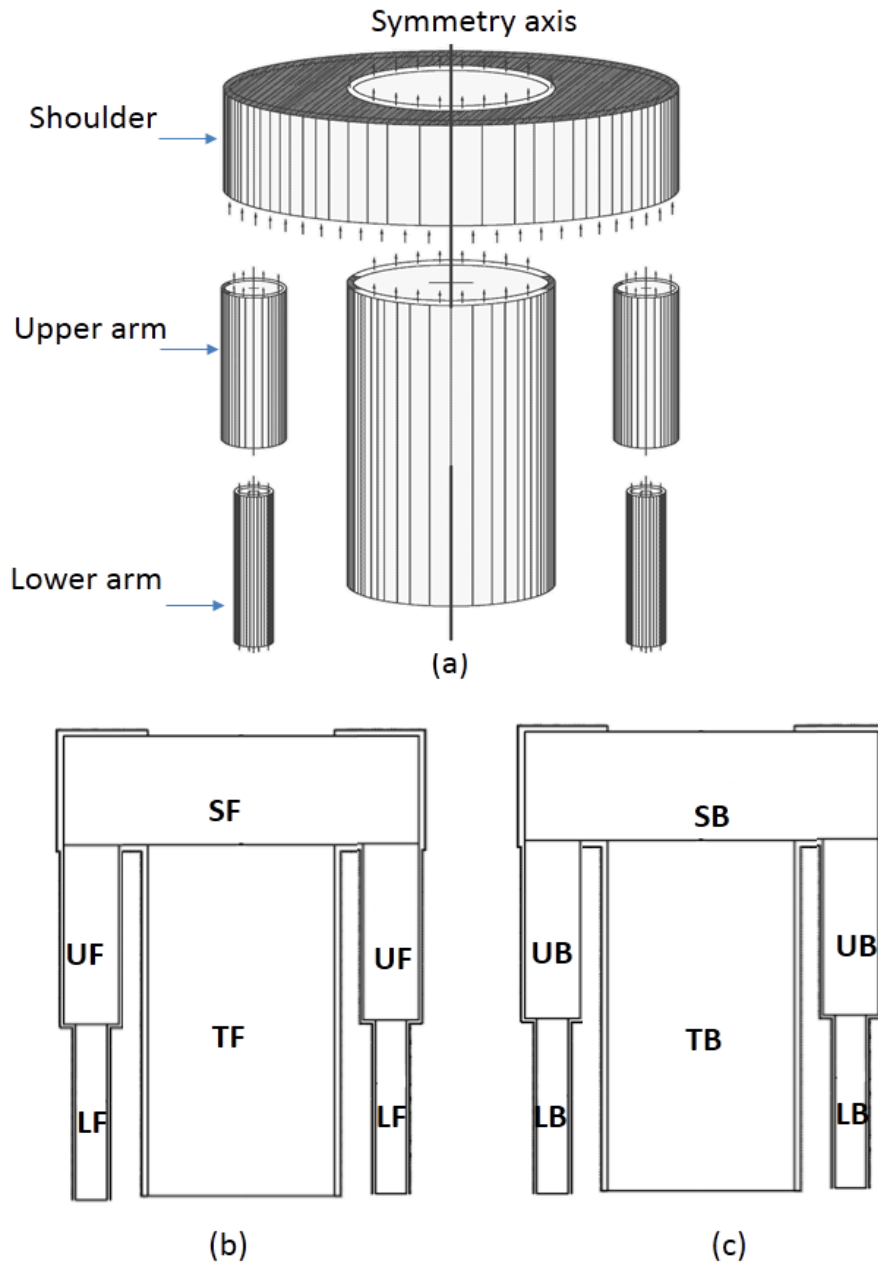


Figure 18: The physical configuration of the upper human body part showing (a) 3 D representation blowing up the segments (b) front view and (c) back view

The inter-connection between the segments requires revising the segmental electric circuit of Figure 17. If we take the example of the lower arm zone (LA), the inter-connection between the lower arm and the upper arm leads to a modification in the electric circuit shown in Figure 1 by adding a supplementary axial flow rate that passes from the lower arm to the upper microclimates in the front and back sides ($LF-UF$, $LB-UB$) or vice versa. By adopting the same methodology, the flow rate between the lower and upper arm is represented by a resistance-inductance circuit. The upper arms and the trunk are connected to the shoulder

zone on both front and back sides exchanging some air flow rate ($UF-SF$, $UB-SB$, $TF-SF$, and $TB-SB$). These exchanges are represented by a resistance-inductance circuit between the upper arm and the shoulder pressures and by a resistance circuit between the trunk and the shoulder since the trunk is not experiencing any oscillation. At the shoulder level (SF , SB), the inter-segmental ventilation (m^3/s) is estimated by the angular flow rate between the front and the back sides as given by the following equation:

$$Q_{inter-seg} = \frac{P_{SF} - P_{SB}}{R_{\theta 1}} \quad (42)$$

where $R_{\theta 1}$ represents the resistance to the air flow from the front to the back at the shoulder level. The following equation implies that if $Q_{inter-seg}$ is positive, this means that the air passes from the chest to the arm and vice versa. The top end of the shoulder front and back (SF/SB) are partially opened at the neck level while they are closed otherwise. This means that the air inside the microclimate layers of SF and SB zones is subjected to a discharge coefficient because of the 90° bending when leaving from the shoulder human body segment (SF and SB) to the environment.

Therefore, the electric circuit representing the walking human body is composed of the electric circuits characterizing each clothed segment connected between each other. This electric circuit is shown in **Figure 19**. All the resistances and inductances representing the ventilation used are presented in **Table 3**.

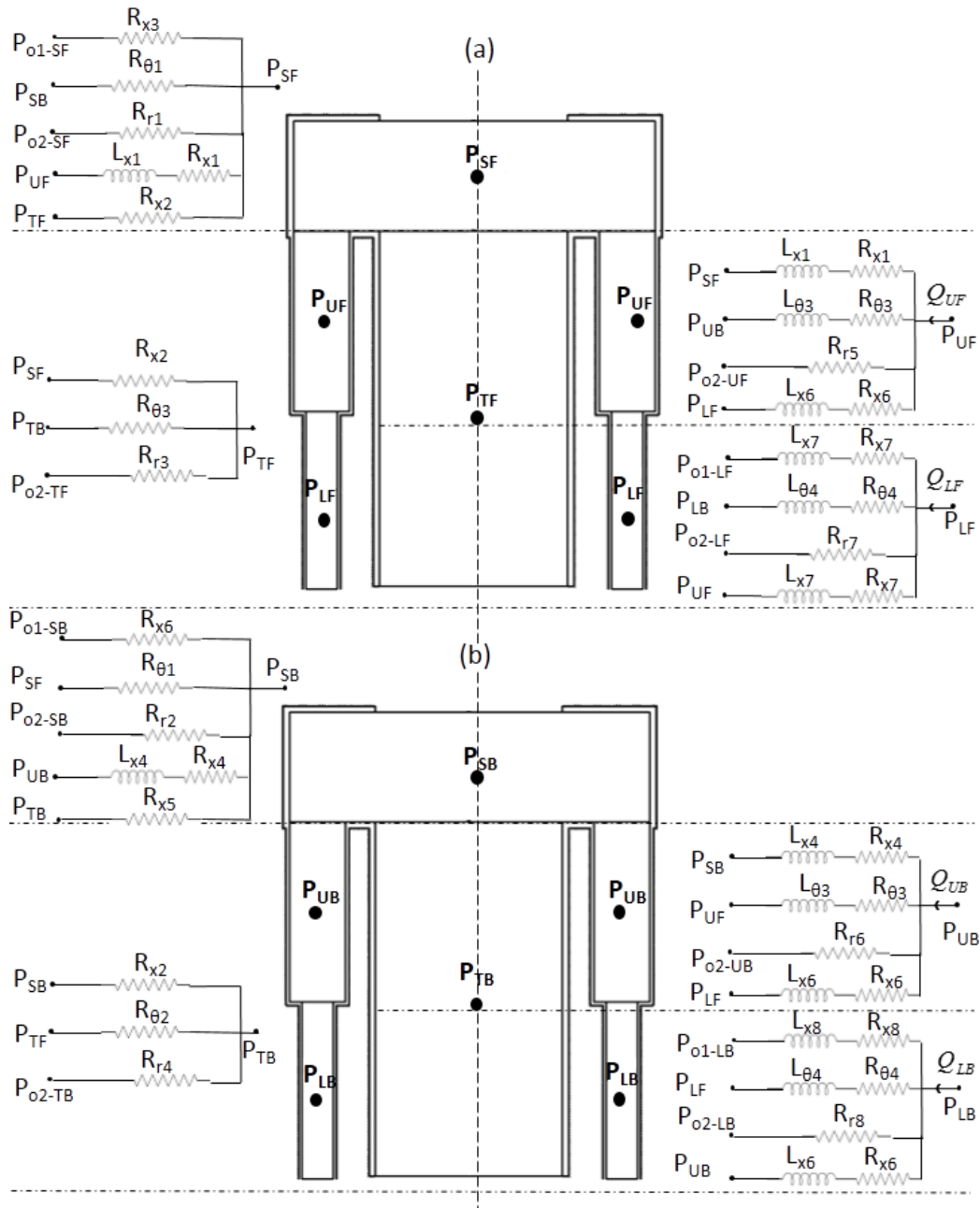


Figure 19: Network representing the analogy of the air flow inside the microclimate air layer of clothed upper human body for (a) the front side and (b) the back side

Table 3: Definition of the resistances and inductances in each direction

Direction	Resistance	Definition	Inductance	Definition
Axial	R_{x1}	$\frac{12\mu H_{UA}}{\bar{Y}_{UA}^3 (\pi r_{UA})}$	L_{x1}	$\frac{\rho H_{UA}}{\bar{Y}_{UA} (\pi r_{UA})}$

Direction	Resistance	Definition	Inductance	Definition
	R_{x2}	$\frac{12\mu H_{TF}}{\bar{Y}_{TF}^3 (\pi_{TF})}$	L_{x4}	$\frac{\rho H_{UB}}{\bar{Y}_{UB} (\pi_{UB})}$
	R_{x3}	$\frac{12\mu H_{SF}}{\bar{Y}_{SF}^3 (\pi_{SF})}$	L_{x6}	$\frac{\rho H_{SB}}{\bar{Y}_{SB} (\pi_{SB})}$
	R_{x4}	$\frac{12\mu H_{UB}}{\bar{Y}_{UB}^3 (\pi_{UB})}$	L_{x7}	$\frac{\rho H_{LF}}{\bar{Y}_{LF} (\pi_{LF})}$
	R_{x5}	$\frac{12\mu H_{TB}}{\bar{Y}_{TB}^3 (\pi_{TB})}$	L_{x8}	$\frac{\rho H_{LB}}{\bar{Y}_{LB} (\pi_{LB})}$
	R_{x6}	$\frac{12\mu H_{SB}}{\bar{Y}_{SB}^3 (\pi_{SB})}$		
	R_{x7}	$\frac{12\mu H_{LF}}{\bar{Y}_{LF}^3 (\pi_{LF})}$		
	R_{x8}	$\frac{12\mu H_{LB}}{\bar{Y}_{LB}^3 (\pi_{LB})}$		
	Angular	$R_{\theta1}$	$\frac{12\mu (\pi_{SF})}{\bar{Y}_{SF}^3 H_{SF}}$	$L_{\theta3}$
$R_{\theta2}$		$\frac{12\mu (\pi_{TF})}{\bar{Y}_{TF}^3 H_{TF}}$	$L_{\theta4}$	$\frac{\rho (\pi_{LF})}{\bar{Y}_{LF} H_{LF}}$
$R_{\theta3}$		$\frac{12\mu (\pi_{UF})}{\bar{Y}_{UF}^3 H_{UF}}$		
$R_{\theta4}$		$\frac{12\mu (\pi_{LF})}{\bar{Y}_{LF}^3 H_{LF}}$		
Radial	R_{r1}	$\frac{\Delta P_m}{\alpha \pi_{SF} H_{SF}}$	R_{r5}	$\frac{\Delta P_m}{\alpha \pi_{UF} H_{UF}}$
	R_{r2}	$\frac{\Delta P_m}{\alpha \pi_{SB} H_{SB}}$	R_{r6}	$\frac{\Delta P_m}{\alpha \pi_{UB} H_{UB}}$
	R_{r3}	$\frac{\Delta P_m}{\alpha \pi_{TF} H_{TF}}$	R_{r7}	$\frac{\Delta P_m}{\alpha \pi_{LF} H_{LF}}$
	R_{r4}	$\frac{\Delta P_m}{\alpha \pi_{TB} H_{TB}}$	R_{r8}	$\frac{\Delta P_m}{\alpha \pi_{LB} H_{LB}}$

i. Electric circuit analogy of the heat model from the upper human body part

In order to predict the heat and moisture transfer from the human body, Lotens [137] developed a steady-state heat resistance network model that describes all the mechanisms of heat and moisture transfer from the skin of the clothed segment to the environment. The heat network includes the radiative heat exchange, the convective resistances due to the air motion inside the microclimate air layer and outside in the environment, the dynamic resistance which includes the dry resistance of the clothing corrected for radial ventilation of renewal air [137]. The open aperture of the clothed segment induces a presence of additional heat exchange path between environment and microclimate air due to ventilation through opening. This heat resistance network has then been used in different studies to find the heat losses at different conditions. Ismail et al. [131] coupled the Loten's model to the electric circuit analogy of the ventilation model in order to find the heat losses from the independent clothed segment subjected to windy condition and experiencing walking mechanism. However, the coupling assumes an independent clothed segment concept and ignores the heat losses due to the flow rate from the clothed body segments. In this section, we will take the example of the clothed trunk and extend it to all other segments. The trunk segment consists of two zones as shown in Figure 18: the front zone (TF) and the back zone (TB). The air flowing from TF to TB and vice versa leads to a convective heat transfer. Furthermore, air could pass from the trunk to the shoulder part (TF-SF and TB-SB). This flow of air could also create a convective heat transfer. **Figure 20 (a-b)** illustrates respectively the heat transfer mechanism from each clothed body segment and the heat network associated with the clothed trunk. It is shown that the temperature of the trunk in front and back sides (T_{TF} , T_{TB}) are connected to the temperature of the shoulder in front and back sides (T_{SF} , T_{SB}).

In the same manner, the thermal resistance of Figure 21 illustrates the heat transfer in the shoulder zone. In fact, the inter-connection between the clothed segment microclimates allows air to be exchanged. The flow of air between the segments permits the convective heat exchange. The inter-segmental thermal resistance is given by the following equation:

$$R'_{SF-SB} = \frac{1}{\rho \times Q_{inter-seg} \times cp} \quad (43)$$

where ρ and cp are respectively the density and the specific heat of air. The electric circuit analogy of the heat exchange inside the microclimate air layer connects all the segmental electric circuits representing the heat transfer mechanism. All other corresponding thermal resistances are summarized in **Table 4**.

Table 4: Thermal resistance equations corresponding to the thermal network that represents the heat transfer from the clothed trunk

Resistance	Definition	Equation	Similar resistance equation
R'_{TF1}	Convective to the environment through the opening of the front side of the trunk	$\frac{1}{a \cdot V_w^b \cdot (\pi r_{TF} H_{TF})} \times \frac{r_{TF}}{(r_{TF} + Y_{TF})}$ <p>where $a = 4.8 * (2 \cdot r_{TF})^{-0.33}$ and $b = 0.5$</p> <p>[138]</p>	R'_{TB1} R'_{SF1}, R'_{SB1} R'_{UF1}, R'_{UB1} R'_{LF1}, R'_{LB1}
R'_{TF2}	Fabric dry resistance corrected by the dynamic resistance for ventilation of the front side of the trunk	$\frac{1}{\left(\frac{1}{R_d} + \rho Q_{r,TF} \times cp_a\right)} \times \frac{r_{TF}}{(r_{TF} + Y_{TF})}$ <p>[139]</p>	R'_{TB2} R'_{SF2}, R'_{SB2} R'_{UF2}, R'_{UB2} R'_{LF2}, R'_{LB2}
R'_{TF3}	Convective resistance from the inner fabric to microclimate air of the front side of the trunk	$\frac{1}{h_{i-a}} \times \frac{r_{TF}}{(r_{TF} + Y_{TF})}$ where $h_{i-a} = 9.6$ <p>[139]</p>	R'_{TB3} R'_{SF3}, R'_{SB3} R'_{UF3}, R'_{UB3} R'_{LF3}, R'_{LB3}
R'_{TF4}	Radiative resistance to the skin of the front side of the trunk	$\frac{1}{h_r} \times \frac{r_{TF}}{(r_{TF} + Y_{TF})}$ where $h_r = 3.7$ <p>[138]</p>	R'_{TB4} R'_{SF4}, R'_{SB4} R'_{UF4}, R'_{UB4} R'_{LF4}, R'_{LB4}
R'_{TF5}	Convective resistance from the skin to microclimate air of the front side of the trunk	$\frac{1}{h_{s-a}} \times \frac{r_{TF}}{(r_{TF} + Y_{TF})}$ where $h_{s-a} = 10.5$ <p>[139]</p>	R'_{TB5} R'_{SF5}, R'_{SB5} R'_{UF5}, R'_{UB5} R'_{LF5}, R'_{LB5}

R'_{TF6}	Radiative resistance to the skin of the front side of the trunk	$\frac{1}{h_r} \times \frac{r_{TF}}{(r_{TF} + Y_{TF})}$ where $h_r = 3.7$ [138]	R'_{TB6} R'_{SF6}, R'_{SB6} R'_{UF6}, R'_{UB6} R'_{LF6}, R'_{LB6}
R'_{SF7}	Convective to the environment through the opening of the front side of the shoulder	$\frac{1}{(\rho Q_{x,SF} \times cp_a)} \times \frac{r_{SF}}{(r_{SF} + Y_{SF})}$	R'_{SB7} R'_{UF7}, R'_{UB7} R'_{LF7}, R'_{LB7}
R'_{TF-TB}	Convective resistance from the front to the back microclimate air of the trunk	$\frac{1}{\rho Q_{\theta,TF} \times cp_a}$	R'_{SF-SB} R'_{UF-UB} R'_{LF-LB}
R'_{TF-SF}	Convective resistance from the front to the shoulder front zone microclimate air	$\frac{1}{\rho Q_{x,TF} \times cp_a}$	R'_{TB-SB} R'_{UF-SF}, R'_{UB-SB} R'_{LF-UF}, R'_{LB-UB}

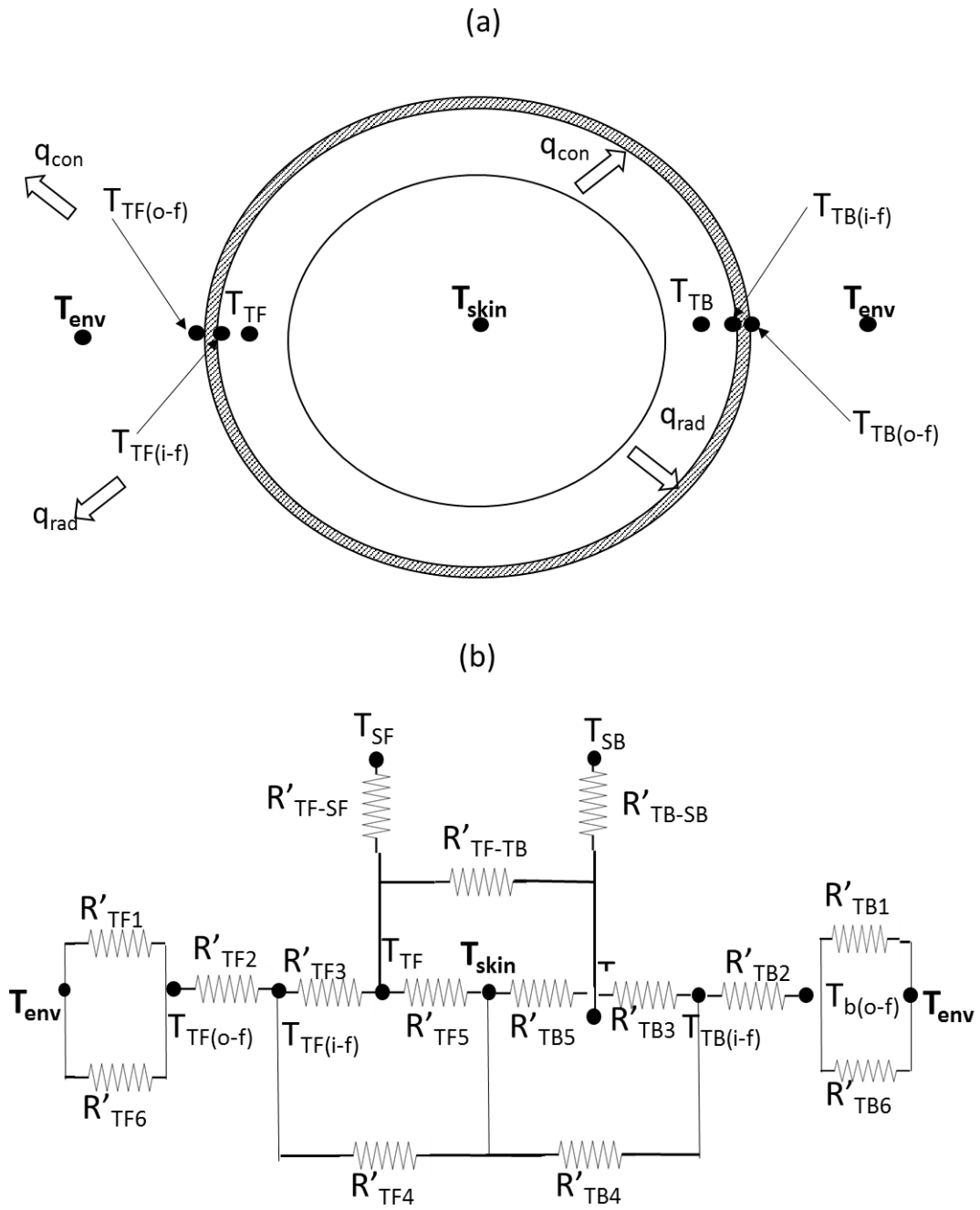


Figure 20: Schematic of (a) different mechanisms of heat transfer from the independent segment representing the trunk (b) thermal resistance network

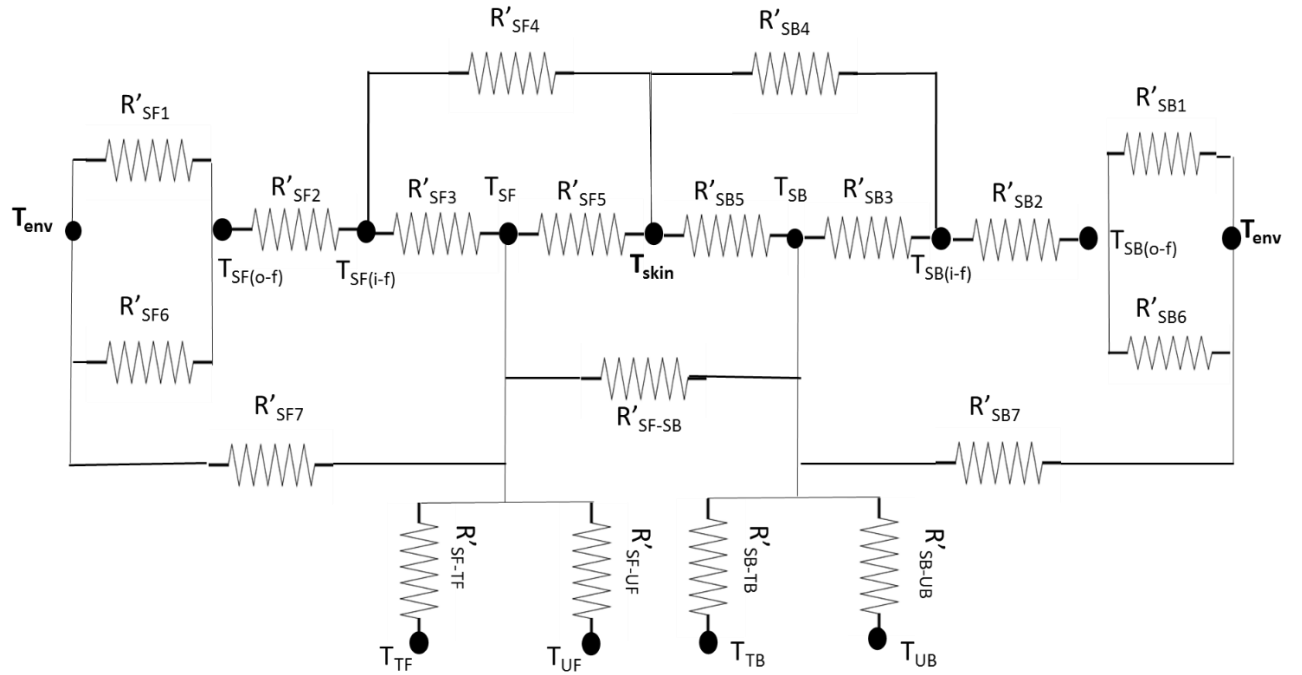


Figure 21: Schematic of thermal resistance network of the shoulder zone

c. Electric circuit analogy to predict the segmental ventilation of independent clothed segment by taking into account the natural convection

The aim of this section is to extend the simplified circuit model of ventilation in order to account for the buoyancy effect for a clothed arm segment with open aperture to the environment. The ventilation circuit model is coupled with a thermal resistance network in order to find the temperature difference between skin and the microclimate air layer that generates the buoyancy effect. The ventilation estimation will be considering a walking human with clothed arms that swing during walking and using actual reported data of human gait [123]. The coupled ventilation-heat circuit model will be the first in literature representing the complex heat exchanges of walking clothed human at low computational cost using common circuit and fast solvers.

This is accomplished by taking the example of the clothed arm in the front side and formulating the momentum equation in the axial direction where natural convection takes place. The back side will have similar derivation. The air gap size is assumed to vary in sinusoidal manner with time due to arm swings during walking.

The 1-D momentum equation for microclimate air flow in axial direction using the Boussinesq approximation is given by

$$\rho \frac{\partial v}{\partial t} = -\frac{\partial P}{\partial x} + \mu \frac{\partial^2 v}{\partial^2 y} - \rho g \beta (T_{front} - T_{env})$$

(44)

where ρ , μ and β are the density, the viscosity and the thermal expansion of air respectively, t is the time, v is the velocity.

By integrating the momentum equation over the corresponding cross-sectional area and replacing the velocity by the Wormesley parabolic profile in the y -direction, the equation becomes:

$$\Delta P_x = \frac{12\mu H}{\bar{Y}^3(\pi r)} Q_x + \frac{\rho H}{\bar{Y}(\pi r)} \frac{dQ_x}{dt} - \rho g \beta (T_{front} - T_{env}) H$$

(45)

The last term of Eq. (45) is the natural convection force per unit area related to the temperature difference between the microclimate and the ambient air. An electric circuit composed of a resistance and inductance placed in series with a voltage source of zero internal resistance is shown in Figure 22. The characteristic equation of this electric circuit is given by

$$\Delta V = Ri + L \frac{di}{dt} - e$$

(46)

By comparing Eq. (45) and Eq. (46), it is clear that there is a similarity between the air flows inside an oscillating arm in presence of natural convection subject to wind and the electric circuit shown in Figure 22. The analogy is based on the fact that when air is flowing inside the microclimate air layer, it is resisted by the viscous effect represented by an axial resistance as follows:

$$R_x = \frac{12\mu H}{\bar{Y}^3(\pi r)}$$

(47a)

On the other hand, the change in the flow of air due to the oscillating motion is represented by the inductance and is given by

$$L_x = \frac{\rho H}{\bar{Y}(\pi r)}$$

(47b)

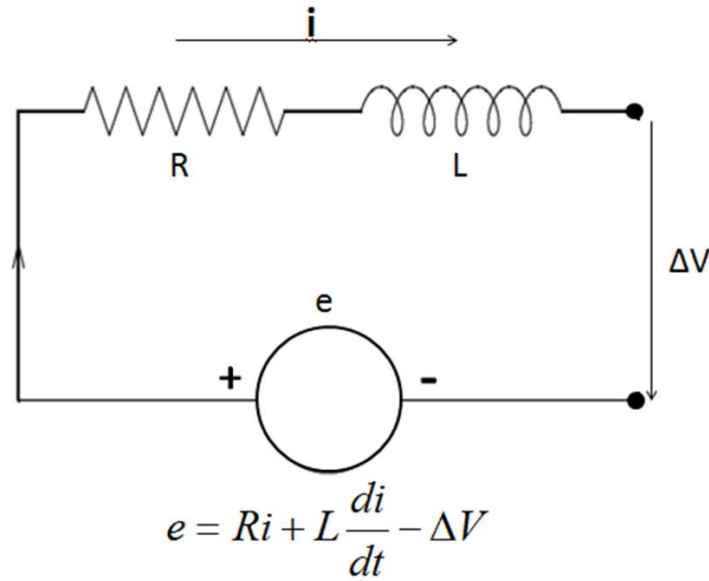


Figure 22: Electric circuit composed of inductance, resistance and source of voltage in series

Since the natural convection effect is induced by the warm human body condition, natural convection induced flow by virtue of the temperature difference is represented by the electromotive force (*e.m.f.*) and is given by

$$e = \rho g \beta (T_{front} - T_{env}) H \quad (48)$$

The above mathematical formulation establishes the electric circuit analogy in the axial direction where the natural convection phenomenon takes place. Concerning the other directions, the momentum equations are respectively the same as section 4.2.1. The electric circuit representing the oscillating clothed arm is given by Figure 23.

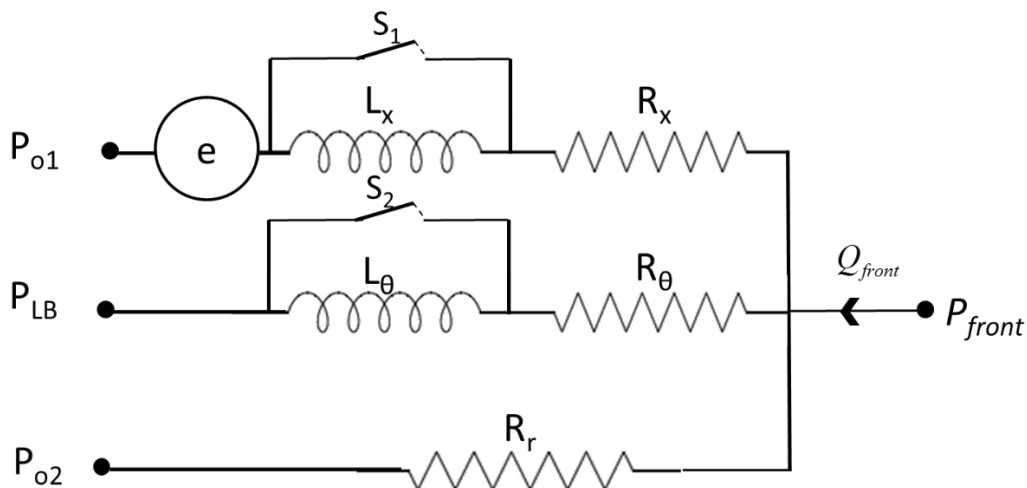


Figure 23: Network representing the analogy of the air flow inside the microclimate air layer of clothed arm subjected to external wind and oscillating motion taking into account the natural convection.

Incorporating the natural convection effect requires the knowledge of the temperature difference between the environment and the microclimate air layer (see Eq. (45)) which necessitates the coupling of the ventilation circuit model to the thermal resistance network shown in Figure 24.

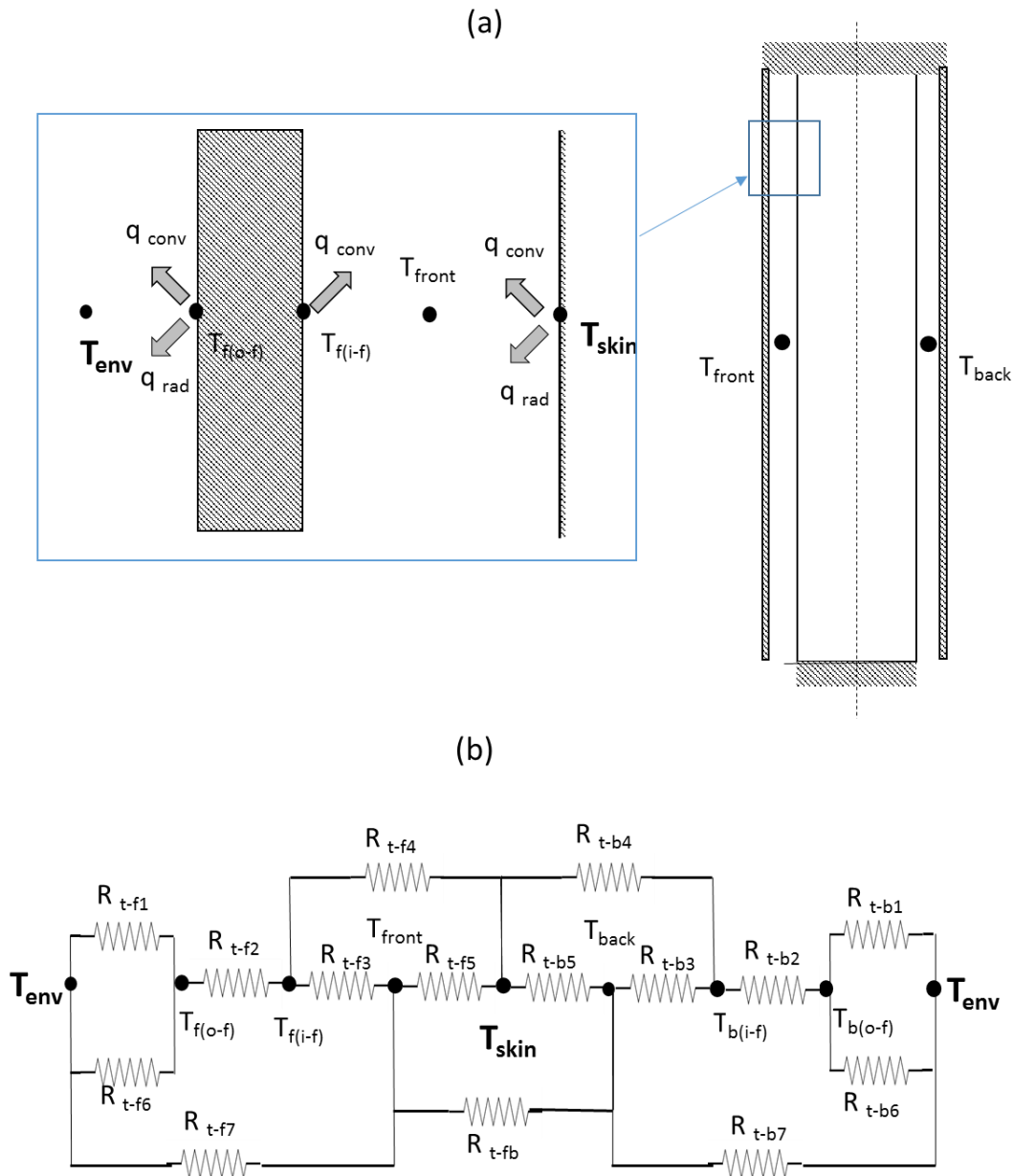


Figure 24: Schematic of (a) different mechanisms of heat transfer from the human body (b) thermal resistance network

The heat transfer consists of the radiative heat exchange, the convective resistances due to the air motion inside the microclimate air layer and outside in the environment, and the dynamic resistance that accounts for the clothing dry resistance and the ventilation rate. The radiative heat exchange q_{rad} occurs between (i) the skin and inner fabric and (ii) the

environment and the outer fabric. The heat transfer by convection q_{conv} is generally due to the air motion inside and outside the microclimate air layer. Since the swinging clothed arm is exposed to windy condition, convection heat transfer occurs at the outside cylinder at the front and back sides. The air flowing inside the microclimate air layer causes also a heat transfer between the inner fabric and the microclimate air layer at the front and back side respectively. On the other hand, the motion of air inside the microclimate air layer carries the heat from the inner cylinder surface representing the skin. Not only this, the presence of the opening at the end of the clothed arm creates a flow of air that releases the heat of the microclimate air layer. Similarly, the air flowing from the front to the back side creates a heat transfer between the front and the back sides. Finally, the temperature difference between the outer and inner nodes of fabric drives a heat transfer through clothing. The thermal heat resistances of these heat transfer modes are described in Table 5 with their corresponding equations.

Table 5: Thermal resistance equations corresponding to the thermal network that represents the heat transfer of the clothed oscillating arm

Resistance	Definition	Equation	Reference
$R_{t-f1}, R_{t=b1}$	Outer convective resistances to the environment for the front and back sides respectively	$\frac{1}{a.V_w^b.(\pi r_f H)} \times \frac{r}{r_f}$ <p>where $a = 4.8 * (2.r_f)^{-0.33}$ and $b = 0.5$</p>	[138]
R_{t-f2}	Fabric dry resistance corrected by the dynamic resistance for ventilation for the front side	$\frac{1}{\left(\frac{1}{R_d} + \rho Q_{r,front} \times cp_a\right)} \times \frac{r}{r_f}$	[139]
R_{t-b2}	Fabric dry resistance corrected by the dynamic resistance for ventilation for the back side	$\frac{1}{\left(\frac{1}{R_d} + \rho Q_{r,back} \times cp_a\right)} \times \frac{r}{r_f}$	[139]

R_{t-f3}, R_{t-b3}	Convective resistances from the inner fabric to microclimate air for the front and back sides respectively	$\frac{1}{h_{i-a}} \times \frac{r}{r_f}$ where $h_{i-a} = 9.6$	[140]
R_{t-f4}, R_{t-b4}	Radiative resistances to the skin for the front and back sides respectively	$\frac{1}{h_r} \times \frac{r}{r_f}$ where $h_r = 3.7$	[138]
R_{t-f5}, R_{t-b5}	Convective resistances from the skin to microclimate air for the front and back sides respectively	$\frac{1}{h_{mixed}} \times \frac{r}{r_f}$ where $h^3_{mixed} = h^3_{forced} + h^3_{natural}$ $h_{forced} = 10.5$ and $h_{natural} = 1.007 \Delta T^{0.406}$	[139] [142] [143]
R_{t-f6}, R_{t-b6}	Radiative resistances to the environment for the front and back sides respectively	$\frac{1}{h_r} \times \frac{r}{r_f}$ where $h_r = 3.7$	[138]
R_{t-f7}	Convective to the environment through the opening of the front side	$\frac{1}{(\rho Q_{x,front} \times cp_a)} \times \frac{r}{r_f}$	
R_{t-b7}	Convective to the environment through the opening of the back side	$\frac{1}{(\rho Q_{x,back} \times cp_a)} \times \frac{r}{r_f}$	
R_{t-fb}	Convective resistance from the front to the back microclimate air	$\frac{1}{\rho Q_\theta \times cp_a}$	

The developed coupled ventilation-heat circuit model is based on the coupling of the electric circuits representing the ventilation and the heat exchange models. The input parameters that were used in the coupled ventilation and heat model are the clothing properties, the geometric characteristics, the ambient conditions and the skin temperature as well as the walking speed, the frequency and the oscillation angle. First, an initial guess of the microclimate air layer temperature was made, and then the ventilation model was run. For each clothed segment, the pressure equations were solved in the front and the back side. The outputs of the ventilation model were the pressures, the mass flow rates in all directions, and the radial ventilation rate through clothing estimated as the positive flow of air into the air annulus integrated per unit area of the clothed surface. Afterwards, the segmental ventilation was used to adjust for the dynamic resistance on the thermal resistance network. The thermal model was solved in order to estimate the temperatures at different nodes. Once the temperatures were found, the microclimate air layer temperature estimated from the thermal resistance network is corrected in the ventilation circuit model. The procedure was repeated until convergence was achieved when both coupled pressure and temperature equations converge such that overall mass and energy were conserved in each grid and the values of pressure and temperature at the front and back side converge to a minimum relative error of 10^{-5} . The main outputs of the model are the segmental ventilation and heat losses from the skin to the environment.

3. Experimental methodology

The aim of this experiment is to measure the segmental ventilation as well as the heat losses from the human body at different wind and walking conditions in order to validate the integrated ventilation and heat model.

The experiments were conducted using 20-zone “Newton” thermal manikin [140] (Measurement Technology Northwest, Seattle Washington, USA) equipped with a walking mechanism. The surface temperature or heating power of each body segment of the manikin could be measured and controlled individually. Wire sensors are embedded on the thermal zones to afford the requested skin temperature with a standard deviation less than 0.01 °C. The heat flux generated to provide the skin temperature were recorded during experiments at each body part by ThermDAC® software. The manikin was dressed with a long sleeved cotton shirt and trousers. The properties of the shirt and pants were measured experimentally: (i) the air permeability of the shirt and pants were tested by SDL MO2IA

air permeability device with a standard deviation in repeated measurements of $\pm 10^{-4}$ and accuracy of $0.1 \text{ l}/(\text{m}^2 \cdot \text{s})$ (ii) the dry resistance is measured using the sweating guarded hotplate (Model 306-200/400) with an error less than 0.1%. These properties are given in **Table 6**.

Table 6: Fabric properties of the thermal manikin ensemble

	Material	Air permeability (m/s)	Dry resistance (K·m ² /W)
Shirt	100 % cotton	1.38	0.046
Pants	75 % cotton, 25% polyester	0.25	0.041

Two large fans with a diameter of 0.5 m were installed vertically on a stand with controllable wheels to adjust the distance between the manikin and the fans stand for the desired velocity at the front side of the manikin. An additional single fan is used whenever we want a trunk relative velocity that is different than the clothed arm. In fact, when considering the walking condition, the trunk is moving in the real case scenario; however, the thermal manikin trunk stays at the same place while the clothed arm is oscillating. In order to solve this issue, the trunk is faced with an additional fan that adjusts the relative velocity. The wind speed was measured by the manikin wind speed sensor which is an air velocity transducer (model 8475-06) at 3-min intervals at different locations and a mean value of wind speed is reported for each test scenario. The manikin and the fans were placed in a controlled environmental chamber. The chamber air temperature was measured by two manikin sensors at different heights (0.9 m and 1.6 m) and the average was about $25 \text{ }^\circ\text{C} \pm 0.2 \text{ }^\circ\text{C}$. The relative humidity was measured at 1.6 m height and it was about $40 \pm 3 \%$.

The experiment is conducted on a thermal manikin using a constant temperature mode by applying the tracer gas technique at different wind and walking conditions. In the case of independent clothed segment, tracer gas injection experiment is conducted for each experiment. Second, if inter-connected experiment is considered, three experiments were conducted with three scenarios of tracer gas injection into (i) both the clothed trunk and the arm simultaneously; (ii) for the clothed arm only; and (iii) for the clothed trunk only.

The tracer gas method is applied only at the upper clothed part using Argon as tracer gas since it is non-explosive, non-toxic, and completely inert (no contamination of the tested product). Furthermore, Argon is extremely rare in the atmosphere and will not contaminate and desensitize its own detector. **Figure 25** shows the schematic diagram of our experimental setup that estimates the ventilation based on the tracer gas methods of Ke et al. [141] for local clothing ventilation measurement. An argon analyzer of 0.2 % accuracy and a resolution of 0.01 % were mounted in line at the outlet flow from the manikin microclimate air layer. A diaphragm pump (2-5 l/min) was installed to circulate the extracted air from the manikin. The flow of air was controlled and measured by an air flow controller (0-5 l/min). Another flow controller (0-1.5 l/min) was mounted at the top of the Argon tank. The distribution and the sampling flow were provided using tubes sealed to the right arm (or left) and the half of the trunk perforated with holes of 1 mm diameter. The inlet flow and outlet flow were controlled to 5 l/min while the added Argon flows were 3 l/min. Taking advantage of symmetry, the distribution flow and the sampling flow were provided using tubes sealed to the right arm (or left), and half of the chest of the thermal manikin and perforated with holes of 1 mm diameter. The thermal manikin was turned on at constant segmental skin temperature of 34 °C. Once the heat fluxes generated during experiments from each segments stabilized, the Argon tank was opened, and the flow controller mounted at the top of the tank was calibrated to the desired Argon flow. The diaphragm pump was switched on to extract air at a flow rate specified by the air flow controller. The mixed air and Argon were injected and extracted at the microclimate conditions from the arm and the trunk. The experiment was repeated until the steady state/ steady periodic conditions of the recorded inlet and outlet concentrations and the heat losses of the thermal manikin were reached and recorded. The steady state/ steady periodic was reached after 80-100 minutes. **Figure 26** shows the experimental set up with the walking thermal manikin and the argon tank.

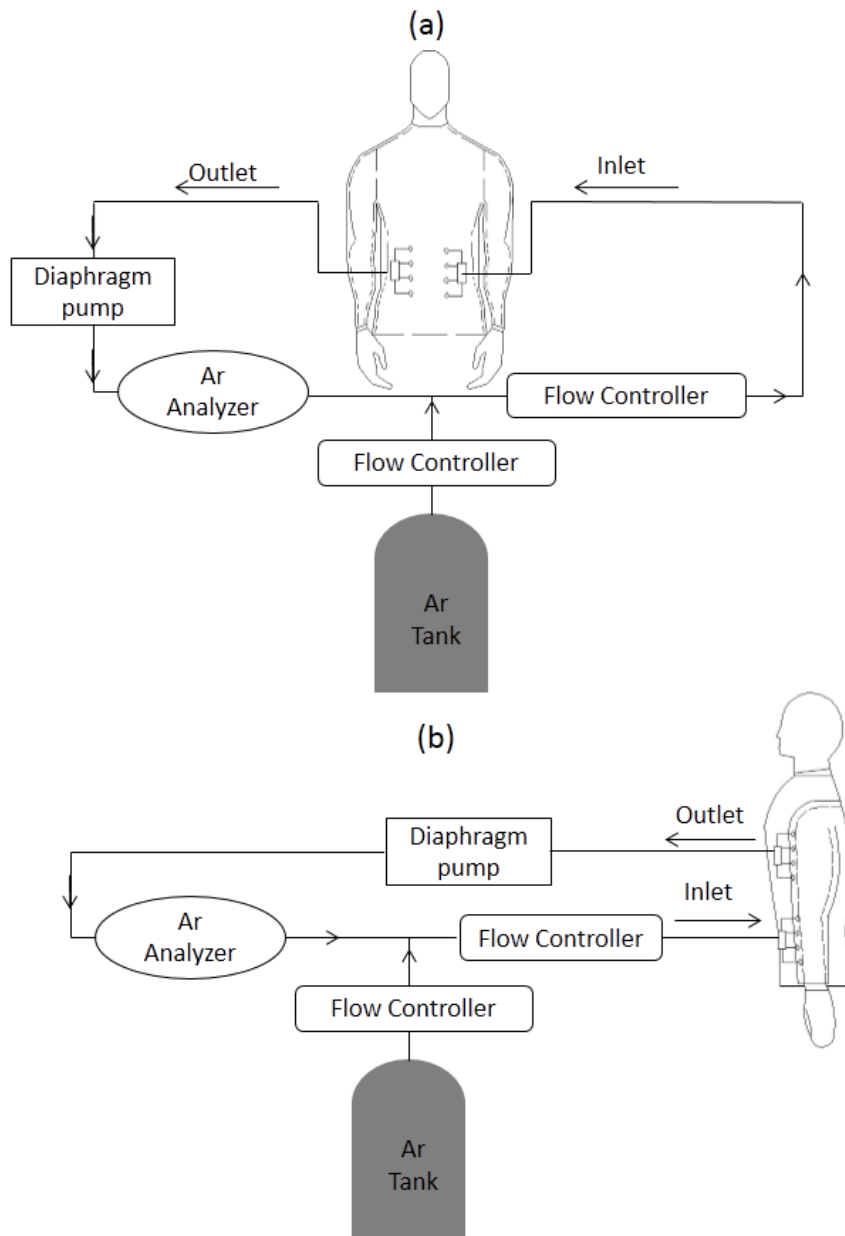


Figure 25: Schematic of the experimental set up to measure the ventilation of the front side for (a) the clothed trunk and (b) the clothed arm

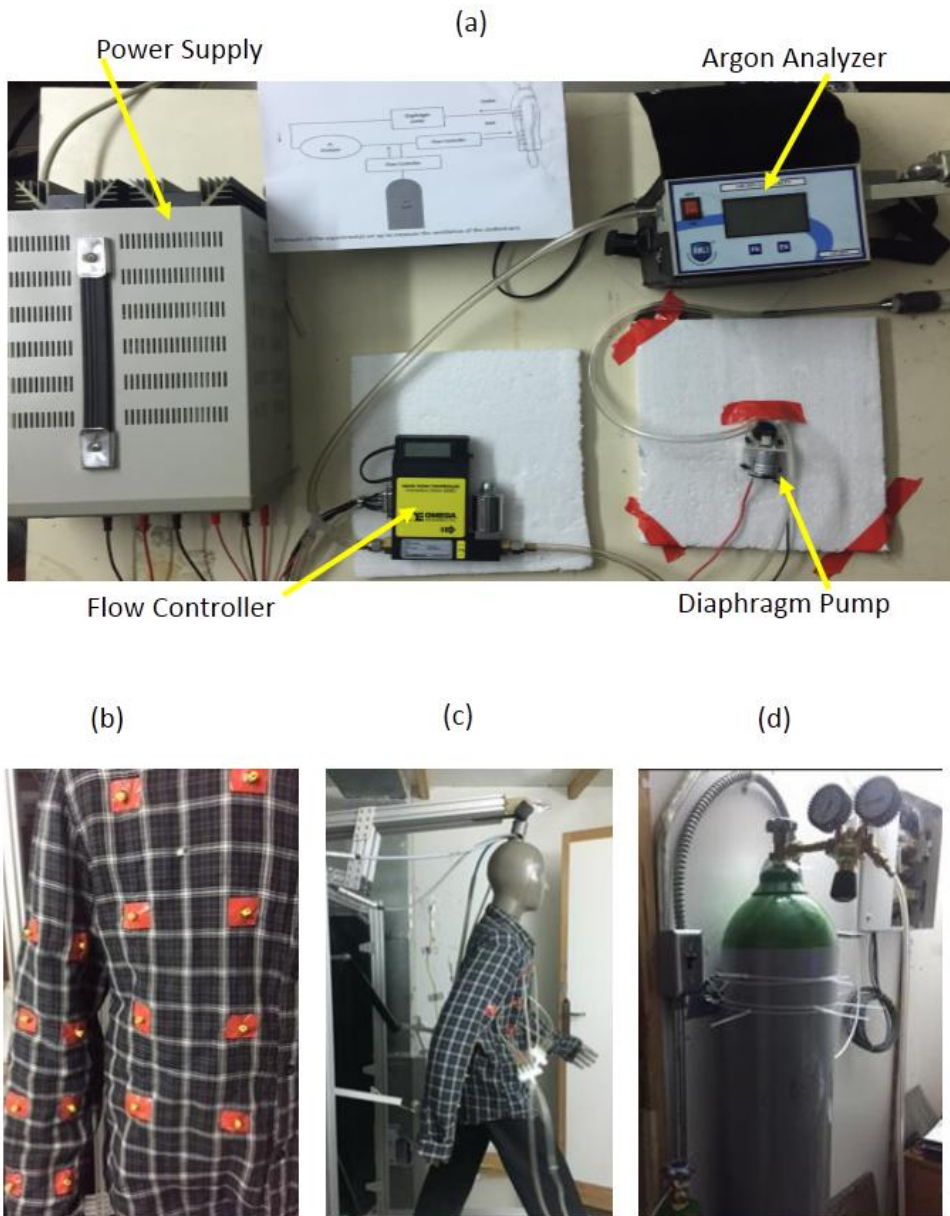


Figure 26: Figures showing (a) the experimental set up (b) the manikin shirt (c) the walking thermal manikin and (d) the argon tank with its flow controller

CHAPTER III

RESULTS AND DISCUSSIONS

A. Prediction of the fiber diameter

The model is simulated for the three sets of experiments summarized in Table 7 and the final fiber diameter is calculated. To insure the validity of the model predictions, the calculated and the experimental fiber diameter are calculated for the same conditions. The relative error between them is reported for each simulation.

Figure 27(a), 27(b), and 27(c) show the theoretical and the experimental fiber diameter as a function of (a) the flow rate, (b) the electric field, and (c) the polymer concentration. The error bars shown in Figure 27 are related to the standard deviation given by the SEM machine. The average standard deviation is about ± 32 nm. There is a good agreement between the predicted and experimental values with an average relative error of 6.65 % of and a maximum relative error of 10%.

Table 7: Set of experiments performed.

	Flow rate ($\mu\text{l/hr}$)	Electric field (V/m)	Solution property	
			Concentration (%)	Conductivity (S)
Varying the flow rate	900	97222	10	0.00823204
	960	97222	10	0.00823204
	1020	97222	10	0.00823204
	1080	97222	10	0.00823204
	1140	97222	10	0.00823204
	1200	97222	10	0.00823204
	1260	97222	10	0.00823204
	1320	97222	10	0.00823204
Varying the electric field	900	88889	10	0.00823204
	900	91667	10	0.00823204
	900	94444	10	0.00823204
	900	97222	10	0.00823204
	900	100000	10	0.00823204
	900	102778	10	0.00823204

	900	105556	10	0.00823204
	900	108333	10	0.00823204
	900	111111	10	0.00823204
	900	113889	10	0.00823204
Varying the polymer concentration	900	97222	8	0.00726524
	900	97222	9	0.00778994
	900	97222	10	0.00823204
	900	97222	11	0.00859154

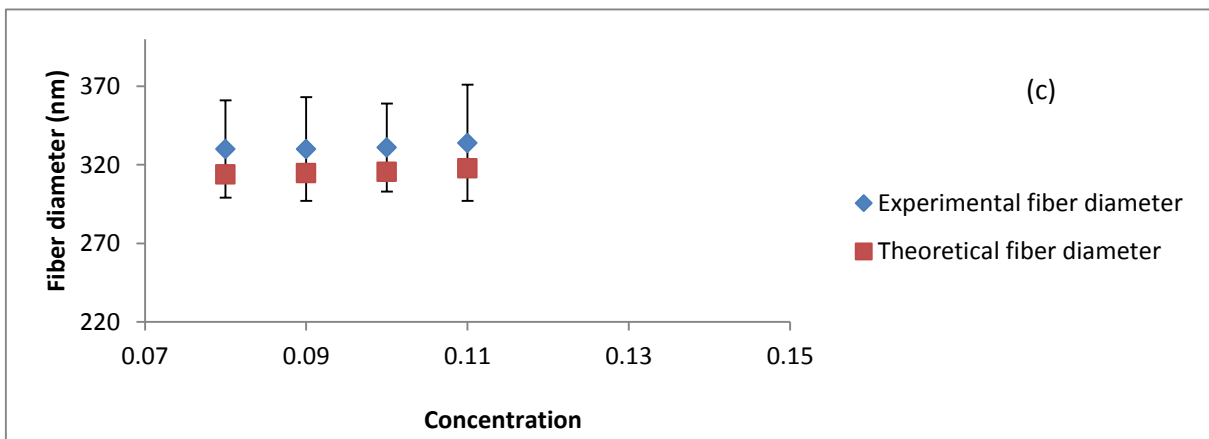
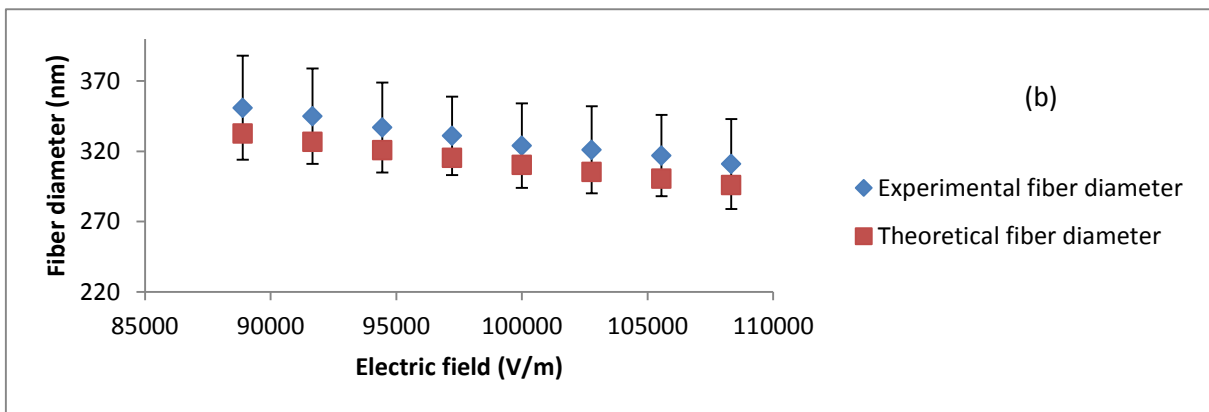
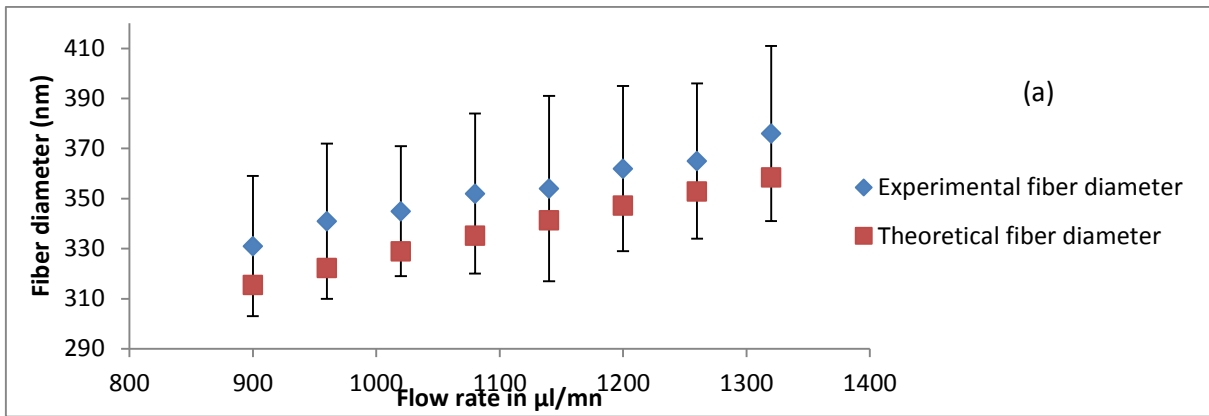


Figure 27: Comparison between theoretical and experimental fiber diameter for (a) different flow rates (b) different electric field (c) different concentrations

1. Effect of flow rate on the fiber diameter

Our model predictions agree with the experimental fiber diameter at different flow rates with a relative error of 6.5 %. The final fiber diameter increases with the increase of flow rates which is the case for most of polymeric solution (see Figure 27(a)). This is similar to trend

reported in literature where at lower flow rates, a small amount of solution is ejected from the nozzle. With increasing flow rate at the same electric field, a larger amount of solution volume is ejected. However, the electric field strength is not capable of stretching the ejected solution of larger volume. This limited stretching leads to an increase of fiber diameter at larger flow rate. Moreover, it is shown that the flow rate has a significant effect on the final diameter: an increase of 30% in flow rate leads to an increase of 15% in fiber diameter.

2. Effect of electric field on the fiber diameter

Figure 27(b) shows the variation of the fiber diameter with the electric field. The figure shows a good agreement between the model predictions and the experiment with an average relative error of 6.72 %. Moreover, it clearly illustrates that the increase of electric field yields to a decrease of the fiber diameter. Indeed, the increase in applied electric field yields to an increase in the drawing force (Coulombic force) which is responsible in stretching and thinning the fiber. Therefore, increasing the electric field contributes to a decrease in the final fiber diameter. For instance, an increase of 30% in electric field yields to a decrease of 14% in the final fiber diameter.

3. Effect of polymer concentration on the fiber diameter

Figure 27(c) shows the variation of the fiber diameter with the polymer concentration. The model predictions line with the experiment measurements of the final fiber diameter with an average error of 6.72 %. The effect of concentration on the fiber diameter is generally related to the viscous effect. As the polymer concentration increases, the viscosity increases. However, the viscous force stands against the stretching of the fiber. Consequently, the fiber diameter increases with increasing the viscosity. In other terms, an increase in concentration leads to an increase in the final fiber diameter. However, the effect of concentration is

negligible compared to the effects of flow rate and electric field. As shown in Figure 27(c), an increase of 30% in the concentration contributes to only 1% increase.

4. Model validation with published experimental study

Ozkok *et al.* [144] investigated the effect of solution concentration on the morphology of polyacrylonitrile (PAN) nanofibers by measuring the fiber diameter at different concentrations. In this section, we are interested on comparing our model results with Ozkok *et al.*[144] published experiment. Unlike other studies, Ozkok *et al.* [144] provided all the electrospinning parameters needed as input to validate our model. These parameters are: $r_0=0.7$ mm, $\Delta V=35$ kV, $Q=0.5$ ml/hr, $L=10$ cm. the fiber diameter varies from 216 nm at a polymer concentration of 6%, to 270 nm at a polymer concentration of 12 %. By using the same input, our model predicted the same trend with a maximum relative error of 15 %. The predicted fiber diameter varies from 189 nm to 230 nm at a polymer concentration of respectively 6 % to 12 %. Given that the standard deviation of SEM measurement is about ± 32 nm, the predicted fiber diameter using current model are within the range of the published experiment.

5. Model comparison against predictions of published models

Despite the fact that the stages of electrospinning were investigated in the literature by different mathematical models, however these models were mainly interested in studying the jet profile, the stability of the jet, and the physics behind the bending instabilities. Few models reported the final fiber diameter explicitly [30]. For instance, some models presented a scaling study of the final fiber diameter in electrospinning as function of the processing parameters and did not come up with the fiber diameter values [29]. Other models, like Zeng *et al.* [42] model and Stepanyan *et al.* model [43] that are based on the published physical models, reported the final fiber diameter at different processing parameters. However, they

did not report their model accuracy except in the work of Fridrich et al. [30] where an average relative error of 20 % for polyacrylonitrile solution was reported. However, they used an arbitrary range for the characteristic length χ without developing a systematic method for its calculation. While in the current work, the characteristic length χ is related to the first electrospinning stable jet stage which couples the stable and the unstable jet regions leading to better prediction of final fiber diameter.

6. Model limitations

The main limitation of this model was attributed to the correlation assumption used (equation 11) in the bending instability region which limit the model to relatively small polymer solvent concentration ($\leq 12\%$). Another limitation is related to the collecting speed. In our study, we choose an average collecting speed of 600 rpm. The choice of this collecting speed is basically related to the fact that a high collecting speed could affect the final fiber diameter which is the result of the force exerted on the depositing fibers by the take-up roll.

B. Prediction of the web morphology

PAN solutions at various concentrations were electrospun under the ambient conditions of 20°C and a relative humidity of about 30%. A set of experiments was performed where the flow rate was varied from 900 to 1320 $\mu\text{l/hr}$, the electric field was varied from 90 to 120 KV/m , the solution concentration was varied from 8 to 11 % and the time of electrospinning was varied from 10 to 360 min . The effect of each processing parameter on the morphology of the nano-fibrous web as well as the air filtration efficiency is studied by varying one parameter and holding all the other constants at the following values:

$Q = 900 \mu\text{l/hr}; E = 98 \text{KV/m}; C = 10\%, \text{ and } t_e = 10 \text{min}, u_0 = 5 \text{cm/s}, d_p = 300 \text{nm}.$

1. Effect of processing parameters on thickness and porosity

a. Electrospinning time

Figure 28 shows the variation of the nano-fibrous web porosity and thickness as a function of the electrospinning time as measured experimentally and predicted by the modeling approach. As shown in Figure 28, the electrospinning time affects both the thickness and the porosity of the nano-fibrous web. Good agreement is found between the theoretical and the experimental values with a relative error less than 8 %. The number of layers forming the nano-fibrous web increases by increasing the electrospinning time. As these layers are randomly deposited, the fibers of a layer may block the pores of the previous deposited layer. Thus, the porosity of the nanofiber decreases gradually by deposition time.

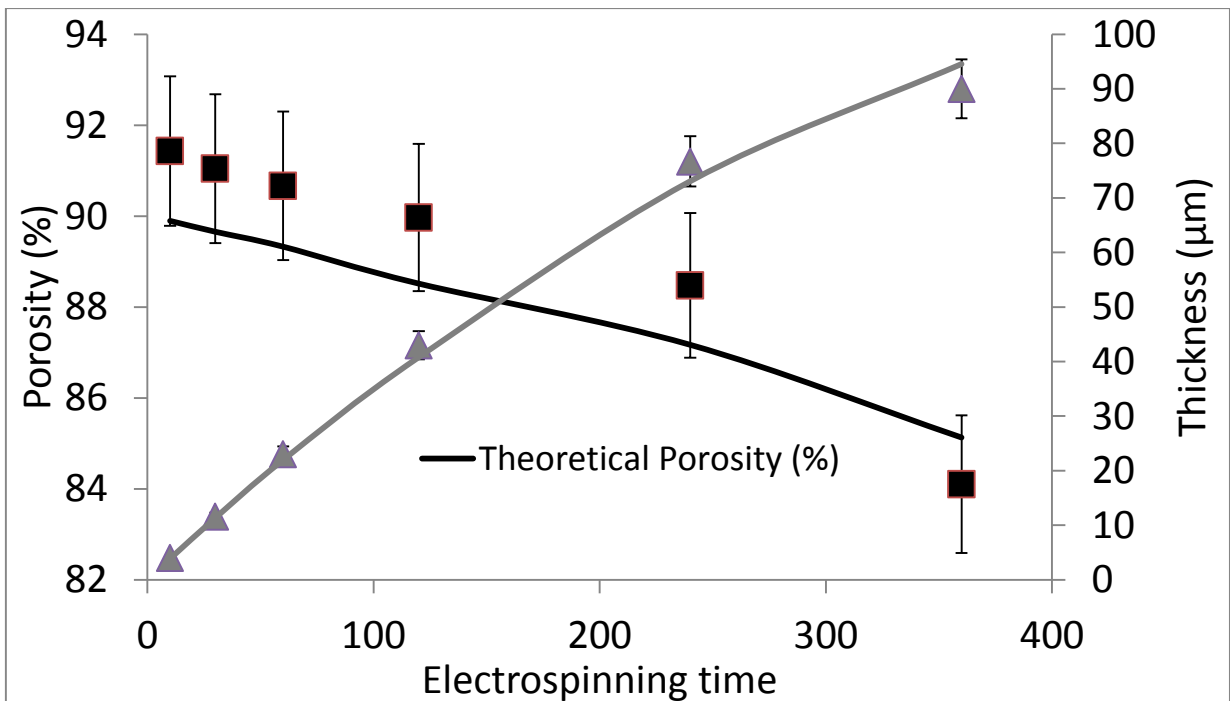


Figure 28: Experimental and theoretical effect of electrospinning time on the porosity and thickness of the nanofiber web

b. Processing parameters of electrospinning (Q, E, C)

Figure 29 shows the effect of processing parameters on the morphology of the nano-fibrous web as measured experimentally and predicted by the models. It shows the influence of varying (a) the volumetric flow rate, (b) the electric field, and (c) the polymer concentration of electrospinning, respectively, on both porosity and thickness. It is worth to note that good agreement is found between the theoretical and the experimental values with a relative error less than 8 %. As shown in our previous study, the final fiber diameter increases by

increasing the flow rate and the polymer concentration and decreases by increasing the electric field. Therefore, the effect of electrospinning parameters on the porosity and thickness of the nano-fibrous web is directly attributed to the effect of the final fiber diameter on them. Fig. 30 presents the effect of the electrospinning fiber diameter on the porosity and thickness determined by the developed model. It is clear that increasing the fiber diameter causes larger pore size as shown in the literature. On the first impression, one would expect that increasing the fiber diameter would lead intuitively to an increase of porosity. However, as shown in Fig. 30, the porosity is slightly changed (increased/ decreased) with the increase in the fiber diameter. The main reason is that the porosity is also affected by the change in the nano-fibrous web thickness. Indeed, porosity and thickness are inversely correlated: if the thickness increases, the porosity decreases and vice versa. As shown in Figure 30, the thickness is increasing with the fiber diameter. Thus, the porosity is dominated by two opposite phenomena as a consequence of the fiber diameter increase: increasing the pore size and increasing the thickness. The former leads to an increase in porosity while the latter does the opposite. This dual effect is the cause of the slight change of the porosity as a function of the final fiber diameter.

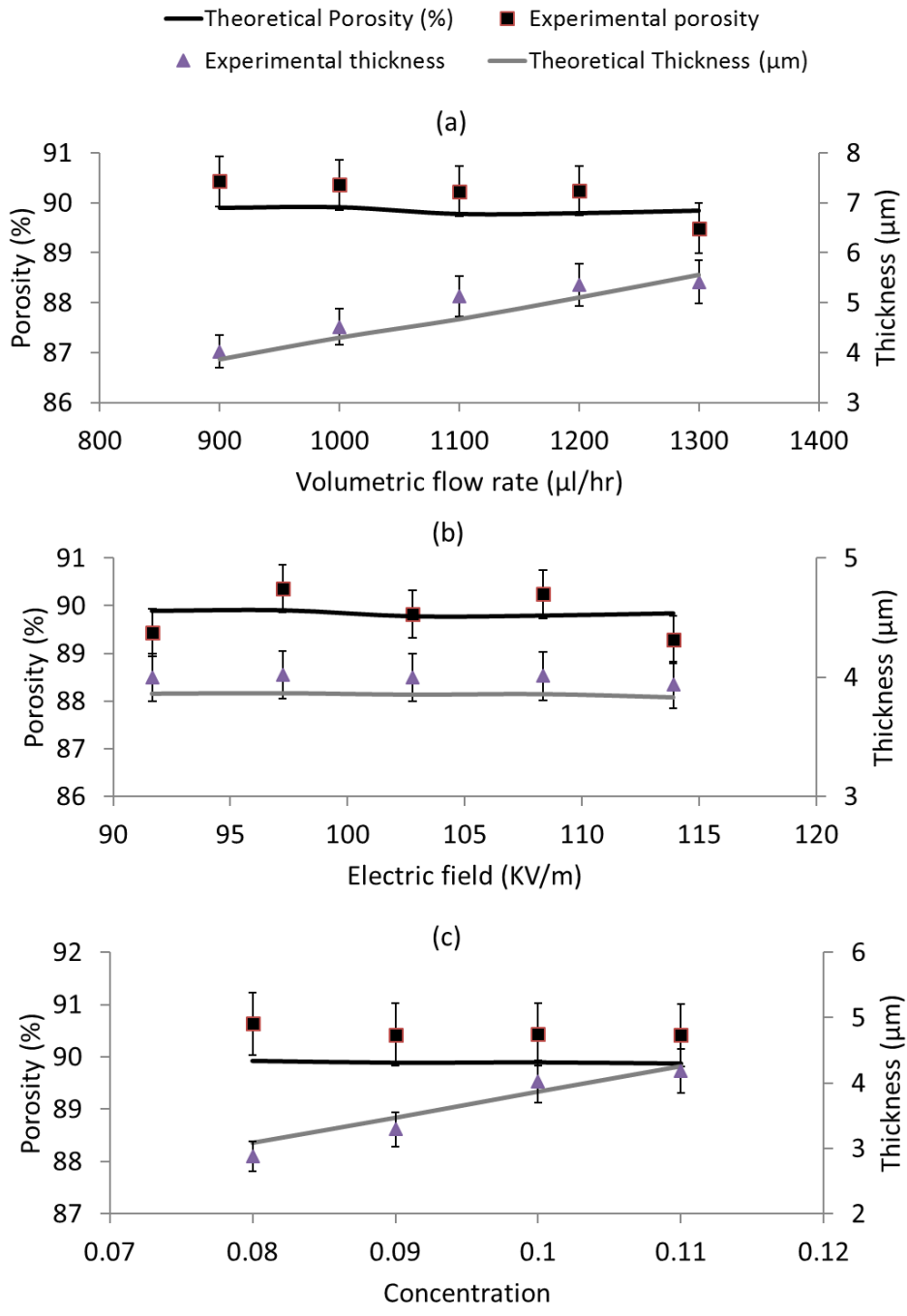


Figure 29: Effect of (a) flow rate (b) electric field (c) concentration on porosity and thickness at the nanofiber web

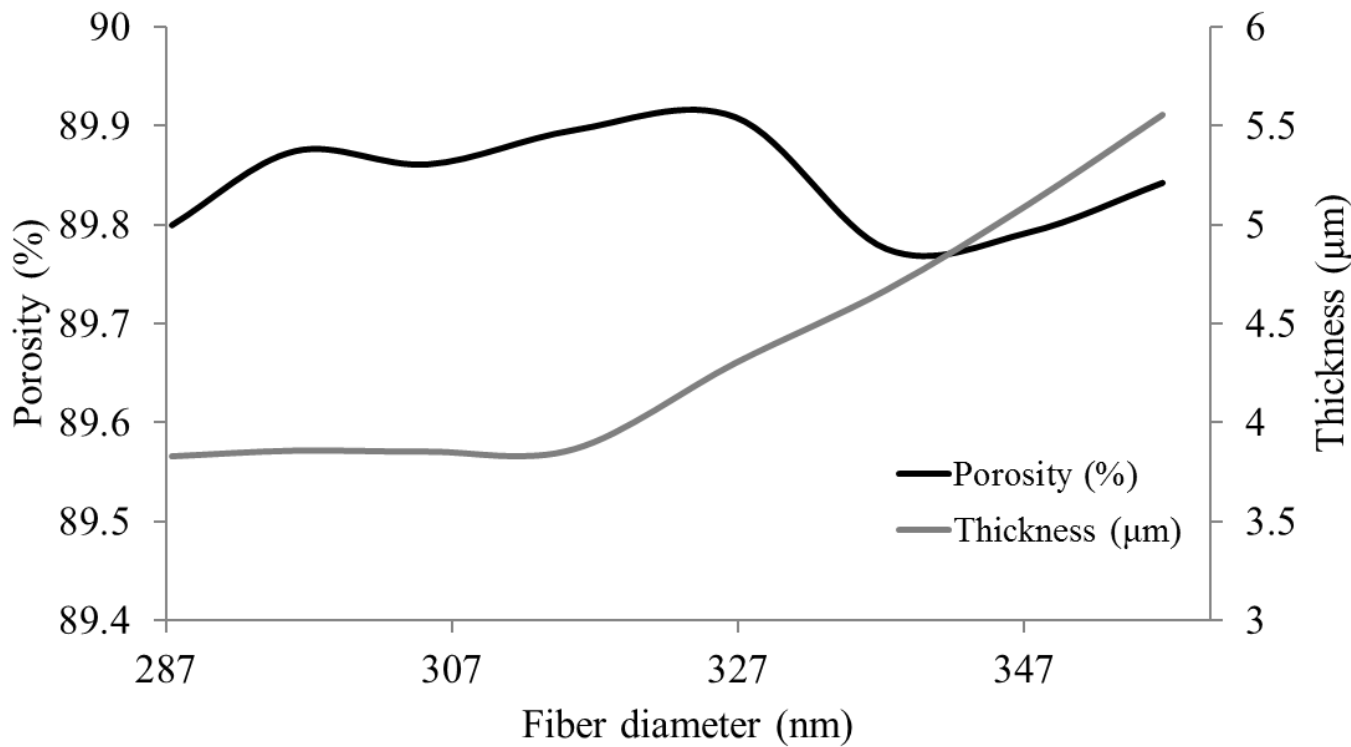


Figure 30: Effect of the fiber diameter on nanofiber web thickness and porosity

2. Effect of processing parameters on air permeability and aerosol filtration

a. Electrospinning time

Figure 31 illustrates the effect of the electrospinning time on the air permeability and the air filtration efficiency against aerosol particles for the following processing parameters ($Q = 900 \mu\text{l/hr}$, $E = 97222 \text{ V/m}$, and $C = 10\%$). The experimental results are in a good agreement with the theoretical findings (i.e., the maximum and the average relative error are respectively 10 % and 7 %). Figure 31(a) shows that the air permeability is decreasing significantly as the coating time increases. Only 20 min of electrospinning is able to decrease the air permeability from 120 to 40 cm/s. The air permeability is strongly related to the thickness and porosity of the nano-fibrous web. As the coating time increases, the thickness increases while the porosity decreases. This contributes to a large resistance to the air flow leading to a significant decrease of air permeability.

Fig. 31(b) shows the results obtained for the penetration of nanoparticles (size range of 300–1000 nm) through the nano-fibrous web deposited on the nylon screen mesh as a function of different electrospinning time at a velocity of 5 cm/s. The electrospinning time range is

limited in this figure to 60 *min* because both simulations and experiments prove that, after this time, the filtration efficiency reaches 100% (i.e. no particle passes through). The results show that the predictions of the model lie in the standard deviation of the experimental data. Moreover, the results show that the filtration of aerosol particles through nano-fibrous web followed the classical filtration model: the filtration efficiency decreases when reducing the particle size, due to Brownian diffusion. Therefore, in our study, the most penetrating particles were found to have a size of 300 nm. On the other hand, the filtration of aerosol particles increases with the time of electrospinning reaching an approximate total filtration (100%) after one hour of coating. This is of course due to the fact that increasing the thickness and decreasing the porosity by increasing the electrospinning time will form an efficient barrier to aerosol particles generation. The least efficient nano-fibrous web was the sample having the least coating time (10 *min*). Indeed, after only ten minutes of coating, the nano-fibrous web is able to filtrate more than 75 % of the most penetrating particles while having a significant air permeability of 120 *cm/s*. By tripling the coating time to 30 *min*, the nano-fibrous web filtration increases harshly to about 90% for the most penetrating particles. This finding clearly proves the potential of nano-fibrous web in the development of barrier materials against aerosol particles. Figure 31(b) shows that the aerosol filtration agrees with the experimental findings. The standard deviation of the measured values was within (2 %).

b. Processing parameters (Q, E, C)

It is of interest to study the effect of the electrospinning processing parameters (Q, E, t_e) on the air permeability and the filtration efficiency of the nano-fibrous web. The chosen nano-fibrous web corresponds to an electrospinning time of 10 *min*. The particle diameter studied in the filtration efficiency is the most penetrating particle found (300 *nm*) at a wind velocity of 5 *cm/s*. It is shown that when the flow rate increases (see Figure 32(a)), the air permeability decreases while the filtration efficiency increases. The same results are found when the electric field or the concentration increases (see Figure 32 (b-c)). Although the flow rate and the concentration variation have the opposite effect of the electric field on the fiber diameter of electrospinning, they all affect the air permeability and the filtration efficiency in the same way.

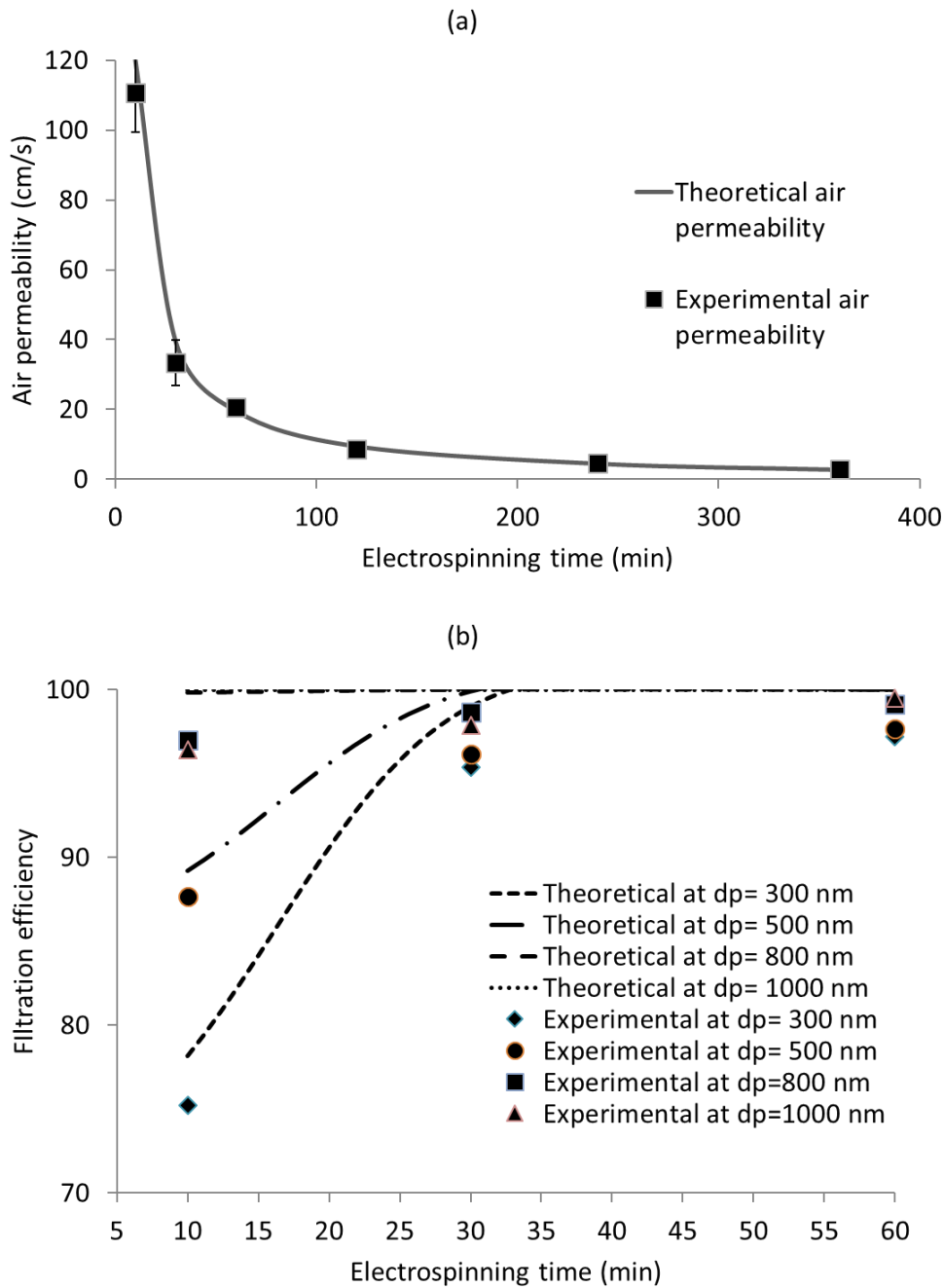


Figure 31: Effect of electrospinning time on (a) air permeability (b) aerosol filtration for different particle diameters

In order to understand the cause of such behavior, it is important to show the effect of fiber diameter on the air permeability and the filtration efficiency of the nano-fibrous web chosen (10 min of coating time) at the most penetrating aerosol particle (300 nm) and at a velocity of 5 cm/s. As Fig. 33 shows, the predicted air permeability and the filtration efficiency experience a maximum and a minimum respectively for the same fiber diameter 315 nm. In order to explain this behavior, it is worth to refer to Fig. 30. Fig. 30 shows that although the

fiber diameter is increasing to reach 315 nm, the porosity and thickness are unchanged. The increase of fiber diameter at constant porosity and thickness means an increase in the pore size. Indeed, the increase in pore size compensates the increase in fiber diameter to reserve the same porosity. The increase in pore size enhances the air permeability and decreases the filtration efficiency as shown in Fig. 33. On the other hand, when the fiber diameter keeps increasing beyond this fiber diameter value (315 nm), it is shown from Fig. 30 that the porosity is kept unchanged while the thickness experiences a significant increase. This

increase in thickness leads to a decrease in air permeability and increase in filtration efficiency.

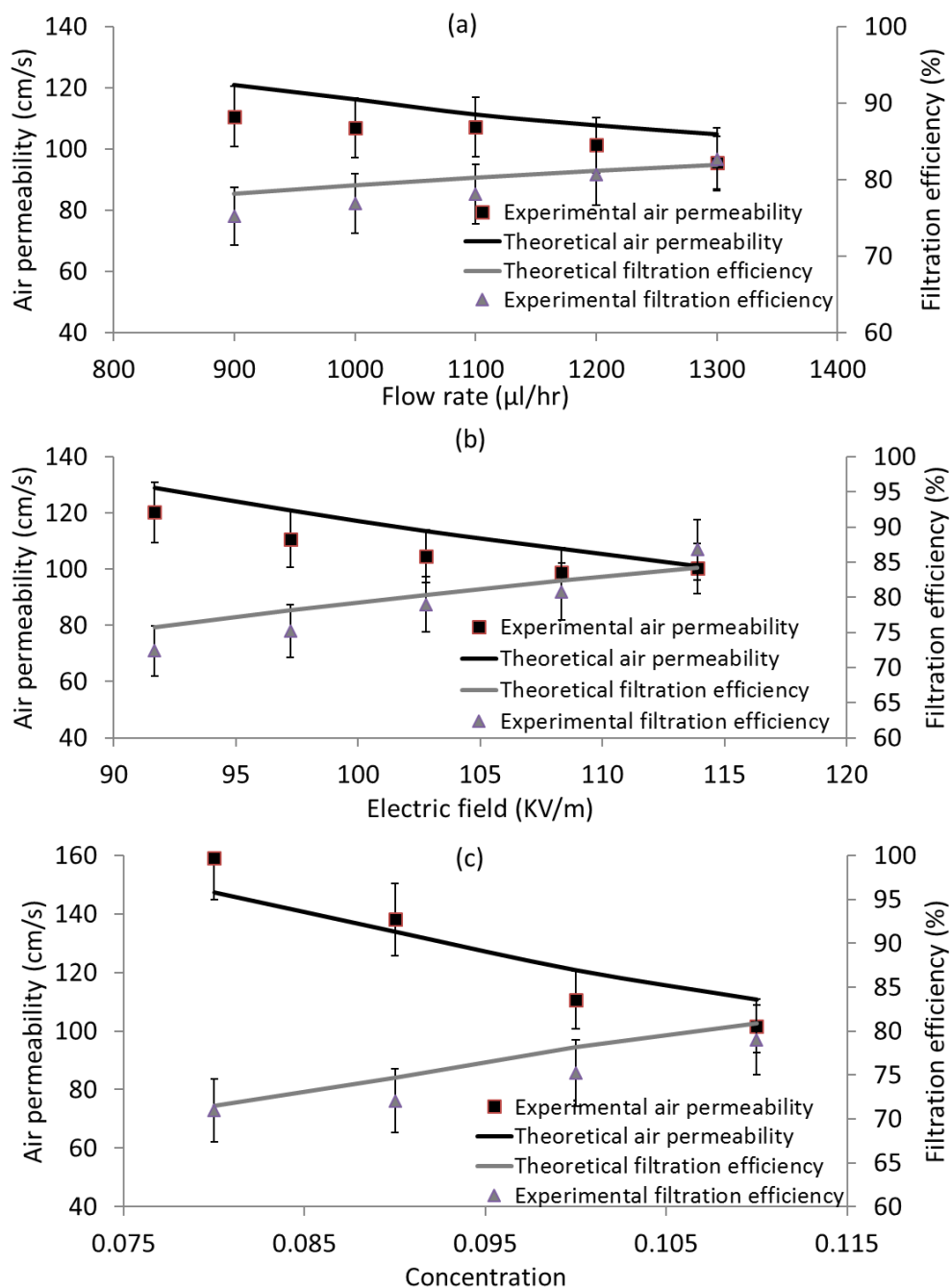


Figure 32: Effect of (a) flow rate (b) electric field (c) concentration on air permeability and filtration efficiency

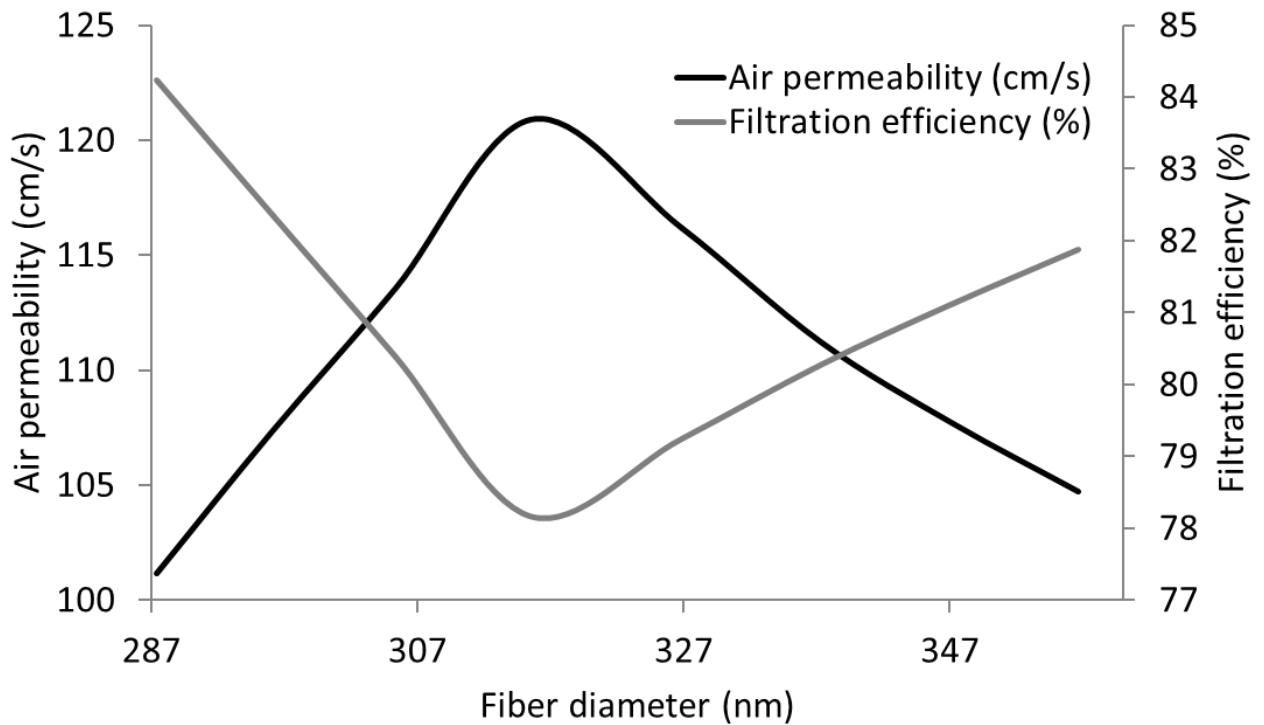


Figure 33: Effect of fiber diameter on air permeability and filtration efficiency

3. Design charts correlation

In order to establish the relation between the nano-fibrous web filtration performance or its air permeability and the electrospinning processing parameters, design charts are developed by performing several simulations (180 simulations) on the combined model(Fig. 34, 35 and 36). First, Fig. 34 (a, b) present the fiber diameter as a function of the electrospinning processing parameters (Q , E) at two different concentrations (8% and 10 %). These design charts could be interpolated to obtain the fiber diameter at the following range of concentrations (8-11 %). The lower limit provides the continuity of the jet while the upper limit is due to the use of the electrospinning model based on the assumption that at the final stage of electrospinning, the competition is between the surface tension and the electrostatic force. This assumption is not applied to relatively high polymer solution concentration ($\geq 12\%$) because in this case the relatively large viscous force prevents the reach of the final stage of bending instabilities. On the other hand, the electrospinning parameters (flow rate and electric field) were chosen in a range to generate a continuous jet without droplets so that the conservation equations are. Fig. 35 shows the ratio of the porosity over the thickness as a function of the fiber diameter for different electrospinning time. Finally, Fig. 36 shows

the air permeability and the air filtration for the nano-fibrous web as function of the porosity/thickness and the fiber diameter.

The utility of these design charts is that it is now possible, for a specific input of electrospinning processing parameters (E , Q , C , and t_e), to predict directly the filtration performance of the nano-fibrous web as well as its air permeability. The design charts allow getting the electrospinning processing parameters for desirable air permeability/ air filtration properties and in other words, they allow going backwards from the output of the combined model to the inputs.

Two examples are considered to illustrate the utilization of these design charts. First, consider a case of a PAN solution of 10 % concentration; this example is presented by a black circle on the design charts figures. For the following processing parameters ($Q=1000 \mu\text{l/hr}$, $E=110 \text{ KV/m}$), Fig. 34(b) predicts a fiber diameter of 300 nm. From Fig. 35, after a deposition time of 30 min, for a fiber diameter of 300 nm, the ratio of porosity over the thickness is about 8%/ μm . For the obtained porosity over thickness, and for the same fiber diameter, Fig. 36 indicates that the air permeability is 38 cm/s and the air filtration for the most penetrating particles is 98%. In another way, consider the case where the desirable air permeability is 100 cm/s, this second example is presented by a black square on the design charts figures. Fig. 36 shows that for this air permeability, we can choose different fiber diameter. In order to have a maximum filtration, it is worth to choose the fiber diameter of 290 nm (filtration efficiency of 85%). For these parameters, the ratio of porosity to thickness is 23 %/ μm . For 290 nm fiber diameter and a ratio of porosity to thickness of 23%/ μm , the time of electrospinning is 10 min. In order to obtain the electrospinning processing parameters, at a concentration of 8 % for example, Fig. 34 (a) shows that the electric field is 110 KV/m, and a flow rate of 980 $\mu\text{l/hr}$. It is of interest to state that, although the design charts give us the ratio of porosity over thickness, however, these two morphological properties could be predicted separately using eq. (6).

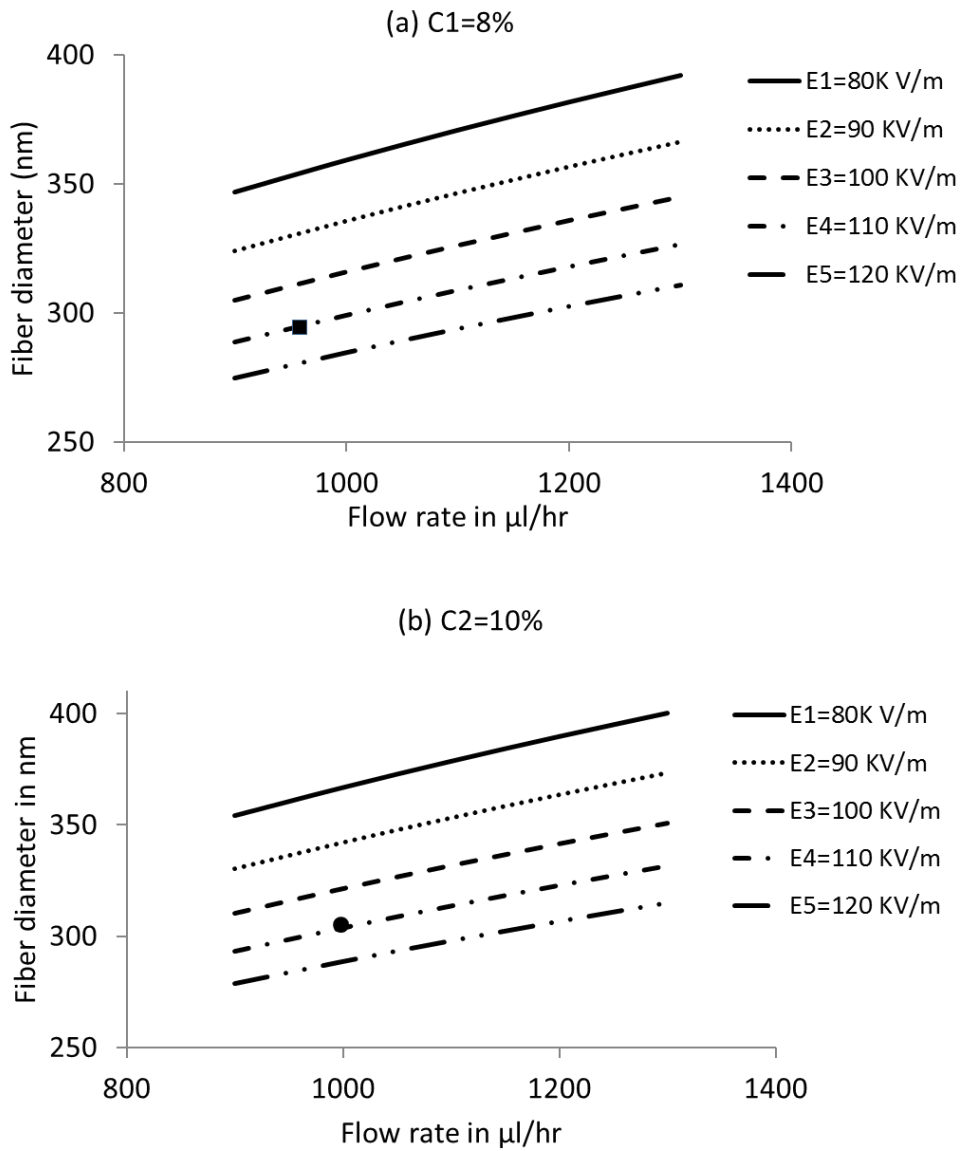


Figure 34: Design chart of the fiber diameter as function of flow rate and electric field at polymer concentration of (a) 8% and (b) 10 %

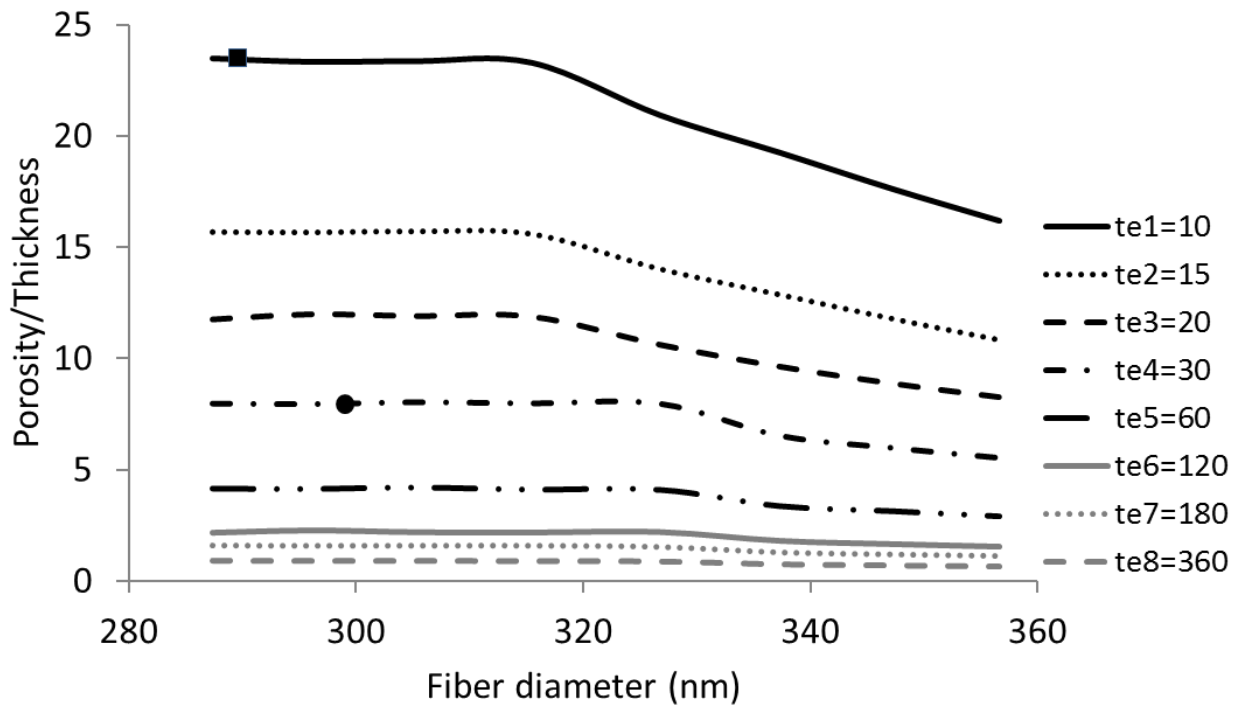


Figure 35: Design chart of the porosity over the thickness as function of fiber diameter for different time of electrospinning

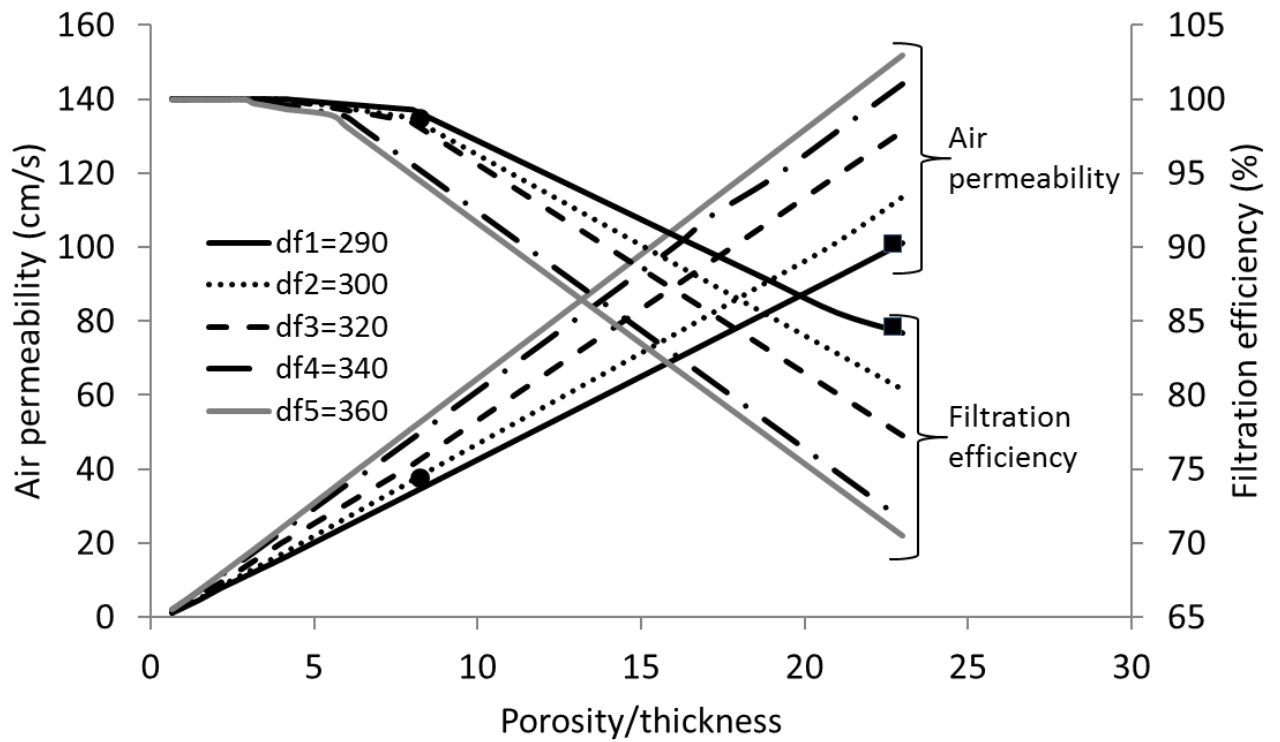


Figure 36: Design chart of the air permeability and filtration efficiency as function of porosity over thickness at different fiber diameters

C. Prediction of the ventilation through clothing by solving the governing equations inside the microclimate air layer

This section focuses on the validation of the simulation results. The strategy of the validation consists of validating the flow characteristics with the CFD simulation at constant cross wind. Then the total ventilation obtained from the connected ventilation of trunk and arm segments will be compared with published experimental data for cases of connected segments and isolated segments. A parametric study then follows to identify the parameters that induce high inter-segmental ventilation.

1. CFD validation

In order to validate the simplified model results, we first study the microclimate flow direction as well as the temperature distribution in axial and angular directions of the air layer in the trunk and arm.

a. Flow direction validation:

It is of interest to validate the direction of the flow at the connection between the clothed arm and trunk. Indeed, the connection of the microclimate zones of the different segments allows the air to be exchanged between them; therefore, when air flows from the microclimate of zone Z4 to that of Z2, supplementary air is forced to enter to zone Z4 to conserve mass. This supplementary air will either come from the opening of aperture Z4 or through normal clothing ventilation thus enhancing the segmental ventilation. But this would result in a decrease in ventilation of the microclimate zone Z2 because air flowing from zone Z4 to Z2 is hotter than air coming from ambient conditions. This in turn forces microclimate air to flow out from the zone Z2. Therefore, some air mass flow rate passes from zone Z2 downward to zone Z1 and leaves from the bottom opening or through clothing. Ke et al. [64] pointed this exchange phenomenon; however, they ignored its effect on ventilation by

closing garment connection during experiments. Therefore, to highlight the effect of the exchange rate between segments on their local ventilation values, the direction of the flow should be determined correctly.

The CFD simulation results of flow leaving the trunk top aperture, flow entering or leaving from the sleeve bottom aperture and the flow in the connection between clothed trunk and arm are shown in figures 37(a), 37(b), and 37(c), respectively at $V_w = 0.9$ m/s and $T_a = 20^\circ\text{C}$. Figure 37(a) shows that the air leaves from the open top trunk upward. Figure 37(b) shows that the connection between the trunk and the arm by the shoulder segment allowed the flow to move from the trunk microclimate air to the arm microclimate air. Since the flow is transferred from the trunk to the arm, some air mass flow rate is leaving from the microclimate air layer of the clothed arm to conserve the mass; this is shown in figure 37(c).

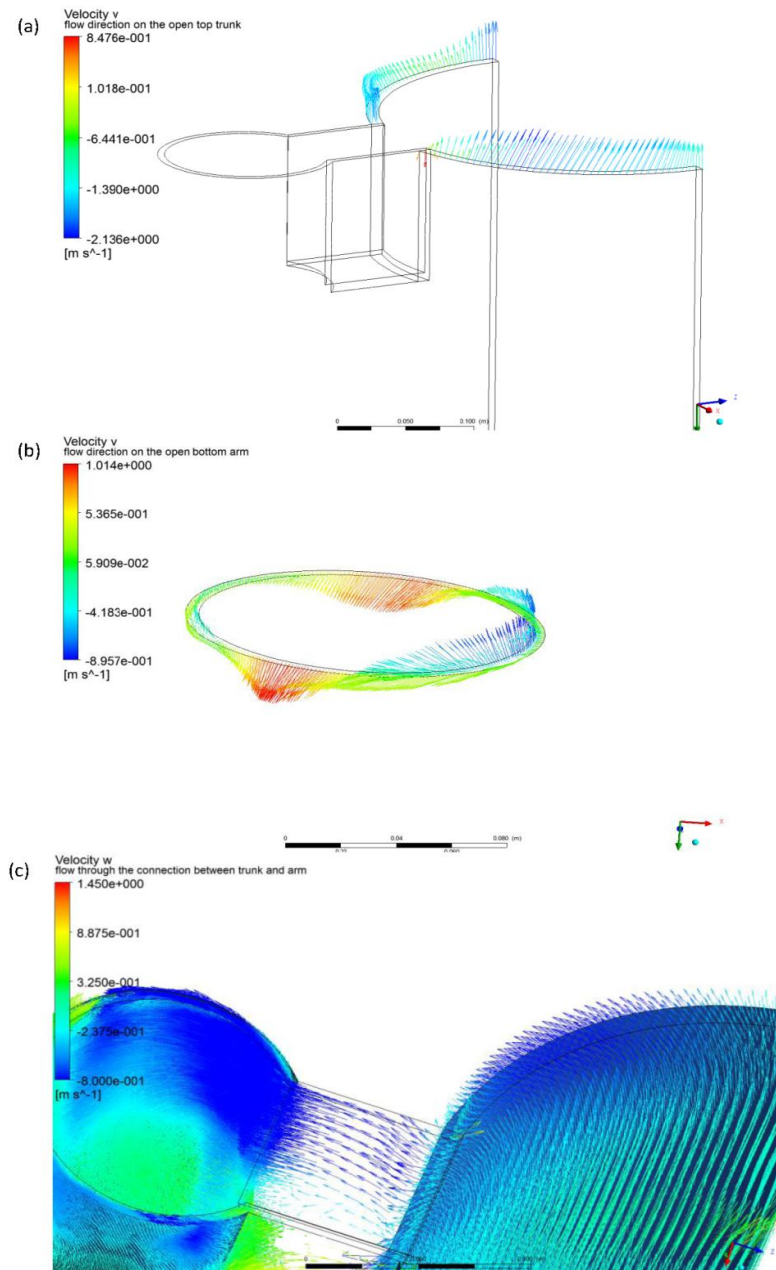


Figure 37: CFD simulation plots of the flow (a) leaving the open top of clothed

trunk (b) leaving and entering the open bottom clothed arm (c) through the connection. In order to validate the velocity field (flow direction and velocity magnitude), simulations on the simplified ventilation model at same conditions are conducted. The upper human body is simulated at $V_w = 0.9 \text{ m/s}$ and $T_a = 20^\circ\text{C}$ and at a segmental air gaps that are approximately estimated by subtracting the jacket circumference size from the human body size divided by 2π . The validation is shown in the corresponding figures 38(a), 38(b), and

38(c). Good agreement is shown between the CFD simulations and the simplified model with an error that does not exceed 14 %.

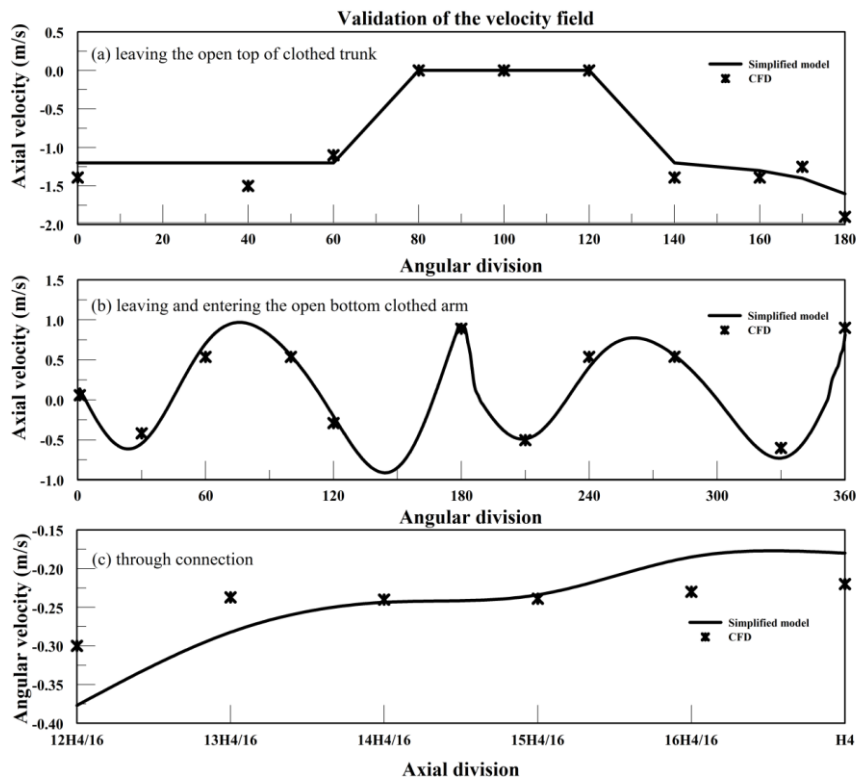


Figure 38: Validation of the velocity field (a) leaving the open top of clothed trunk (b) leaving and entering the open bottom clothed arm (c) through the connection

The effect of the flow direction from the trunk to the arms is shown in figure 39 where the distribution of the pressure over the trunk and over the arm is presented. Clearly, the pressure at the trunk air layer was greater than that of the arm forcing the flow to move from the trunk to the arm. In addition, the pressure at the opening bottom end of the arm was negative and positive relative to ambient pressure. For this reason, some of this flow in the arm clothing annulus is lifted up and some of this flow is pushed down (see figure 37(b)). Finally, the positive pressure of the upper part of the trunk illustrates clearly the upward flow of the opening at the top end of the trunk.

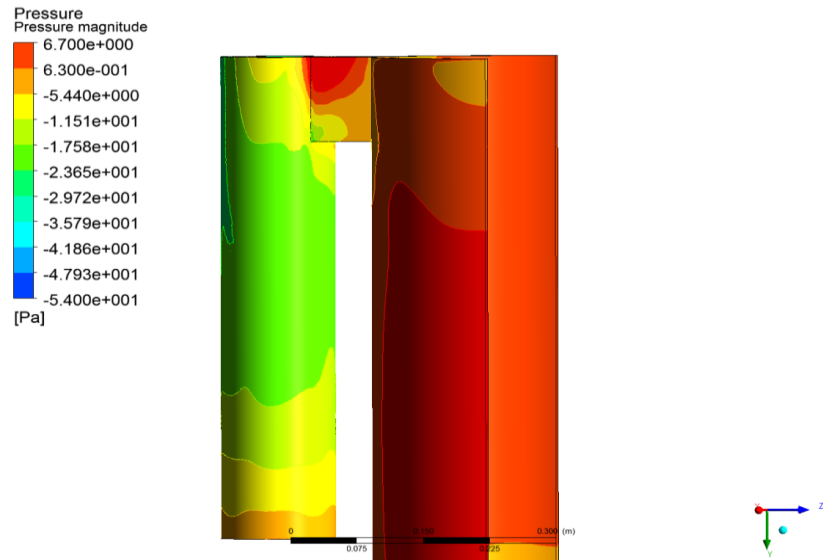


Figure 39: Distribution of the relative pressure obtained from CFD simulation

b. Temperature validation

Figures 40(a), 40(b), 40(c), and 40(d) show the variation of the model predicted temperature in the microclimate air layers of four zones (Z1, Z2, Z2, Z4) and corresponding averaged valued calculated by the CFD model at $V_w = 0.9$ m/s and $T_a = 20$ °C.

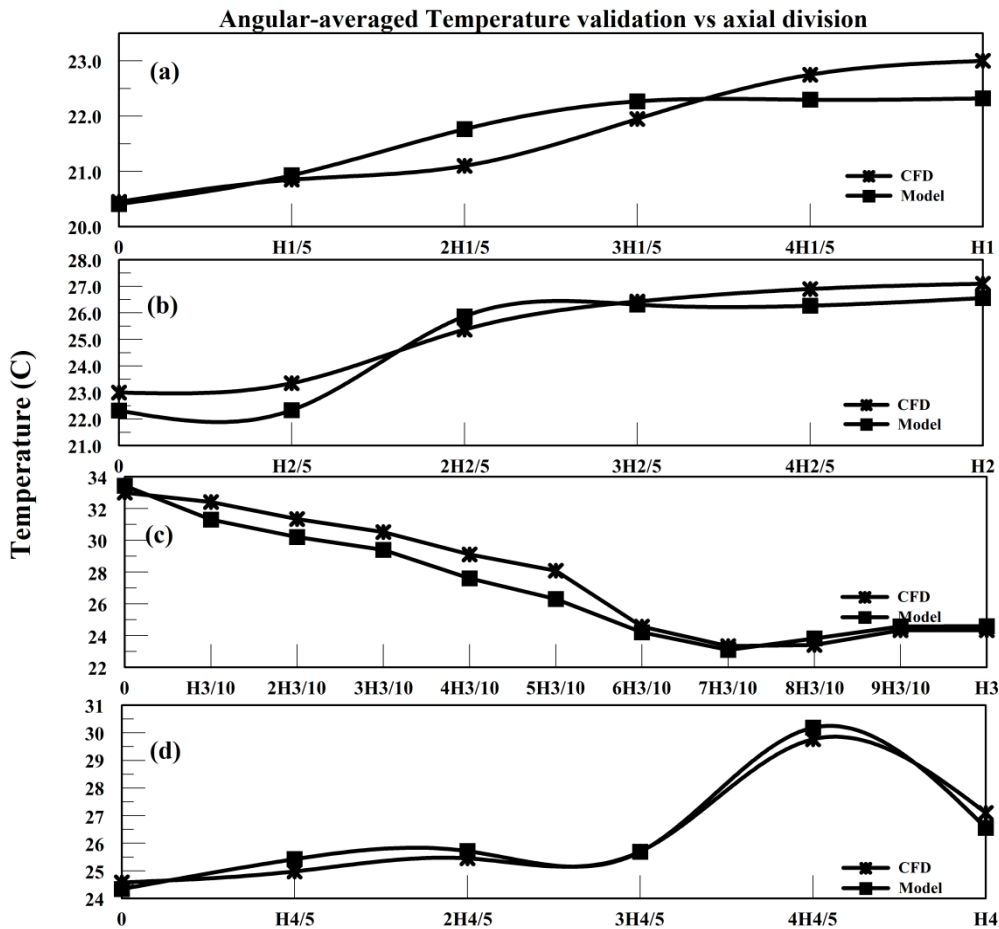


Figure 40: Angular-averaged axial temperature validation obtained from the ventilation model at (a) zone Z1 (b) at zone Z2 (c) at zone Z3 (d) at zone Z4

Figure 40(a) shows the variation of the angular-averaged temperature in axial direction of the lower clothed arm (Z1) versus its height H1. The temperature increased from the ambient temperature at the bottom opening as expected due to the warm skin. Figure 40(b) shows the validation of the angular-averaged temperature in axial direction for the upper clothed arm versus its height H2. The temperature was also found to increase because of two factors: (i) (Z2) is connected to (Z4) where the top end is partially closed; and (ii) the top end of (Z2) is connected to the clothed trunk where the microclimate air layer is closed (the under arm region). Figure 40(c) shows the validation of the angular-averaged temperature of the microclimate trunk (Z3) versus its height H3. The temperature decreased from the skin

condition at the closed bottom end. The increase in the angular-average temperature at the top end of zone Z3 was also due to the skin temperature under the arm. Figure 40(d) shows the validation of the angular-averaged temperature of the connection zone (Z4) versus its height H4. The temperature increases axially because the top end was partially closed where the skin conditions were applied at the closed part and zero-gradient was applied at the open part.

2. Model validation with published experimental data

The mathematical ventilation model developed in this study elaborates the effect of connection on the overall ventilation. The aim of this section is to validate the overall ventilation rates through a permeable jacket ($\alpha=0.135$ m/s) at different wind velocities with published experiment [64] where the connection between segments is left open to allow the air exchange between them. Furthermore, the segmental ventilation rates computed with opened connection condition are compared with the segmental ventilation rates computed with closed connection condition (independent cylinders). This comparison will show up the effect of connections on varying the ventilation rates and the necessity to include their effects in order to approach more accurately the experimental values of ventilation rates.

Ke et al. [64] used a steady state tracer gas method for measuring the microclimate ventilation rates. Nitrogen (N_2) was chosen as tracer gas. Three wind speeds were used: $V_w \leq 0.1$ m/s (no wind), $V_w = 0.6$ m/s and $V_w = 0.9$ m/s. The experiment was carried out on a standing shop manikin in an air conditioned chamber at 20°C ambient temperature and 40% ± 10 % relative humidity. The dimensions used in the published experiment (garment S1) are the same used in the model. Table 8 shows the total ventilation values predicted by the connected model as compared with the published experimental values at different wind speeds for the same permeable jacket when the connection effect is included and when it is

excluded. It is observed that the connected model is closer in accuracy to the published experiment (with an error not exceeding 12 %) than the unconnected one (with an error exceeding 15 %) at relatively high wind speeds ($V_w \geq 0.6$ m/s). However, it shows approximately the same result at low wind speeds ($V_w \leq 0.1$ m/s).

Another recent experiment is held by ke et al. [77] on a thermal manikin heated at $T_{skin}=35$ °C in an air conditioned chamber at 20°C ambient temperature and $50\% \pm 5\%$ relative humidity. Two wind speeds were used: $V_w \leq 0.3$ m/s (here we assume it at 0.3 m/s), $V_w = 1.1$ m/s. In this study, the connection is also kept open; the local ventilation is calculated using the tracer gas method equation that neglects the inter-segmental ventilation effect. Therefore, in order to validate our work, the local ventilation of chest, back and arm are summed to find the total ventilation rate. Table 9 shows the total ventilation values predicted by the connected model as compared with the published experimental values at two different wind speeds for the garment G1 of 0.135 m/s permeability. Good agreement is found between the connected mathematical model and the published experiment as the predicted values fall within the ranges provided by the published data.

Table 8: Validation of the model ventilation at different wind speeds

V_w (m/s)	0.1		0.6		0.9	
Experiment ventilation ³ (l/min)	36.57		44.5		58.5	
	Ventilation (l/m)	relative error (%)	Ventilation (l/m)	relative error (%)	Ventilation (l/m)	Relative error (%)
Model connected (l/min)	32.12	12.16	40.65	8.65	60.01	2.58
Model unconnected (l/min)	32.54	11.02	37.79	15.07	55.09	5.82

Table 9: Validation of the model ventilation at different wind speeds

V_a (m/s)	0.3	1.1
Experiment ventilation (l/min)	55.27 ± 6.6	82.73 ± 7.79
Model connected (l/min)	48.12	75.1

3. Parametric study

In order to understand the effect of connection on the ventilation rate, it is of interest to isolate the new parameter; the inter-segmental ventilation and compute its value under different flow conditions and for different physical and geometric clothing parameters. This inter-segmental ventilation is defined as the air mass flow rate (l/min) that flows from the trunk to the arm. This parameter is important because of its impact in varying the segmental ventilation of the trunk and the arm. In the case of the flow of air from the trunk to the arm, the air will enter the trunk air layer from the ambient conditions through clothing and will leave through the arm connection, or the clothing, or the top opening. This will cause an increase of trunk ventilation and a decrease of arm ventilation because the air that enters the arm microclimate is heated and is hotter than the ambient air. The developed model gives us the net mass flow rate (l/min) leaving the trunk and entering the arm. However, different factors influence the inter-segmental ventilation and these parameters include wind speed, clothing permeability, and clothing apertures. In order to study the impact of these different factors on the inter-segmental ventilation, we assume that the inter-segmental ventilation is positive if the flow of air is from the trunk to the arm and negative vice versa.

Figure 41(a) shows the inter-segmental ventilation using a permeable jacket ($\alpha=0.135$ m/s) at different wind speeds. It was shown that when the velocity increases, the inter-segmental ventilation increased. At low wind speeds ($V_w \leq 0.1$ m/s), it was found that the inter-

segmental ventilation was no longer significant. In this case, the trunk and the arm can be modeled as independent segments. However, at high wind speeds ($V_w \geq 0.9$ m/s), the inter-segmental ventilation exceeds 5 l/min. Another important factor that affects the inter-segmental ventilation is the clothing permeability. In general, the jacket permeability allows air to enter to the segmental microclimate air layers and the interconnection allows the air exchange between the segments. In order to study the impact of permeability on the inter-segmental ventilation, different jacket permeability are investigated at a wind speed of 1 m/s. Figure 41 (b) illustrated this impact. It was shown that at relatively high permeability ($\alpha = 0.135$ m/s), the inter-segmental ventilation was significant and reaches 5 l/min. However, at lower permeability ($\alpha = 0.05$ m/s), the connection impact vanished and the air exchange between the trunk and the arm was no longer important. The third important parameter that affects the inter-segmental ventilation is the opening at the bottom end of the lower arm and at the neck. Figure 41(c) illustrated this effect by estimating the inter-segmental ventilation at different apertures. At $V_w = 1$ m/s and for a permeable jacket ($\alpha = 0.135$ m/s), it was found that the inter-segmental ventilation became more significant when the bottom opening of the arm was open than when it was closed. This is because the pressure at the arm microclimate air layer increases when the bottom end of the arm is closed. This pressure increase caused lower air exchange leaving the trunk to the arm. However, this was not the case when the top end of the trunk was closed. No significant variation in the inter-segmental ventilation in both cases: open top end or closed top end.

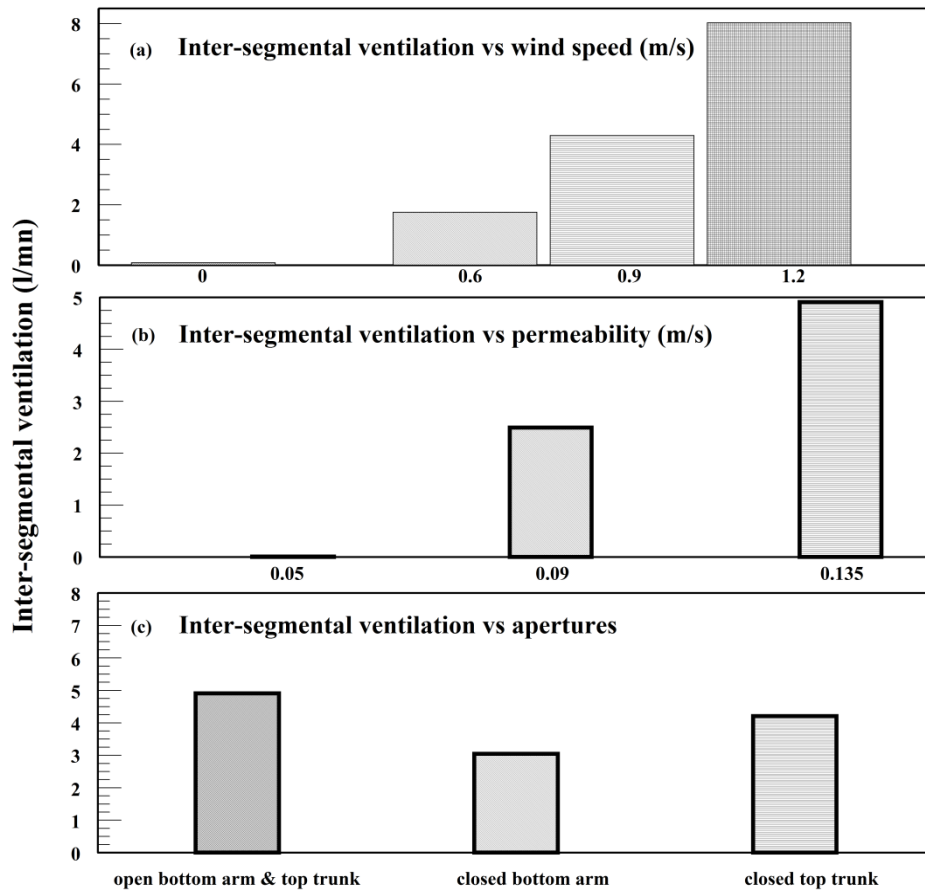


Figure 41: Estimation of the inter-segmental ventilation obtained from the ventilation model as a function of (a) wind speed (b) permeability (c) apertures

As discussed earlier, the inter-segmental ventilation causes the trunk ventilation to increase by allowing some fresh air mass flow rate to penetrate instead of the heated mass flow rate (inter-segmental ventilation). Indeed, the trunk ventilation is essential in providing the human comfort. It is considered as the most influential segment because of its highest segmental heat loss. Several studies that are related to this issue and to the segmental thermal sensation have been recently tackled.

Table 10 summarizes the trunk ventilation increase at different conditions. It was observed that the inter-connection provided an important role in increasing the trunk ventilation by more than 15 % at high wind speeds ($V_w \geq 0.9$ m/s), relatively high permeability ($\alpha=0.135$

m/s), and open bottom arm apertures. On the other hand, the heated air mass flow rate that enters the arm microclimate layer causes a decrease in the arm ventilation.

Table 10: Percentage increase of trunk ventilation at different conditions

	Trunk connected (l/min)	Trunk unconnected (l/min)	Increase (%)
$V_w = 0.1$ m/s; $\alpha = 0.135$ m/s Open bottom & open top	1.04	1.04	0.40
$V_w = 0.6$ m/s; $\alpha = 0.135$ m/s Open bottom & open top	15.17	13.22	14.73
$V_w = 0.9$ m/s; $\alpha = 0.135$ m/s Open bottom & open top	35.83	31.06	15.35
$V_w = 1.2$ m/s; $\alpha = 0.135$ m/s Open bottom & open top	63.69	54.77	16.28
$V_w = 1.0$ m/s; $\alpha = 0.05$ m/s Open bottom & open top	16.39	16.38	0.06
$V_w = 1.0$ m/s; $\alpha = 0.09$ m/s Open bottom & open top	29.50	26.60	10.90
$V_w = 1.0$ m/s; $\alpha = 0.135$ m/s Open bottom & open top	44.23	38.46	15.02
$V_w = 1.0$ m/s; $\alpha = 0.135$ m/s Closed bottom & open top	42.05	38.46	9.32
$V_w = 1.0$ m/s; $\alpha = 0.135$ m/s Open bottom & closed top	43.82	38.18	14.79

Table 11 summarizes the arm ventilation reduction when considering the connected segments. It was shown that that the inter-connection provided a reduction in the arm ventilation by more than 5 % at high wind speeds ($V_w \geq 0.9$ m/s), relatively high permeability ($\alpha=0.135$ m/s), and open bottom arm apertures.

Table 11: Percentage change of arm ventilation at different conditions

	arm connected (l/min)	arm unconnected (l/min)	Decrease (%)
$V_w = 0.1$ m/s; $\alpha = 0.135$ m/s Open bottom & open top	16.37	16.62	1.50
$V_w = 0.6$ m/s; $\alpha = 0.135$ m/s Open bottom & open top	13.1	13.53	3.17
$V_w = 0.9$ m/s; $\alpha = 0.135$ m/s Open bottom & open top	12.21	12.63	3.32
$V_w = 1.2$ m/s; $\alpha = 0.135$ m/s Open bottom & open top	15.35	17.34	11.47
$V_w = 1.0$ m/s; $\alpha = 0.05$ m/s Open bottom & open top	8.00	8.32	3.84
$V_w = 1.0$ m/s; $\alpha = 0.09$ m/s Open bottom & open top	10.89	11.38	4.30
$V_w = 1.0$ m/s; $\alpha = 0.135$ m/s Open bottom & open top	12.94	13.59	4.78
$V_w = 1.0$ m/s; $\alpha = 0.135$ m/s Closed bottom & open top	13.36	13.85	3.53
$V_w = 1.0$ m/s; $\alpha = 0.135$ m/s Open bottom & closed top	13.24	13.59	2.57

The developed simplified model and the inter-segmental ventilation behavior may be used in the design of protective clothing where improved ventilation of the human trunk is needed which can be achieved by increasing inter-segmental ventilation from the trunk to the arm through the connection.

3. Experimental evaluation and validation of IS and local ventilation using the integrated bio-heat and clothing inter-connected cylinders Models

For each clothing jacket case, three experiments were conducted where N₂ injection was (i) for both the clothed trunk and the arm; (ii) for the clothed arm only (iii) for the clothed trunk only. The experiment show that the outlet oxygen concentration for the trunk in both cases (low and high permeable jacket) was invariant and was similar to the ambient O₂ concentration when only the arm was injected with excess Nitrogen. This means that in both cases, the flow rate of microclimate air at the inter-connection was not driven from the arm to the trunk.

When the trunk was injected, different scenarios emerged for the two jackets. In the first case (low permeable jacket), the outlet oxygen concentration for the arm was similar to the ambient oxygen concentration when the trunk was injected with excess nitrogen. This means that negligible air mass flow rate was being driven through the connection from the trunk to the arm. On the other hand, the outlet oxygen concentration for the trunk in the second case of high permeable jacket was smaller than the ambient O₂ concentration which meant that a certain microclimate mass flow rate was being driven from the trunk to the arm and should be computed. This emphasizes the effect of air permeability on the inter-segmental ventilation. In fact, the jacket air permeability allowed air to enter to the segmental microclimate air layers while the inter-connection allowed the air exchange between the segments.

Note that the analytical solution for inter-segmental ventilation was obtained by integrating the mathematical model of the inter-connected clothed cylinders' ventilation model developed. However, the experimental calculations were achieved by using the tracer gas method on a thermal manikin and solving the mass balances of tracer gas for three injection scenarios of the tracer gas. Figure 42 shows a comparison between the analytical and the

experimental segmental ventilations for both cases. The error bars represent the range of the ventilation values found by the repeated experiments conducted for each case. Good agreement was observed between the analytical predictions of local and inter-segmental ventilations with those experimentally calculated. The results showed that the inter-segmental ventilation was significant for the case when air permeability was relatively high. Indeed, the inter-segmental ventilation formed about 30% of the arm total ventilation and about 14% of the trunk total ventilation. Therefore, it is clear that inter-segmental ventilation should not be neglected particularly when accurate estimation of segmental ventilation rate is sought.

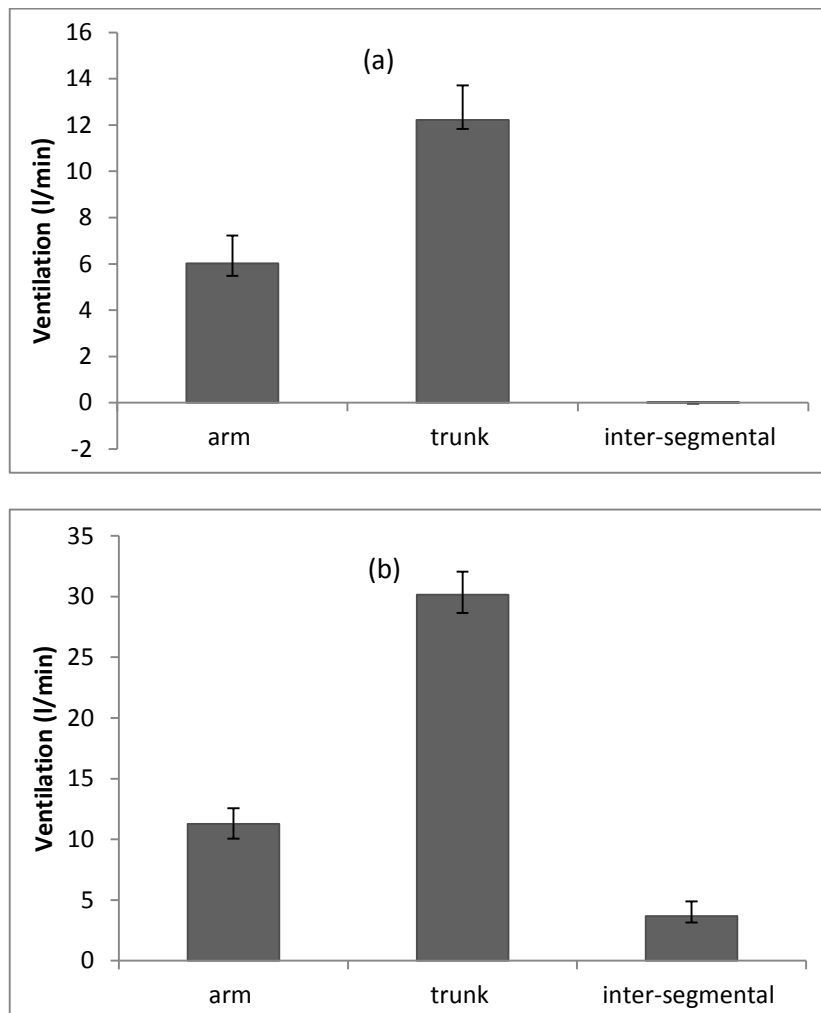


Figure 42: Comparison between the analytical and experimental ventilations in (a) case 1 of low permeable clothing (b) case 2 of high permeable clothing

Table 11 presents a comparison between the analytical and experimental segmental ventilation and heat losses in both cases of open and closed connection for the high permeable jacket. The analytical heat losses were found from the integrated ventilation model with the bio-heat model. The experimental heat losses were given by the thermal manikin software and they were defined as the necessary heat flux used to reach the segmental skin temperatures given from the bio-heat model at the given metabolic rate. Good agreement was observed between the analytical and the experimental results with a relative error that did not exceed 10 % for the segmental ventilation and a relative error of a maximum of 5 % for the segmental heat losses. Furthermore, data presented in Table 12 revealed that the inter-connection affected the segmental ventilation and heat losses for both arm and trunk. The heat losses and ventilation from the trunk decreased when the connection was closed. However, this was compensated by an increase of the arm ventilation and heat losses. The main reason for this behavior is that the heated air that flowed from the trunk to the arm when the connection was open allowed more fresh air to enter the trunk. This fresh air increased the segmental ventilation of the trunk by 12 % and the heat losses by 5.46 %. On the other hand, the heated air that left the trunk and entered the arm decreased the arm ventilation by 3% and the heat losses by 6.68 %. The importance of this finding stems from the fact that the trunk is the most influential segment in body heat loss and any increase in the trunk ventilation and heat losses would enhance the thermal comfort of the human body.

Table 12: Comparison between predicted and experimentally measured values of segmental ventilation and heat losses between open and closed connection

Segment	Connection configuration	Predicted value by Model	Experimentally measured value
---------	--------------------------	--------------------------	-------------------------------

		Ventilation (<i>l/min</i>) with a standard deviation of ± 0.05	
Arm	open connection	11.26	10.56
	closed connection	12.03	10.856
Trunk	open connection	31.20	30.88
	closed connection	28.63	27.5
Segment	Connection configuration	Heat losses (W/m^2) with a standard deviation of ± 0.05	
Arm	open connection	52.15	53.3
	closed connection	56.70	57.12
Trunk	open connection	64.91	65.4
	closed connection	59.13	61.54

The inter-segmental ventilation was evaluated from the validated mathematical model as a function of the different parameters affecting its value. These parameters are: the air permeability, the wind speed, the mean air gap of the upper human body trunk, and the aperture design. A statistical correlation was derived using the validated model results for each of the designs of jacket apertures mentioned in section 2: (A) open bottom arm and open top trunk; (B) open bottom arm and closed top trunk; (C) closed bottom arm and open top trunk. Eighty simulations were performed using the developed mathematical model for each aperture design case to evaluate inter-segmental ventilation (*IS*) at equal increments of each of the influencing parameters. The increment of air permeability was $\Delta\alpha = 0.01 \text{ m/s}$ at constant $V_w=1.2 \text{ m/s}$ and $y=2.5 \text{ cm}$. The increment of wind velocity is $\Delta V_w=0.1 \text{ m/s}$ at constant $\alpha=0.135 \text{ m/s}$ and $y=2.5 \text{ cm}$. The increment of air gap size is $\Delta Y = 0.1 \text{ cm}$ at constant $\alpha = 0.135 \text{ m/s}$ and at constant $V_w=1.2 \text{ m/s}$.

The statistical analyses was performed using the SPSS© software package where the predicted *IS* at each parameter were subject to a linear regression to derive a correlation for

each aperture design. The SPSS software generates the correlations after a number of iterations depending on the initial value given until the relative reduction between successive residual sums of squares is of order of 10^{-8} .

The generated equations from the statistical analysis for clothing aperture cases A, B, and C are given by

$$(A) \quad IS = 83.68 * \alpha + 12.38 * V_w + 3.26 * Y - 26.86 \quad (R^2 = 0.982)$$

) (49a)

$$(B) \quad IS = 62.99 * \alpha + 9.61 * V_w + 2.27 * Y - 19.86 \quad (R^2 = 0.983)$$

(49b)

$$(C) \quad IS = 84.08 * \alpha + 11.86 * V_w + 3.17 * Y - 26.38 \quad (R^2 = 0.981)$$

(49c)

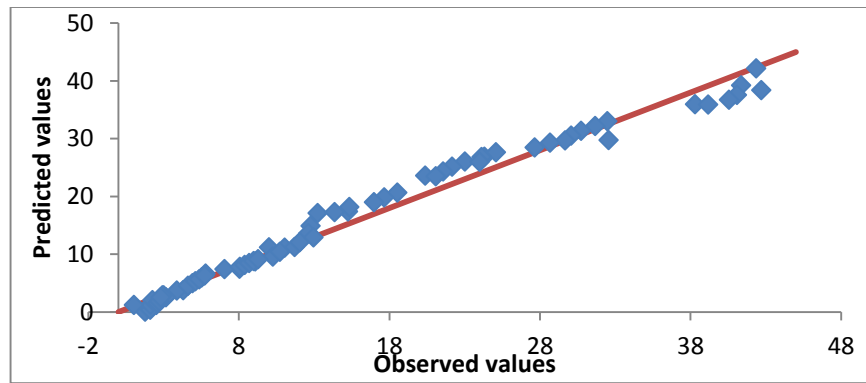
where α is the air permeability in m/s , V_w is the wind velocity in m/s , Y is the microclimate air gap in cm , IS is the inter-segmental ventilation in l/min . Figure 43 (a-c) shows parity plot of inter-segmental ventilation for each clothing aperture case A, B, and C respectively. The observed values and the predicted values lie close to the $y = x$ line which indicated that the observed and the predicted values agree together.

A sensitivity analysis is performed to study the influence of each parameter in the inter-segmental ventilation. It is obvious that the inter-segmental ventilation increases with the increase of all three parameters given that all the correlation coefficients multiplied by the air permeability, the wind velocity, and the microclimate air gap are positive. However, the rate of increase varies depending on the parameter. For example, an increase of 20 % in wind speed results in about 25% increase in the inter-segmental ventilation for the three aperture type cases. However, an increase of 20% in air permeability leads to an inter-segmental increase of about 28 % for the same cases. The lowest rate of increase is observed for the air

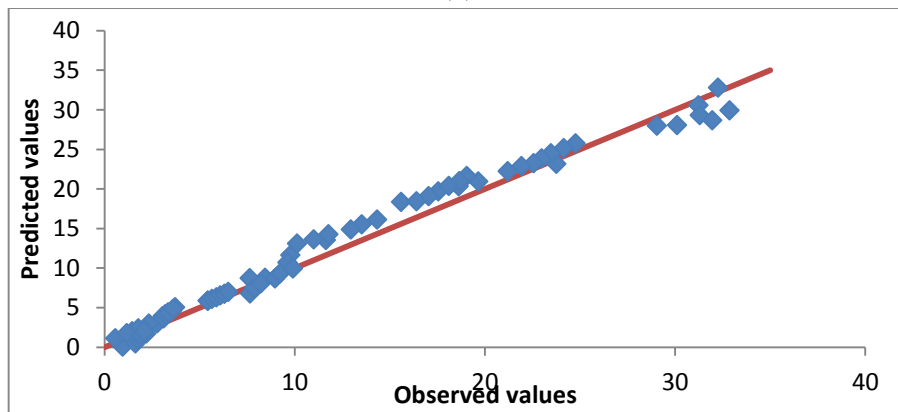
gap size where a 25% increase in size leads to an increase of 18 % only. This means that the air permeability is the most influencing parameter followed by the wind speed and then the air gap size within the ranges specified for the applicability of equation (49):

$$0.05 < \alpha < 0.3(m/s) \quad ; \quad 0.5 < V_w < 4(m/s) \quad \text{and} \quad 0.5 \leq Y \leq 3(cm)$$

(50)



(a)



(b)

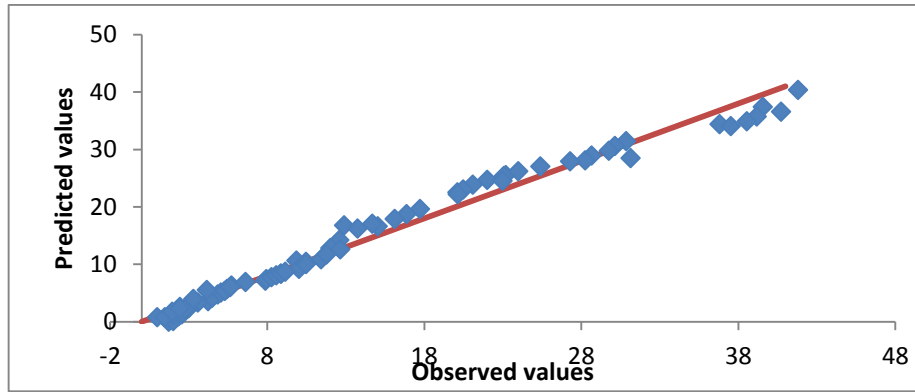


Figure 43: Inter-segmental ventilation (l/min) parity plot for case (a) open bottom and open top (b) closed bottom and open top (c) open bottom and closed top

(c)

By following the same scenario adopted to find the inter-segmental ventilation correlation, the correction factors of the arm and the trunk closed-connection ventilations were generated using a nonlinear regression method. The correction factor is the ratio of the corrected local ventilation occurring when the inter-connection is open to the local ventilation occurring when the inter-connection is close. The corrected local ventilation was predicted by simulating the validated integrated connected clothed cylinder model of current work while the local ventilation at zero IS was obtained using the unconnected clothed cylinder model. Therefore, the correction factors for local ventilations VR_{arm} and VR_{trunk} are given respectively as follows:

$$CF_{arm} = -0.0014IS^3 + 0.0127IS^2 - 0.029IS + 0.9719 \quad (R^2 = 0.9855)$$

(51a)

$$CF_{trunk} = -0.001IS^3 + 0.00837IS^2 + 0.0134IS + 1.0249 \quad (R^2 = 0.9026)$$

(51b)

The above correction factor correlations are applicable for the range of air permeability, velocity and gap size given in equation (50). Because the clothing inter-connection results in a decrease of arm ventilation and an increase of trunk ventilation, CF_{arm} is always smaller than unity while CF_{trunk} is always greater than unity. Using correction factors of equations (51 a) and (51 b) to adjust the experimentally estimated local ventilation of the arm and trunk when the inter-connection was closed for the high permeable jacket data, the resulting corrected local ventilation of the arm and trunk was that of the experimentally obtained values when the inter-connection was open, hence providing additional confidence in the obtained correlations using the unconnected clothed cylinder and the connected clothed cylinders models.

D. Electric circuit analogy of the ventilation through clothing

1. Independent clothed segment

In this section, the model is validated by comparing the results of segmental and overall ventilation rates with different published experiments at different conditions. Different permeability, wind speed, oscillation frequency (for the clothed arm), walking conditions and aperture configurations are investigated.

Ke et al. [66] used the tracer gas method to measure the local ventilation rates of the arm and trunk for different working garments. The experiment was based on injecting the nitrogen gas (tracer gas) after pre-mixing it with air into different locations in the garment. Then, the nitrogen concentrations were measured at the inlet and outlet using the N_2 analyzer. For each location, the microclimate ventilation rate was estimated using the tracer gas equation, and the average ventilation was reported for the local ventilation rate. Different conditions were examined: different garment permeability (0-0.135 m/s), different wind speeds (0, 0.6 m/s, and 0.9 m/s), and different aperture configurations (close or open conditions of the garment). The experiment was carried out in an air conditioned chamber using a standing up shop manikin.

Ke et al. [64] investigated the local ventilation rates of an impermeable garment at two activities (static, walking) and two wind speeds (no wind, 1.2 m/s). The experiment was based on injecting Argon gas (tracer gas) after pre-mixing it with air into different locations in the garment. Then, the argon concentrations were measured at the inlet and outlet using a mass spectrometer. As usual, the microclimate ventilation rate was estimated using the tracer gas equation for each location, and the average ventilation was reported for the local ventilation rate. The experiment was carried out in an environmental chamber using a walking thermal manikin.

The third experiment was published by Ghaddar et al. [70] to determine the ventilation induced by swinging motion and external wind for a fabric covered cylinder representing the limb. The experiment was conducted in a controlled environmental chamber using a permeable clothing fabric (0.05 m/s) tested at different wind speed and oscillating frequency. The periodic rotational motion of the inner cylinder was provided by a dc motor by means of three-bar mechanism. The ventilation rates were estimated using a tracer gas method (N_2 as a tracer gas). All of these experiments measured the local ventilation rates of the upper human body segments. The overall ventilation rate is validated using the published experiment of Ueda et al. [100]. In this experiment, the overall ventilation rate was measured using a tracer gas technique tested on human subjects wearing a coverall of a specified air resistance ($0.3 \text{ KPa}\cdot\text{s}/\text{m}$) under the following conditions: standing still or walking at 1 m/s, in still air and in wind condition at 1 m/s for opened and closed suits. The effect of openings on ventilation rates of the overall human body is also investigated. The openings were located only on the collars and cuffs; no openings exist on the clothed legs.

In order to validate the ventilation rate of the clothed trunk subjected to wind, the experiment of Ke et al. [66] is used. The inputs to the simplified model are the geometrical dimensions, the air permeability of the fabric, the wind speed, the aperture configuration, and the walking speed. In this comparison, the trunk is static, thus the walking speed is zero. In order to achieve the comparison, the same conditions of the experiment are adopted. The height, radius, and air gap of the clothed trunk are respectively 65 cm, 14 cm, and 5 cm. When the garment used is impermeable, the air permeability used in the model is 0.005m/s or less than that; moreover, when there is no wind condition, the air speed used in the model is 0.01 m/s or less than that. The main reason is that the model limitation does not accept zero permeability and wind condition. When considering the opening aperture in the simplified model, the axial flow rate is included and vice versa. Fig. 44 illustrates the comparison

between the ventilation rates of the simplified model and the experiment performed by Ke et al. [66]. Although the mean relative error between the experimental and the predicted ventilation rates was 30%, all the predicted ventilation rates were within the range of the standard deviation provided by Ke et al. [66]. The main reason is that the standard deviation was relatively large. No comparison was achieved between the experiment and the simplified model in the case of impermeable garment when the aperture is closed (fig. 44(a)) since in this case, there is no way for the air to enter the microclimate layer. In their experiment, Ke et al. [66] reported the ventilation rates for this case at different wind speed. They justified these finding by telling that the opening cannot be totally closed experimentally; thus, their experimental results in this closed impermeable apertures were not reliable. The maximum ventilation rate is obviously attained at high permeability and wind speed (38 l/min) for the opening aperture. Fig. 44(b) shows that an increase of 50% in wind velocity induces an increase in ventilation rates of 44 % for opened aperture compared to 33 % for closed apertures. The **Fig. 44:** Comparison between the ventilation obtained by the simplified model and the published experiments⁸ for the clothed trunk at different wind velocity and aperture geometries for (a) impermeable open aperture and (b) permeable open and closed apertures.

reason behind these findings is that the pressure near the opening (P_{o1}) increases with the increase of wind speed, thus, the pressure difference ΔP_x increases allowing more air to enter through the opening.

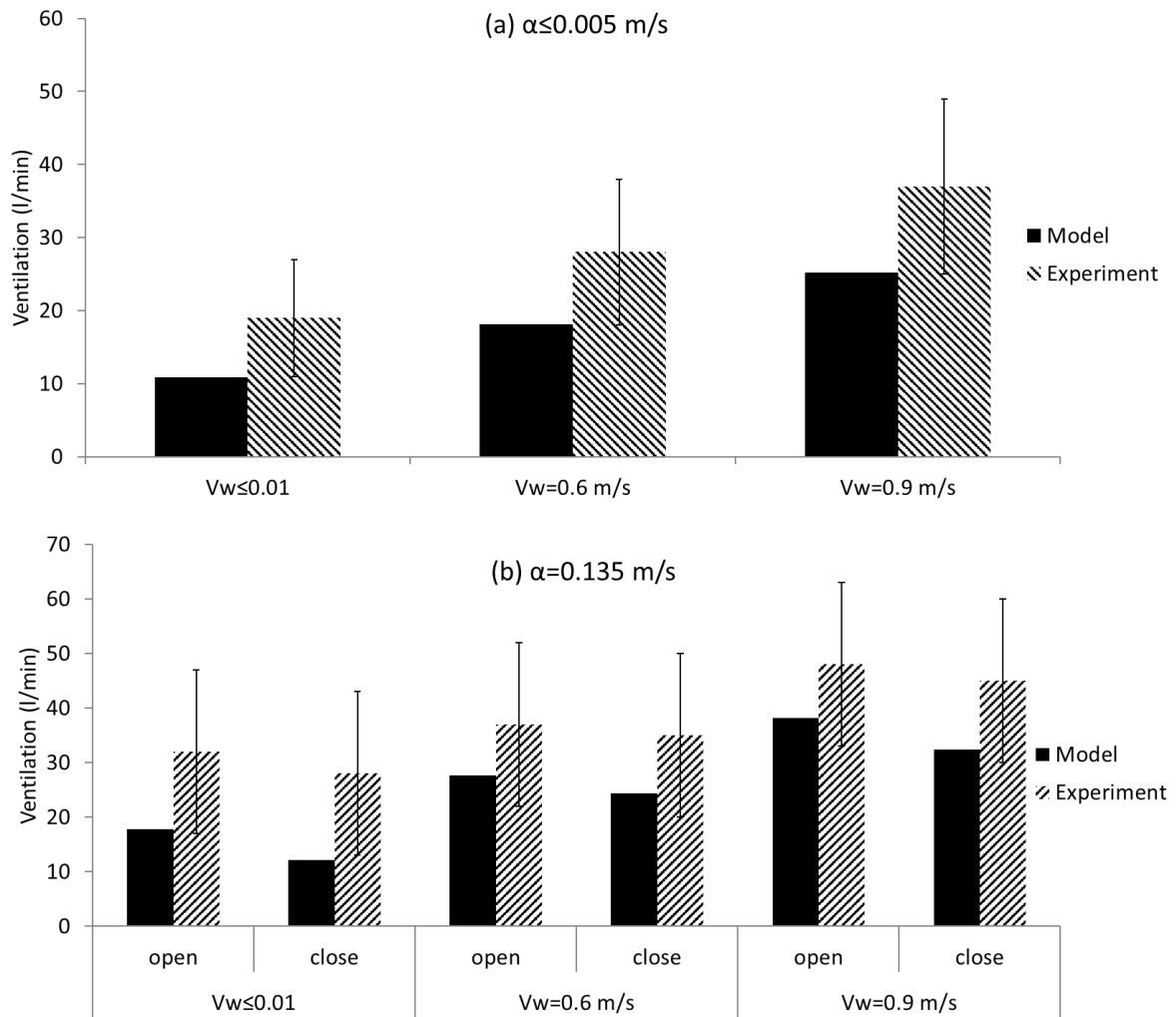


Figure 44: Comparison between the ventilation obtained by the simplified model and the published experiments⁸ for the clothed trunk at different wind velocity and aperture geometries for (a) impermeable open aperture and (b) permeable open and closed apertures.

Case of impermeable clothing

In order to validate the ventilation rate of the impermeable clothed subject subjected to oscillating motion and wind, the experiment of Ke et al. [64] is used. The simplified model of the clothed arm subjected to oscillating motion and wind is thoroughly described. The inputs to the oscillating arm model are the geometrical dimensions of the clothed arm, the air permeability of the fabric, the wind speed, the aperture configuration, the oscillating frequency, and the oscillating amplitude. The height, radius, and air gap of the clothed arm are respectively 58 cm, 3.8 cm, and 1.6 cm. In this comparison, the garment used is impermeable, thus, the air permeability used in the model is 0.005 m/s or less than that due to model limitation. As mentioned before, when there is no wind condition, the air speed

used in the model is 0.01 m/s or less than that. For the static activity, no oscillation is considered; thus, there is no change in air flow rate with respect to time. For the walking condition, oscillation of the clothed arm occurs; thus the simplified model needs the oscillating frequency, and the oscillating amplitude as inputs. The walking speed used in the experiment (1.25 m/s) corresponds to a frequency of about 80 *rpm* and a normal angle of oscillation $\phi_{max}=20^\circ$. Another important input is the aperture configuration; in this section, the clothed arm is always opened because the garment is impermeable (closing the impermeable garment prevents air to enter and ventilate the human body).

Fig. 45 shows the comparison between the simplified model and the experiment ventilation rates at different conditions: walking with wind, walking without wind, and wind without walking. It is shown that all the predicted ventilation rates fall within the standard deviation range with a mean relative error of 6 %. The condition of walking with wind presents the maximum ventilation (2.9 l/min) compared to other conditions. It is clear that walking in the direction of the wind will increase the relative wind velocity which, in its turn, increases the pressure outside and induces more air to enter through the opening. Wind without walking condition comes in the second place with a ventilation rate of 2.2 l/min exceeding that of walking without wind condition (1.6 l/min) at approximately the same speed. This can be justified by the fact that when the oscillation of the arm is in the direction of the walking condition, the relative wind increases but the air layer gap decreases affecting the ventilation rate oppositely.

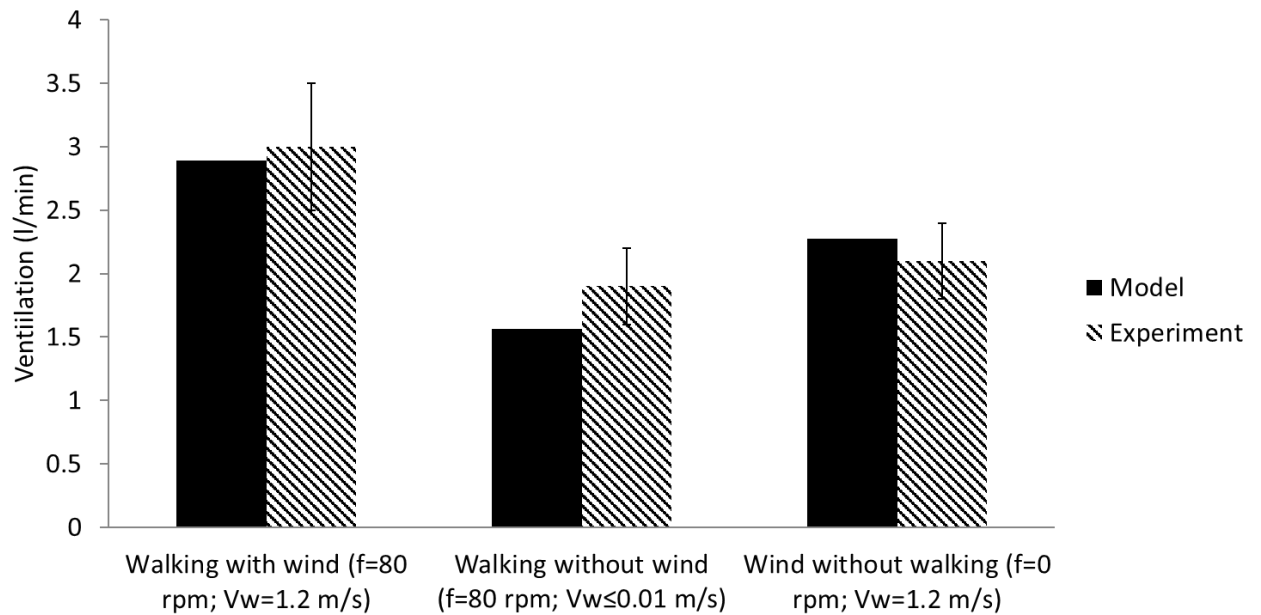


Figure 45: Comparison between the ventilation obtained by the simplified model and a published experiment for the impermeable clothed arm at different conditions (walking with wind, walking without wind and wind without walking).

Case of permeable clothing

In this section, two published experiments are involved. The first experiment adopted is that of Ke et al. [66] that measures the local ventilation rates of the arm for different wind speed at no walking condition (0 rpm). The second experiment adopted is that of Ghaddar et al. [70] that measures the local ventilation rates of the arm for different wind speed at different oscillation frequencies (40-80 rpm). The combination of these two published experiments is achieved in the reason of studying the variation of the ventilation rates at different oscillating frequency (0-80 rpm). Therefore, the air permeability of the clothing must be the same in both experiment (0.05 m/s), as well as the wind velocity (0-1m/s).

The simplified model of the clothed arm subjected to oscillating motion and wind is thoroughly described where the analogy with electric circuit is adopted. The inputs to the oscillating arm model are the air permeability of the fabric (0.05 m/s), the wind speed (0-1 m/s), the aperture configuration (opened and closed), the oscillating frequency (0-80 rpm), and the oscillating amplitude ($\phi_{max}=20^\circ$). As mentioned before, at no wind condition, the speed used in the model is 0.01 m/s or less than that. For the static activity (0 rpm), no oscillation is considered; thus, there is no change in air flow rate with respect to time and vice versa. Finally, the opening aperture induces a certain flow rate and vice versa.

Fig. 46 illustrates the results of the ventilation rates through a permeable clothed limb ($\alpha=0.05$ m/s) for different frequencies and wind velocity and shows that all the simplified

ventilation results fall in the standard deviation range of the experimental results with a maximum relative error of 18%. It is of interest to mention that the relative error provided by the detailed model of Ghaddar et al. [70] was about 7%. Thus, although the model developed is simplified, however, the relative error is acceptable.

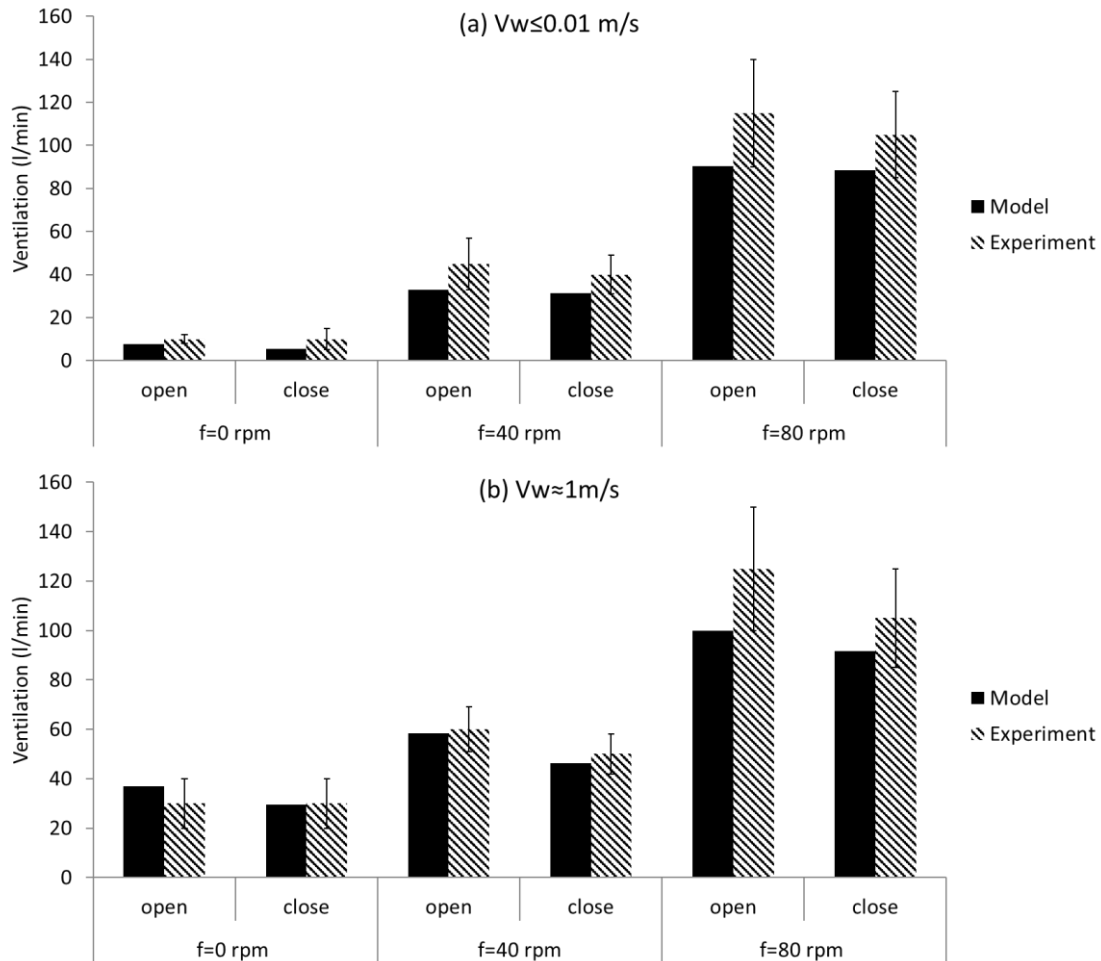


Figure 46: Comparison between the ventilation obtained by the simplified model and the published experiments for the permeable clothed arm at different frequencies and aperture geometries for (a) no wind speed and (b) 1 m/s wind speed.

It is obvious that the maximum ventilation rate is attained in the case of high frequency oscillation (80 rpm) and high wind velocity for both opened (100 l/min) and closed apertures (91.4 l/min). The minimum ventilation rate is achieved for no-frequency and no wind speed (5 l/min) in the case of closed aperture. The reason is clearly that air cannot be exchanged because the opening is closed and the zero wind velocity is unable to create a significant pressure difference between the outside and the microclimate air layer that induces a flow

through the permeable fabric. Another important remark is that increasing the oscillation frequency has major effect for small wind speed rather than large wind speed. In fact, when the frequency doubles from 0 to 40 rpm, the ventilation triples in both open and close apertures for the no-wind speed case, however; it only doubles at larger wind speed ($V_w = 1$ m/s). This is related to the relative wind speed profile that shows that its variation with frequency attains its maximum at small wind speed. On the other hand, it is of interest to investigate the importance of opening aperture at difference conditions. It is shown that the opening increases the ventilation rates of 25 % at a frequency of 40 rpm, while this increase decreases to 13 % at a frequency of 80 rpm (for wind condition). This means that when the frequency increases significantly, the opening role in increasing the ventilation is reduced. This could be related to the time of pumping air through the opening in oscillating condition. Indeed, as the frequency increases, the time of oscillation decreases, and so that air does not have enough time to enter through the openings. Finally, it is worth to mention that in still air, the oscillation induces a significant ventilation rate that increases with the oscillation frequency to be comparable to the case of wind existence at high frequency. Therefore, walking condition at high frequency could induce a significant ventilation rate in still air. However, this statement does not mean that walking in still air could bring thermal comfort because of the induced ventilation. The reason is that in walking condition, the metabolic rate is higher, thus, a significant skin heat losses are needed to ensure thermal comfort. If the ventilation rate induced by the walking conditions is sufficient to relief heat from the skin, the human body could sense a thermal comfort in still air.

iii. Overall Ventilation through permeable coverall

In this section, the overall ventilation rate is validated using the published experiment of Ueda et al. [100]. The simplified model of the clothed trunk and clothed arm are both needed to calculate the overall ventilation rate. The ventilation rate of the clothed legs is estimated based on the same strategy of the clothed trunk because the no-touch phase is negligible in the case of clothed legs. The air resistance of the coverall investigated (0.3 KPa.s/m) which is equivalent to an air permeability of 0.415 m/s at the standard pressure ΔP_m (124.5 Pa). The inputs to the oscillating arm model are the air permeability of the fabric (0.415 m/s), the wind speed (0-1 m/s), the aperture configuration (opened and closed), the oscillating frequency corresponding to a walking speed of 1 m/s (65 rpm), the oscillating amplitude ($\phi_{max}=20^\circ$), and the geometrical dimensions (the height, radius, and air gap of the clothed arm are respectively 58 cm, 3.8 cm, and 1.6 cm). The inputs to the oscillating trunk model

are the air permeability of the fabric (0.415 m/s), the wind speed (0-1 m/s), the aperture configuration (opened and closed), the walking speed (1 m/s), and the geometrical dimensions (the height, radius, and air gap of the clothed trunk are respectively 65 cm, 14 cm, and 5 cm). Same inputs of the trunk model are used to the clothed legs except for the geometrical dimensions (the height, radius, and air gap of the clothed legs are respectively 85 cm, 7 cm, and 4 cm). Finally, the experimental ventilation is given in air exchange rate per minute (min^{-1}), therefore, all the predicted ventilations are divided by the microclimate air layer volume (63 liters).

The results of the comparison between the published experiment and the simplified model are shown in table 13. Examining data presented in table 1, it is clear that all the predicted ventilations almost fall on the range of the standard deviation with a maximum relative error of 14 %. This could be related to the fact that the experiment is achieved without closing the connection between the trunk and the arm while the model took each clothed segment independently. Therefore, the discrepancy between the experiment and the model could be compensated in taking into account the inter-connection between the trunk and the arm (in further study) as done by Ismail et al. (2016a and 2016b).

Table 13: Overall air exchange rate (min^{-1}) for a permeable coverall ($\alpha=0.415$ m/s)

		Closed Aperture			Opened aperture		
		Model		Experiment	Model		Experiment
Still air ($V_w \leq 0.01$ m/s)	Standing	Left and right arm	0.5	2.8±0.2	Left and right arm	0.56	3±0.3
		Trunk	1.3		Trunk	1.4	
		Left and right legs	1.2		Left and right legs	1.2	
		Total	3		Total	3.16	
	Walking at $V_{walk} = 1$ m/s	Left and right arm	0.66	5.3±0.3	Left and right arm	0.868	5.6±0.1
		Trunk	2.48		Trunk	2.97	
		Left and right legs	1.71		Left and right legs	1.71	
		Total	4.85		Total	5.55	

		Total	4.85		Total	4.814	
Wind condition ($V_w = 1$ m/s)	Standing	Left and right arm	0.69	4.2±0.3	Left and right arm	0.998	4.9±0.5
		Trunk	2.48		Trunk	2.97	
		Left and right legs	1.71		Left and right legs	1.71	
		Total	4.88		Total	5.678	
	Walking at $V_{walk} = 1$ m/s	Left and right arm	1.16	6.3±0.3	Left and right arm	1.32	6.6±0.3
		Trunk	2.73		Trunk	2.89	
		Left and right legs	2.7		Left and right legs	2.7	
		Total	6.59		Total	6.91	

2. Inter-connected clothed segment

The thermal manikin was run using the constant skin temperature of 34°C. The ambient temperature of the environmental chamber is 25.5 °C ± 0.2 °C while the relative humidity was about 60 ± 3 %. The experiments were repeated at different conditions of wind speeds ($V_w < 0.11$ m/s, $V_w = 1$ m/s and $V_w = 1.2$ m/s). Furthermore, different walking speeds are investigated: no walking ($V_{walk} = 0$ m/s); walking at 0.8 m/s corresponding to a DSPM of 38 and a frequency of about 50 rpm; walking at 1.25 m/s corresponding to a DSPM of 60 and a frequency of about 80 rpm. The inputs to the integrated simplified model are the clothing air permeability, the geometrical parameters of the clothed arm and trunk, the oscillation parameters for the arm, the walking speed for the trunk, the ambient temperature and wind speeds. In the integrated simplified model, the height, radius, and air gap of eight zones are presented in **Table 14**.

Table 14: The geometrical inputs of the air gap

	LF/LB	UF/UB	TF/TB	SF/SB
Y (cm)	0.5	0.8	4	4
R (cm)	3	5	12	17
H (cm)	30	25	40	10

The oscillating parameters depend on the walking speed at a typical angle of oscillation $\phi_{\max} = 20^\circ$ [73]. In this section, the results of the integrated model should be compared with the experimental results. The experimental results are given for the arm and the trunk, however; the results of the simplified model are given for each zone separately which necessitates further calculation. In the case of non-oscillating arm, the problem is steady state so that the microclimate ventilation of the arm is the sum of the lower arm, upper arm and a portion of the shoulder ventilations:

$$Q_{arm} = \max(Q_{r,LF}, 0) + \max(Q_{x,LF}, 0) + \max(Q_{r,LB}, 0) + \max(Q_{x,LB}, 0) + \max(Q_{r,UF}, 0) + \max(Q_{r,UB}, 0) + \frac{r_{UF}}{r_{SF}} (\max(Q_{r,SF}, 0) + \max(Q_{r,SB}, 0) + \max(Q_{x,SF}, 0) + \max(Q_{x,SB}, 0))$$

(52 a)

where $Q_{r,LF}$ and $Q_{x,LF}$ are respectively the volumetric flow rate of air through clothing and through openings for the lower arm front zone; $Q_{r,LB}$ and $Q_{x,LB}$ are respectively the volumetric flow rate of air through clothing and through openings for the lower arm back zone; $Q_{r,UF}$ and $Q_{r,UB}$ are respectively the volumetric flow rate of air through clothing for the upper front and back arm zones; $Q_{r,SF}$ and $Q_{r,SB}$ are respectively the volumetric flow rate of air through clothing for the shoulder front and back zones; $\frac{r_{UF}}{r_{SF}}$ is the ratio of the upper arm radius to shoulder radius, this ratio is used as an estimation of the portion of the shoulder ventilation that is used for the estimation of the arm ventilation. The maximum is used because the air ventilation is estimated as the positive penetrating flow rates either through clothing or through openings.

However, when the arm is oscillating during walking condition, the problem becomes steady-periodic and the segmental ventilation rate is obtained by integrating the penetrating mass flow rate of equation (12 a) through clothing or through openings over one period T . On the other hand, the microclimate ventilation of the trunk is the sum of the trunk front and back zones as well as a portion of the shoulder ventilations:

$$Q_{trunk} = \max(Q_{r,TF}, 0) + \max(Q_{r,TB}, 0) + \frac{r_{TF}}{r_{SF}} (\max(Q_{r,SF}, 0) + \max(Q_{r,SB}, 0) + \max(Q_{x,SF}, 0) + \max(Q_{x,SB}, 0))$$

(52b)

Figure 47 shows the measured and predicted segmental ventilation rates at different conditions. Figure 47(a) shows the comparison between the predicted and the experimental arm ventilation while Figure 47(b) shows the comparison between the predicted and the experimental trunk ventilation. Figure 47 (c) shows the comparison between the predicted and the experimental inter-segmental ventilation. Good agreement is illustrated between the experimental and predicted ventilation rates with a maximum relative error of 16% and an average relative error of 13%. As mentioned in the tracer gas method description, the ventilation rates of the arm, trunk and the inter-segmental ventilation are estimated based on the Ar concentration. The results show that the inter-segmental ventilation is flowing from the trunk to the arm. Furthermore, the inter-segmental ventilation increases with the increase of the relative wind speed and constitutes about 30 % of the arm ventilation and 14 % of the trunk ventilation. The maximum inter-segmental ventilation is achieved when walking in windy condition. This is because both wind and walking increases the relative speed. Increasing the relative speed leads to an increase in the pressure difference between the microclimate air layer and the environment. This phenomenon will induce more air to penetrate through clothing and will lead to an increase of the segmental ventilation. Increasing the segmental ventilation will result, at its turn, to an increase of the inter-segmental ventilation.

Table 15 presents the segmental heat losses for the arm and trunk. Good agreement is seen between the segmental heat losses recorded experimentally by the thermal manikin at constant skin and environmental temperatures of 34 °C and 25.5 °C respectively and the predicted values from the coupled ventilation and thermal network model with a maximum relative error of 8 %. The segmental heat losses for the arm and the trunk attain its minimum for the lowest relative velocity and its maximum for the highest relative velocity. Evidently, when the relative velocity increases, the trunk and arm ventilation increase leading to an increase in segmental heat losses. The main reason is that the penetrated air is coming from an ambient temperature of 25 °C. It is slightly heated in the fabric nodes and enter to the microclimate air layer leading to significant heat losses from the skin set at a constant temperature of 34 °C.

3. Limitations and recommendations

The current model is used to track the penetrating air through clothing and opening apertures in order to accurately measure the segmental and inter-segmental ventilation. The novelty of this model arises from two facts (i) first, estimating the inter-segmental ventilation was restricted to sedentary conditions, (ii) second, accounting for inter-segmental ventilation will add more complexity to the mathematical model; therefore, the simplicity associated with the electric circuit analogy is highly needed. Measuring the inter-segmental ventilation is useful because it leads to accurate estimation of the segmental ventilation which, in its turn, leads to accurate measure of segmental heat losses of the upper human body which is the most influencing part on local and total thermal comfort. Furthermore, inter-segmental ventilation is beneficial in getting rid of the sweat accumulated in the Axilla zone as well as in knowing the contaminant distribution and deposition on the skin.

The model succeeds in predicting the segmental and inter-segmental ventilation as well as the segmental heat losses for the common range of walking and wind speeds. Nevertheless, the simplicity associated with the electric circuit analogy presents some limitations: the model is not sensitive for low air permeability, and low relative wind. When the air permeability $\alpha < 0.2$ m/s, the relative wind speed must be significant ($V_r \geq 0.2$ m/s). At lower air permeability, the correlation developed by Ismail et al. [103] could be used. As a matter of validation, the previous model of Ismail et al. [103] states that the inter-segmental ventilation consists about 30 % of the arm ventilation and 14 % of the trunk ventilation. The simplified model comes up approximately the same results. Therefore, it is recommended to measure the segmental ventilation of the arm and trunk using independent clothed segment and predict the inter-segmental ventilation as 30 % percent of the trunk ventilation. If it is found to be significant, the simplified model taking into account the inter-connection is used and accurate value of the segmental ventilation and heat losses are obtained.

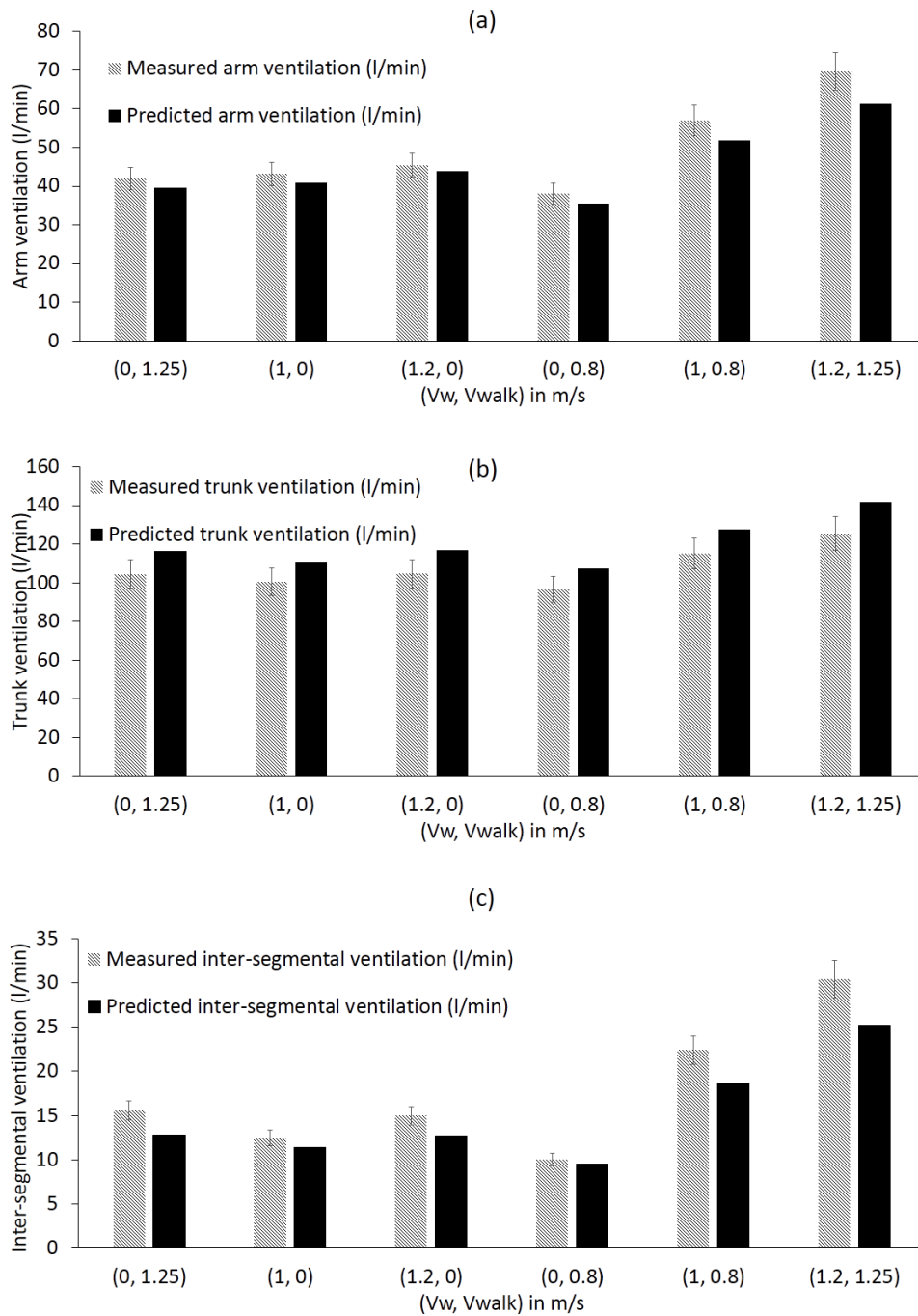


Figure 47: Comparison between the measured and predicted ventilation rate of the (a) clothed arm (b) clothed trunk and (c) inter-segmental ventilation

Table 15: Comparison between the measured and predicted heat losses

Conditions		Arm heat losses (w/m^2)		Trunk heat losses (w/m^2)	
V_w (m/s)	V_{walk} (m/s)	Experiment	Model	Experiment	Model

0	1.25	61.8 ± 3	61.3	62.96	65.71
1	0	61.22 ± 3	60.91	62.07	64.28
1.2	0	65.28 ± 3	61.24	63.54	65.72
0	0.8	59.77 ± 3	58.07	60.12	60.63
1	0.8	75.02 ± 3	72.72	70.82	73.11
1.2	1.25	79.53 ± 3	78.02	75.91	77.94

4. Incorporating the natural convection effect in the estimation of ventilation and heat losses for independent clothed segment

a. Model validation with experiment

The thermal manikin was run using the constant skin temperature of 34°C. The ambient temperature of the environmental chamber is 25.5 °C ± 0.2 °C for the natural convection experiment and 34°C for the non-natural convection experiment. The relative humidity was about 60 ± 3 %. The experiments were repeated at different conditions of wind and walking speeds. For instance, the wind speeds were changed from non-windy condition ($V_w < 0.11$ m/s) to a windy condition of 1 m/s; moreover, the experiment investigated different body postures: standing and walking at 1.25 m/s corresponding to a DSPM of 60. The inputs to the integrated simplified model are the clothing air permeability, the geometrical parameters of the clothed arm, and the oscillation parameters. In the integrated simplified model, the height, radius, and air gap of the clothed arm are respectively 58 cm, 3.8 cm, and 1.6 cm. The clothed arm end is opened at the bottom. The walking speed (1.25 m/s) used in the experiment corresponded to a frequency of about 80 rpm and a typical angle of oscillation $\phi_{\max} = 20^\circ$.

Fig. 48 shows the measured and predicted segmental ventilation rates at different conditions: (i) no wind and no walking conditions (ii) wind (1 m/s) without walking condition (iii) walking (60 DSPM or 1.25 m/s) without wind (iv) wind (1 m/s) and walking (60 DSPM or

1.25 m/s). Good agreement is illustrated between the experimental and predicted ventilation rates with a maximum relative error of 10%. By comparing the results of Fig. 48 (a) and 48 (b), it is clear that the incorporation of natural convection effect led to an increase of segmental ventilation in all conditions. This is evidently related to the fact that the natural convection will lift the air upwards, increasing the penetrating air through clothing or openings in order to conserve the mass. This was also found by Chaves et al. [87] who reported that the natural convection improved the forced convection inside the open cavity. In addition, the validated results show that the effect of natural convection is maximum (13 %) in the case of no wind, no walking conditions. The main reason is that the natural convection overcomes the forced convection phenomena when wind and walking are significantly low. In fact, the presence of openings allows the air to be lifted by the buoyancy force so that the segmental ventilation is enhanced. When only windy condition is considered, the effect of natural convection decreases (6% at $V_w=1\text{m/s}$); this is evidently related to the increase in the segmental ventilation due to forced convection. Similarly, when only walking condition is considered, the effect of natural convection decreases also (6% at $V_{walk}=1.25\text{ m/s}$) for the same reason. When both wind and walking conditions are considered, the effect of natural convection decreases to the minimum (about 5 % for $V_w=1\text{m/s}$, $V_{walk}=1.25\text{ m/s}$). Indeed, the combined wind and walking condition increases the relative wind speed that, in its turn, increases the effect of forced convection to overcome the natural convection effect.

Table 16 presents the segmental heat losses for the arm. Good agreement is seen between the segmental heat losses given by the thermal manikin at constant skin temperature of 34°C and the integrated ventilation and thermal network model with a maximum relative error of 8 %. The segmental heat losses of the oscillating arm in no wind condition are greater by about 14% compared to the sedentary case (no wind, no walking) and almost equal to the

case of wind condition (1 m/s) without walking. The main reason is that the swinging motion of the clothed arm brings the air to penetrate (pumping effect) and leave because of the change in the microclimate air layer size. This flow of air raises the ventilation rate through clothing and through openings. Increasing the ventilation rate decreases the microclimate air temperature and destructs the dynamic resistance of the clothing leading to an increase in the segmental heat losses. Finally, it is shown that walking in windy condition presents the maximum segmental heat losses compared to all other cases. The main reason is clearly the maximum ventilation rate induced when both wind and walking conditions are presented.

Table 16: Segmental heat losses of the arm at different body postures

		Segmental heat losses (W/m ²)	
		Model	Experiment
Still air	Standing	58.32	54.7 ± 3
	Walking	66.78	61.9 ± 3
Wind condition	Standing	64.12	61.4 ± 3
	Walking	75.61	77.1 ± 3

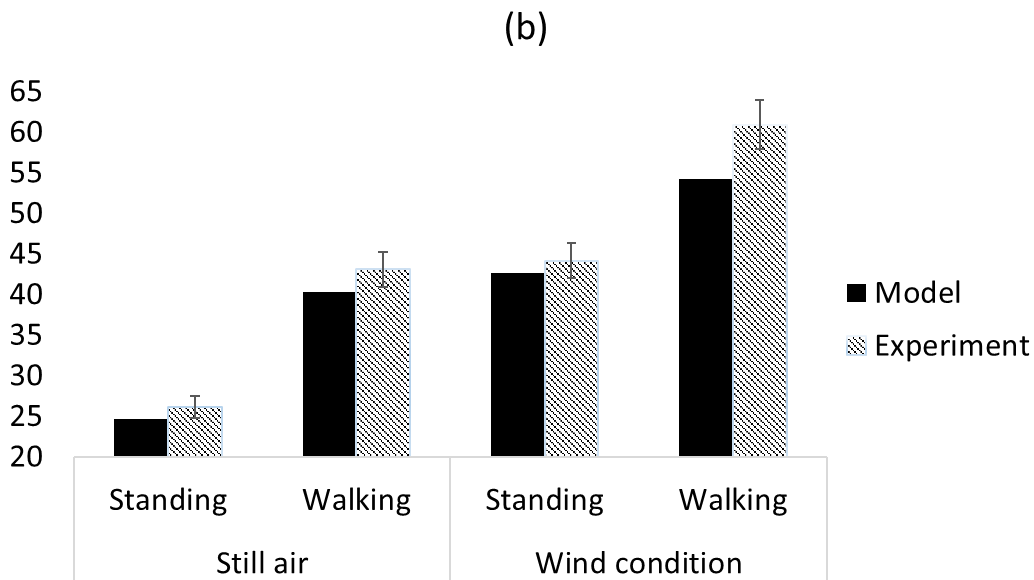
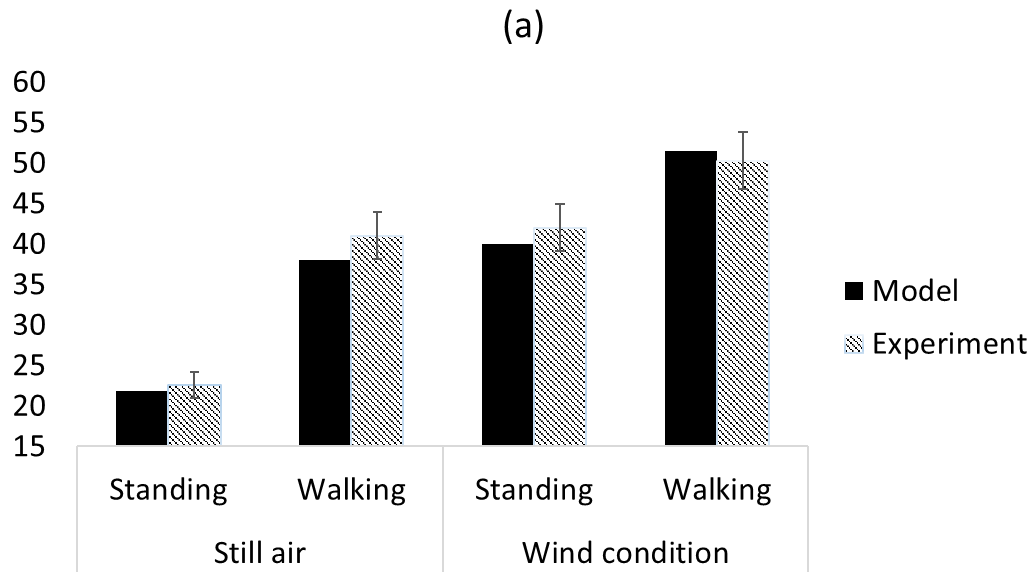


Figure 48: Comparison between measured and predicted segmental ventilation rate of clothed arm (a) without natural convection ($T_{env} = 34^{\circ}\text{C}$, $T_{skin} = 34^{\circ}\text{C}$) and (b) with natural convection effect ($T_{env} = 25.5^{\circ}\text{C}$, $T_{skin} = 34^{\circ}\text{C}$)

In order to insure the validity of the simplified model, it is necessary to test it at different conditions and compare the results with validated published model that take into account the natural convection effect. For instance, the model of Ismail et al. [69] is based on solving the coupled mass, momentum and energy equations inside the microclimate air layer. Its complexity arises from the fact that such model necessitates a high computational cost since

it divides the microclimate region into large number of grid nodes in axial and angular directions. Therefore, if good agreement occurs between the arm ventilation results of the complicated and simplified circuit model, then the validity of such model is established. Table 17 shows the comparison between the current circuit model and the published 2-D model ventilation results at environment temperature of 20 °C [69] at different wind and permeability. Good agreement was found with a maximum relative error of less than 10% and an average relative error of 5%.

Table 17: Comparison between the clothed arm ventilation results

Condition	Published model ventilation rate (<i>l/m</i>) [31]	Current simplified model ventilation rate (<i>l/m</i>)
$V_w=0.6\text{m/s}; \alpha=0.135\text{ m/s}$	13.53	13.3
$V_w=0.9\text{ m/s}; \alpha=0.135\text{ m/s}$	12.63	13.1
$V_w=1.2\text{ m/s}; \alpha=0.135\text{ m/s}$	17.34	15.7
$V_w=1\text{ m/s}; \alpha=0.05\text{ m/s}$	8.32	8.01
$V_w=1\text{m/s}; \alpha=0.09\text{ m/s}$	11.38	12.16
$V_w=1\text{m/s}; \alpha=0.135\text{ m/s}$	13.58	14.1

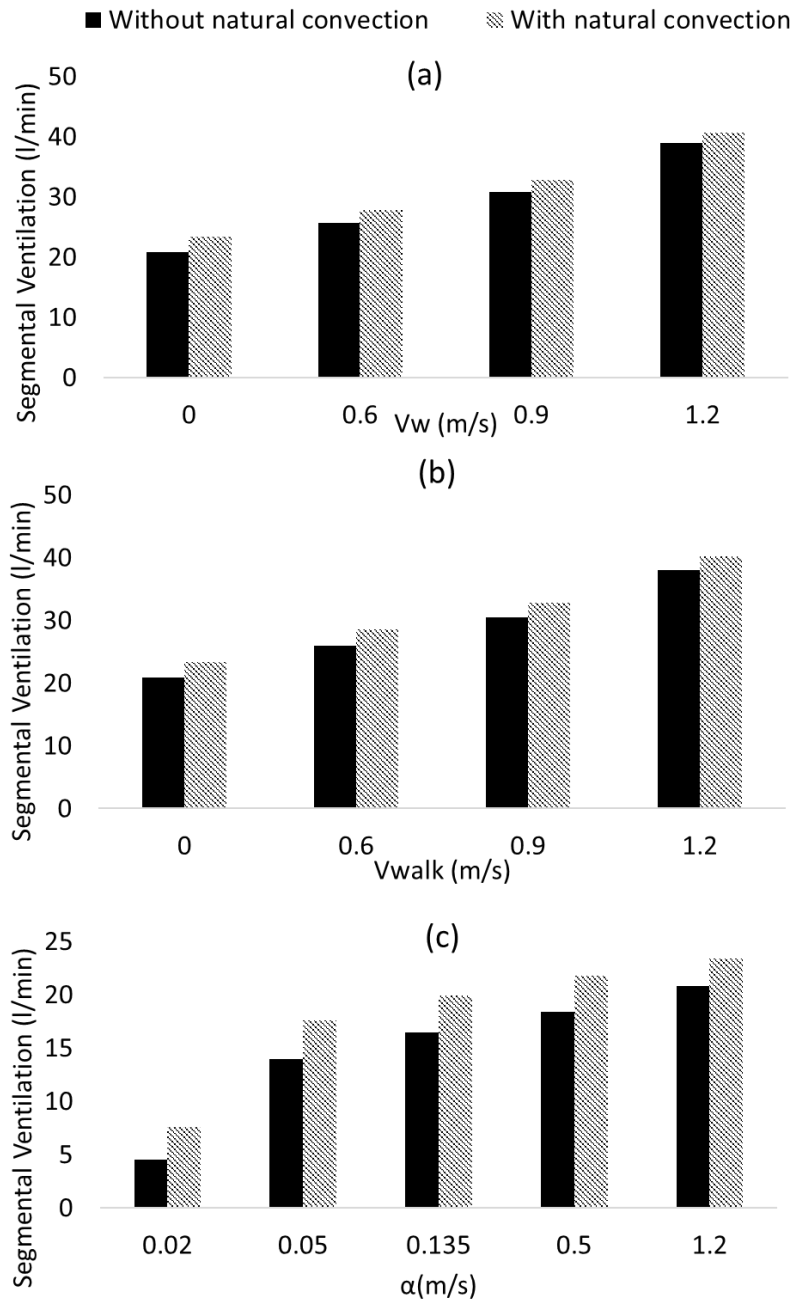


Figure 49: Ventilation rate of the clothed arm segment for different (a) wind speeds (b) walking speeds (c) air permeability ($T_{env} = 25.5^\circ\text{C}$, $T_{skin} = 34^\circ\text{C}$)

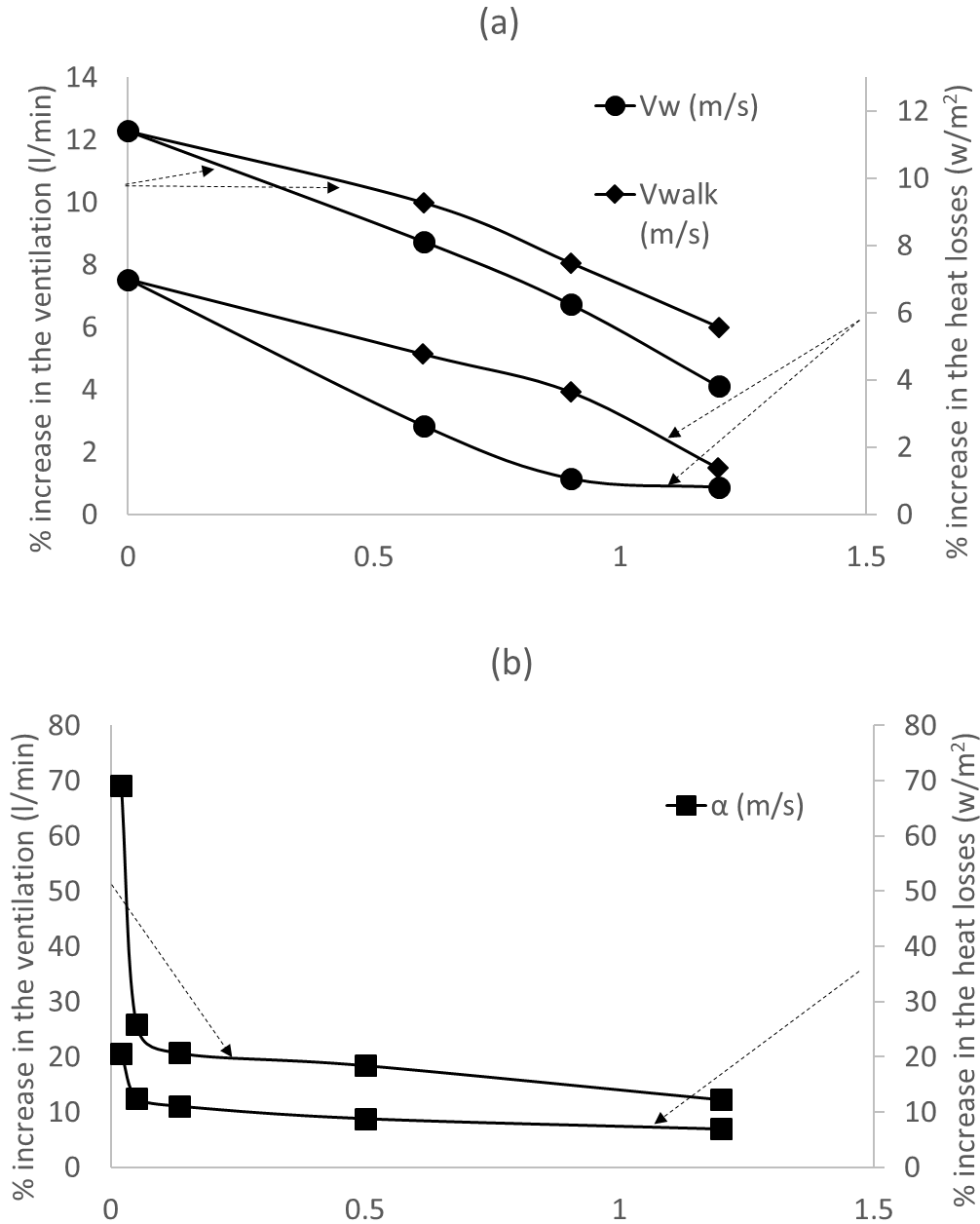


Figure 50: Percentage increase in ventilation rate and heat losses of clothed arm when the natural convection is included for (a) different wind and walking speed (b) air permeability ($T_{env} = 25.5^\circ\text{C}$, $T_{skin} = 34^\circ\text{C}$)

b. Parametric study

In order to examine the effect of natural convection on the segmental ventilation and segmental heat losses of the clothed arm, a parametric study at different conditions is performed. This parametric study is based on estimating the segmental ventilation and heat losses of the clothed arm with and without natural convection and determining the increase

in the rate of segmental ventilation when the natural convection is accounted for. The estimation of the segmental ventilation and heat losses without natural convection is achieved by canceling the electro-motive force e . The coupling with the thermal resistance is realized using a single iteration because there's no need to update for the temperature in the ventilation model. It is noteworthy that the default case is $V_w < 0.11$ m/s, $V_{walk} = 0$ m/s, $\alpha = 1.2$ m/s for environmental temperature of 25 °C.

Fig. 49 and Table 18 show respectively the predicted ventilation rate and heat losses of the clothed arm segment with and without natural convection for different (a) wind speeds (b) walking speeds (c) air permeability at $T_{env} = 25.5^\circ\text{C}$ and $T_{skin} = 34^\circ\text{C}$. In order to clearly see the effect of natural convection at different conditions, the percentage increases in the segmental ventilation and heat losses when including natural convection in the model compared to the case without incorporating natural convection are shown in Fig. 50. It is clear that natural convection effect is more significant in enhancing ventilation and heat losses in the case of walking than in the case of windy condition (Fig. 50 (a)). This is related to the fact that increasing the wind speed increases the penetrating flow rate through clothing to the annulus and hence the forced convection dominates. On the other hand, the increase in walking condition will enhance the pumping effect which results in an increase of mass flow rate that is lifted axially through openings by the natural convection effect. Fig. 50 (b) shows that the maximum increase in the segmental ventilation and heat losses due to the natural convection is when the air permeability of the clothing is relatively small such that the forced convection is neglected. The percentage increase is deteriorated with the increase of air permeability: from 68% in ventilation and 20 % in heat losses at low permeability (0.02 m/s) to 13 % when the air permeability reached 1.2 m/s.

Therefore, it is recommended to take into account the natural convection effect while estimating the segmental ventilation and heat losses when considering relatively small clothing permeability in no-windy and walking conditions

Table 18: Clothed arm segmental heat losses (w/m^2)

		Clothed arm heat losses (w/m^2)	
		Without natural convection	With natural convection
Vw (m/s)	0	53.01	56.71
	0.6	56.94	58.44
	0.9	63.18	63.85
	1.2	64.84	65.36
Vwalk (m/s)	0	53.01	56.71
	0.6	57.1	59.82
	0.9	61.64	63.87
	1.2	65.04	65.94
α (m/s)	0.02	40.3	48.63
	0.05	45.98	51.74
	0.135	47.56	52.84
	0.5	49.67	54.07
	1.2	53.01	56.71

BIBLIOGRAPHY

1. Nunneley, Sarah A. "Heat stress in protective clothing: interactions among physical and physiological factors." *Scandinavian journal of work, environment & health* (1989): 52-57.
2. Ramakrishna, Seeram, Kazutoshi Fujihara, Wee-Eong Teo, Thomas Yong, Zuwei Ma, and Ramakrishna Ramaseshan. "Electrospun nanofibers: solving global issues." *Materials today* 9, no. 3 (2006): 40-50.
3. Lee, K. W., and B. Y. H. Liu. "Theoretical study of aerosol filtration by fibrous filters." *Aerosol Science and Technology* 1, no. 2 (1982): 147-161.
4. Shin, Y. M., et al. "Electrospinning: A whipping fluid jet generates submicron polymer fibers." *Applied physics letters* 78.8 (2001): 1149-1151.
5. Chattopadhyay, Saptarshi, T. Alan Hatton, and Gregory C. Rutledge. "Aerosol filtration using electrospun cellulose acetate fibers." *Journal of Materials Science* 51.1 (2016): 204-217.
6. Kuo, Yu-Ying, Francesca Camilla Bruno, and Jing Wang. "Filtration performance against nanoparticles by electrospun Nylon-6 media containing ultrathin nanofibers." *Aerosol Science and Technology* 48.12 (2014): 1332-1344.
7. Leung, Wallace Woon-Fong, Chi-Ho Hung, and Ping-Tang Yuen. "Effect of face velocity, nanofiber packing density and thickness on filtration performance of filters with nanofibers coated on a substrate." *Separation and purification technology* 71.1 (2010): 30-37.
8. Pai, Chia-Ling, Mary C. Boyce, and Gregory C. Rutledge. "On the importance of fiber curvature to the elastic moduli of electrospun nonwoven fiber meshes." *Polymer* 52.26 (2011): 6126-6133.
9. Abuzade, Ramazan Ali, Ali Zadhoush, and Ali Akbar Gharehaghaji. "Air permeability of electrospun polyacrylonitrile nanoweb." *Journal of Applied Polymer Science* 126.1 (2012): 232-243.
10. Frenot, Audrey, and Ioannis S. Chronakis. "Polymer nanofibers assembled by electrospinning." *Current opinion in colloid & interface science* 8, no. 1 (2003): 64-75.
11. Schreuder-Gibson, Heidi, Phillip Gibson, Kris Senecal, Michael Sennett, John Walker, Walter Yeomans, David ZIEGLER, and Peter P. TSAI. "Protective textile materials based on electrospun nanofibers." *Journal of Advanced Materials* 34, no. 3 (2002): 44-55.

12. Wang, Yu, S. Serrano, and J. J. Santiago-Aviles. "Conductivity measurement of electrospun PAN-based carbon nanofiber." *Journal of materials science letters* 21, no. 13 (2002): 1055-1057.
13. Warner, Steven B., A. Buer, S. C. Ugbohue, G. C. Rutledge, and M. Y. Shin. "A fundamental investigation of the formation and properties of electrospun fibers." *National textile center annual report* (1998): 83-90.
14. Ji, Yuan, Bingquan Li, Shouren Ge, Jonathan C. Sokolov, and Miriam H. Rafailovich. "Structure and nanomechanical characterization of electrospun PS/clay nanocomposite fibers." *Langmuir* 22, no. 3 (2006): 1321-1328.
15. Mohan, A. <http://www.lib.ncsu.edu/resolver/1840.16/1925>, 2003.
16. Shi, Xiaomin, Weiping Zhou, Delong Ma, Qian Ma, Denzel Bridges, Ying Ma, and Anming Hu. "Electrospinning of nanofibers and their applications for energy devices." *Journal of Nanomaterials* 2015 (2015): 122.
17. Rafiei, S., S. Maghsoodloo, B. Noroozi, V. Mottaghitalab, and A. K. Haghi. "Mathematical modeling in electrospinning process of nanofibers: a detailed review." *Cellul Chem Technol* 47 (2013): 323-338.
18. Sarkar, Kamal, Palmira Hoos, and Alberto Urias. "Numerical Simulation of Formation and Distortion of Taylor Cones." *Journal of Nanotechnology in Engineering and Medicine* 3, no. 4 (2012): 041001.
19. Taylor, Geoffrey. "Electrically driven jets." In *Proceedings of the Royal Society of London A: Mathematical, Physical and Engineering Sciences*, vol. 313, no. 1515, pp. 453-475. The Royal Society, 1969. Gupta, P. 2004; Chapter 1, part I, pp. 1-70.
20. Saville, D. A. "Electrohydrodynamics: the Taylor-Melcher leaky dielectric model." *Annual review of fluid mechanics* 29, no. 1 (1997): 27-64.
21. Feng, J. J. "The stretching of an electrified non-Newtonian jet: A model for electrospinning." *Physics of Fluids (1994-present)* 14, no. 11 (2002): 3912-3926.
22. Roozmond, P. C. "A model for electrospinning viscoelastic fluids." *Bachelor Final Project* 576690 (2007).
23. Helgeson, Matthew E., Kristie N. Grammatikos, Joseph M. Deitzel, and Norman J. Wagner. "Theory and kinematic measurements of the mechanics of stable electrospun polymer jets." *Polymer* 49, no. 12 (2008): 2924-2936.
24. Reneker, Darrell H., and Alexander L. Yarin. "Electrospinning jets and polymer nanofibers." *Polymer* 49, no. 10 (2008): 2387-2425.

25. Hohman, Moses M., Michael Shin, Gregory Rutledge, and Michael P. Brenner. "Electrospinning and electrically forced jets. I. Stability theory." *Physics of Fluids* (1994-present) 13, no. 8 (2001): 2201-2220.
26. Yarin, A. L. "Coaxial electrospinning and emulsion electrospinning of core-shell fibers." *Polymers for Advanced Technologies* 22, no. 3 (2011): 310-317.
27. Reneker, Darrell H., Alexander L. Yarin, Hao Fong, and Sureeporn Koombhongse. "Bending instability of electrically charged liquid jets of polymer solutions in electrospinning." *Journal of Applied physics* 87, no. 9 (2000): 4531-4547.
28. Gadkari, Siddharth B. "Scaling analysis for electrospinning." *SpringerPlus* 3, no. 1 (2014): 1-7.
29. Fridrikh, Sergey V., H. Yu Jian, Michael P. Brenner, and Gregory C. Rutledge. "Controlling the fiber diameter during electrospinning." *Physical review letters* 90, no. 14 (2003): 144502.
30. Subbotin, A., R. Stepanyan, A. Chiche, J. J. M. Slot, and G. Ten Brinke. "Dynamics of an electrically charged polymer jet." *Physics of Fluids* (1994-present) 25, no. 10 (2013): 103101.
31. Moses, H., R. Gregory, and P. Michael. "Electrospinning and electrically forced jets. II. Applications." *Physics of Fluids* 13, no. 8 (2001).
32. Carroll, Colman P., and Yong Lak Joo. "Electrospinning of viscoelastic Boger fluids: Modeling and experiments." *Physics of Fluids* (1994-present) 18, no. 5 (2006): 053102.
33. He, Ji-Huan, Yu-Qin Wan, and Jian-Yong Yu. "Scaling law in electrospinning: relationship between electric current and solution flow rate." *Polymer* 46, no. 8 (2005): 2799-2801.
34. Bhattacharjee, P. K., Tobias M. Schneider, M. P. Brenner, G. H. McKinley, and G. C. Rutledge. "On the measured current in electrospinning." (2010).
35. Hinch E. <https://www.who.edu/fileserver.do?id=28326&pt=10&p=17274>.
36. He, Ji-Huan, Yue Wu, and Wei-Wei Zuo. "Critical length of straight jet in electrospinning." *Polymer* 46, no. 26 (2005): 12637-12640.
37. Gomes, Demetrius S., Ana NR da Silva, Nilton I. Morimoto, Luiz TF Mendes, Rogerio Furlan, and Idalia Ramos. "Characterization of an electrospinning process using different PAN/DMF concentrations." *Polímeros* 17, no. 3 (2007): 206-211.

38. Barua, Bipul, and Mrinal C. Saha. "Investigation on jet stability, fiber diameter, and tensile properties of electrospun polyacrylonitrile nanofibrous yarns." *Journal of Applied Polymer Science* 132, no. 18 (2015).
39. Subbiah, Thandavamoorthy, G. S. Bhat, R. W. Tock, S. Parameswaran, and S. S. Ramkumar. "Electrospinning of nanofibers." *Journal of Applied Polymer Science* 96, no. 2 (2005): 557-569.
40. Zargham, Shamim, Saeed Bazgir, Amir Tavakoli, Abo Saied Rashidi, and Rogheih Damerchely. "The effect of flow rate on morphology and deposition area of electrospun nylon 6 nanofiber." *J Eng Fibers Fabr* 7, no. 4 (2012): 42-9.
41. Thompson, C. J., George G. Chase, A. L. Yarin, and D. H. Reneker. "Effects of parameters on nanofiber diameter determined from electrospinning model." *Polyme*
42. Zeng YO, Pei ZE, Wang XI. "Numerical Simulation of Whipping Process in Electrospinning." In *WSEAS International Conference. Proceedings. Mathematics and Computers in Science and Engineering*, edited by Shengyong Chen, no. 8. World Scientific and Engineering Academy and Society, 2009.
43. Stepanyan, R., A. V. Subbotin, L. Cuperus, P. Boonen, M. Dorschu, F. Oosterlinck, and M. J. H. Bulters. "Nanofiber diameter in electrospinning of polymer solutions: Model and experiment." *Polymer* (2016).
44. Sutasinpromprae, Juthawan, Sujinda Jitjaicham, Manit Nithitanakul, Chidchanok Meechaisue, and Pitt Supaphol. "Preparation and characterization of ultrafine electrospun polyacrylonitrile fibers and their subsequent pyrolysis to carbon fibers." *Polymer International* 55, no. 8 (2006): 825-833.
45. Lowery, Joseph Lenning. *Characterization and modification of porosity in electrospun polymeric materials for tissue engineering applications*. Diss. Massachusetts Institute of Technology, 2009.
46. Hosseini, S. A., and H. Vahedi Tafreshi. "Modeling permeability of 3-D nanofiber media in slip flow regime." *Chemical Engineering Science* 65.6 (2010): 2249-2254.
47. Kirsh, At A., I. B. Stechkina, and N. A. Fuchs. "Efficiency of aerosol filters made of ultrafine polydisperse fibres." *Journal of Aerosol Science* 6, no. 2 (1975): 119-124.
48. Fang, Jian, Xungai Wang, and Tong Lin. *Functional applications of electrospun nanofibers*. InTech–Open Access Publisher, 2011.

49. Sundarrajan, Subramanian, Kwong Luck Tan, Soon Huat Lim, and Seeram Ramakrishna. "Electrospun nanofibers for air filtration applications." *Procedia Engineering* 75 (2014): 159-163
50. Wang, Jing, Seong Chan Kim, and David YH Pui. "Investigation of the figure of merit for filters with a single nanofiber layer on a substrate." *Journal of Aerosol Science* 39.4 (2008): 323-334.
51. Jing Wang , Seong Chan Kim & David Y. H. Pui (2008) Figure of Merit of Composite Filters with Micrometer and Nanometer Fibers, *Aerosol Science and Technology*, 42:9, 722-728, DOI: 10.1080/02786820802249133
52. Haines, Andy, et al. "Climate change and human health: impacts, vulnerability and public health." *Public health* 120.7 (2006): 585-596.
53. Barhate, R. S., and Seeram Ramakrishna. "Nanofibrous filtering media: filtration problems and solutions from tiny materials." *Journal of membrane science* 296.1 (2007): 1-8.
54. Lee, Seungsin, and S. Kay Obendorf. "Use of electrospun nanofiber web for protective textile materials as barriers to liquid penetration." *Textile Research Journal* 77.9 (2007): 696-702.
55. Huang, Zheng-Ming, et al. "A review on polymer nanofibers by electrospinning and their applications in nanocomposites." *Composites science and technology* 63.15 (2003): 2223-2253.
56. Kwankhao, B. *Microfiltration Membranes via Electrospinning of Polyethersulfone Solutions*, Thesis submitted to the Department of Chemistry of University of Duisburg-Essen, pp. 35, 2013.
57. Kim, Jung Hyeun, George W. Mulholland, Scott R. Kukuck, and David YH Pui. "Slip correction measurements of certified PSL nanoparticles using a nanometer differential mobility analyzer (nano-DMA) for Knudsen number from 0.5 to 83." *Journal of Research of the National Institute of Standards and technology* 110, no. 1 (2005): 31.
58. Hill, Michael A., Terence A. Ghee, Jonathan Kaufman, and Suresh Dhaniyala. "Investigation of aerosol penetration through individual protective equipment in elevated wind conditions." *Aerosol Science and Technology* 47, no. 7 (2013): 705-713.
59. Boppa, Venugopal. "Characterization of Structure and Tensile Properties of Electrospun Web." (2009).

60. Choi, J., Yang, B.J., Bae, G.N. and Jung, J.H., 2015. Herbal Extract Incorporated Nanofiber Fabricated by an Electrospinning Technique and its Application to Antimicrobial Air Filtration. *ACS applied materials & interfaces*, 7(45), pp.25313-25320.
61. Hsiao, Hung-Yi, Chao-Ming Huang, Yi-Yu Liu, Yu-Cheng Kuo, and Hui Chen. "Effect of air blowing on the morphology and nanofiber properties of blowing-assisted electrospun polycarbonates." *Journal of Applied Polymer Science* 124, no. 6 (2012): 4904-4914.
62. Givehchi, Raheleh, Qinghai Li, and Zhongchao Tan. "Quality factors of PVA nanofibrous filters for airborne particles in the size range of 10–125nm." *Fuel*(2015).
63. Faccini, M., C. Vaquero, and D. Amantia. "Development of protective clothing against nanoparticle based on electrospun nanofibers." *Journal of Nanomaterials* 2012 (2012): 18.
64. Ke Y., Li J. and Havenith G. An improved experimental method for local clothing ventilation measurement. *International Journal of Industrial Ergonomics* 2014; 44: 75-81.
65. Bouskill L., Havenith G., Kuklane K., Parsons K. and Withey W. Relationship between clothing ventilation and thermal insulation. *AIHA J.* 2002; 63:262-268.
66. Ke Y., Havenith G., Li J. and Li X. A New experimental study of influence of fabric permeability, clothing sizes, openings and wind on regional ventilation rates. *Fibers and Polymers* 2013; 14:1906-1911.
67. Havenith G., Zhang P., Hatcher K. and Daanen H. Comparison of two tracer gas dilution methods for the determination of clothing ventilation and of vapour resistance. *Ergonomics* 2014; 53:548-558.
68. Ghaddar N. and Ghali K. Effect of moisture transport on mixed convection in vertical annulus of a heated clothed vertical wet cylinder in uniform cross wind In :14th International Heat Transfer Conference, 2010. Washington, DC; United States.
69. Ismail N., Ghaddar N. and Ghali K. Predicting segmental and overall ventilation of ensembles using an integrated bioheat and clothed cylinder ventilation models. *Textile Research Journal* 2014; 84 :2198-2213.
70. Ghaddar N., Ghali K. and Jreije B. Ventilation of wind-permeable clothed cylinder subject to periodic swinging motion: Modeling and experimentation. *J. Heat Transfer* 2008;130: 1107-2020.

71. Kind R., Jenkins J. and Seddigh F. Experimental investigation of heat transfer through wind-permeable clothing. *Cold region Science and technology* 1991; 20: 39-49.
72. Ghali K., Othmani M., Jreije B. and Ghaddar N. Simplified heat transport model of a wind-permeable clothed cylinder subject to swinging motion *Textile Research Journal* 2009; 79: 1043-1055.
73. Ghaddar N., Ghali K., Harathani J., and Jaroudi E. Ventilation rates of microclimate air annulus of the clothing skin system under periodic motion. *Int. J. of Heat and Mass Transfer* 2005; 48: 3151-3166.
74. Ghaddar N., Ghali K., and Chehaitly S. Assessing thermal comfort of active people in transitional spaces in presence of air movement. *Energy and Buildings* 2011;43: 2832-2842.
75. Al-Othmani M., Holmer I., Kuklane K., Ghaddar N. and Ghali K. Experimental and theoretical study of ventilation and heat loss from isothermally heated clothed vertical cylinder in uniform flow field. *J. Appl. Mech.* 2010; 77 : 031011-8.
76. Leong J. and Lai F. Natural Convection in a Concentric Annulus with a Porous Sleeve. *Int. Journal of Heat and Mass Transfer* 2006; 49 : 3016-3027. [14] ANSYS Software: ANSYS Inc. <http://www.ansys.com/>
77. Ke Y., Havenith G., Zhang X., Li X. and Li J. Effects of wind and clothing apertures on local clothing ventilation rates and thermal insulation, *Textile Research Journal* 2014;84:941-952.
78. Alam M., Moriya M., Takai K. and Sakamoto H. Fluctuating fluid forces acting on two circular cylinders in a tandem arrangement at a subcritical Reynolds number. *Journal of Wind Engineering Industrial Aerodynamics* 2003; 91:139-154.
79. Xu S., Zhou Y. and So R. Reynolds number effects on the flow structure behind two side-by-side cylinders. *Phys. Fluids* 2003; 15:1214-1219.
80. Bearman P.W. The effect of base bleed on the flow behind a two-dimensional model with a blunt trailing edge. *The Aeronautical Quarterly* 1967; 18 : 207-224.
81. Wood C. Visualization of an incompressible wake with base bleed. *Journal of Fluid Mechanics* 1967; 29 :259-272.
82. Ko N., Wong P. and Leung R. Interaction of Flow Structures within bistable flow behind two circular cylinders of different diamters. *Experimental Thermal and Fluid Science* 1996; 12:33-44.

83. Gao Y., Etienne S., Wang X. and Tan S. K. Experimental study on the flow around two tandem cylinders with unequal diameters. *J. Ocean Univ.* 2014; 13:761-770.
84. Zhao M. and Yan G. Numerical simulation of vortex-induced vibration of two circular cylinders of different diameters at low Reynolds number. *Physics of fluids* 2013; 25 .
85. Ghali K., Ghaddar N. and Jones B. Empirical evaluation of convective heat and moisture transport coefficients in porous cotton medium. *ASME heat transfer journal* 2002; 124:530-537.
86. Ghaddar N., Ghali K. and Harathani J. Modulated air layer heat and moisture transport by ventilation and diffusion from clothing with open aperture. *J. heat transfer journal* 2005; 127:287-297.
87. Chaves C., Camargo J. and Correa V. Combined forced and free convection heat transfer in a semi-porous open cavity. *Scientific Research and Essay* 2008; 3: 332-337.
88. ASHRAE. *ASHRAE Handbook-Fundamentals*, Atlanta GA:ASHRAE, 1997.
89. Stuart I.D. Wind induced transfer of water vapor and heat through clothing. *Textile Research Journal* 1987;57: 247-256.
90. Anil L.S. and Reji C. Numerical prediction of natural convection in vented cavities using restricted domain approach. *Int J Heat mass Tran.* 2009; 52: 724-734.
91. Malone T. and Parr A.D. Bend losses in rectangular culverts, Report No. K-TRAN: KU-05-5, Kansas State University and University of Kansas, Kansas, 2008.
92. Pletcher R., Tannehill J.C. and Anderson D.A. *Computational Fluid Mechanics and Heat Transfer*, Philadelphia: Taylor & Francis, 1997
93. Blazek J. *Computational Fluid Dynamics: Principles and Applications*, Second Edition, Elsevier, New York, 2005.
94. Nakamura M., Yoda T., Crawshaw L., Yasuhara S., Saito Y., Kasuga M., Nagashima K., and Kanosue K. Regional differences in temperature sensation and thermal comfort in humans. *Journal of Applied Physiology* 2008; 105: 1897-1906
95. Caroline J., Havenith G. Body mapping of sweating patterns in male athletes in mild exercise-induced hyperthermia. *Journal of Applied Physiology* 2011; 111: 1391-1404
96. Ouzzahra Y., Havenith G., Redortier B. Regional distribution of thermal sensitivity to cold at rest and during mild exercise in males. *Journal of Thermal Biology* 2012; 37: 517-523

97. Gerett N., Ouzzahra Y., Coleby S., Hobbs S., Redortier B., Voelcker T., Havenith G. Thermal sensitivity to warmth during rest and exercise: a sex comparison. *European Journal of Applied Physiology* 2014; 114: 1451-1462
98. Crockford G.W., Crowder M., Prestidg S.P. Trace gas technique for measuring clothing microclimate air exchange rates. *British Journal of Industrial Medicine* 1972; 29: 378-386.
99. Lotens W.A., Havenith G. Ventilation of rainwear determined by a trace gas method. *Environmental Ergonomics* 1988; 162-175
100. Ueda H., Inoue Y., Matsudaira M., Araki T. and Havenith G. Regional microclimate humidity of clothing during light work as a result of the interaction between local sweat production and ventilation. *International Journal of Clothing Science and Technology* 2006; 18: 225-234.
101. Satsumoto Y., Takeuchi M., Habu C. Yoshizaki, A. Development of device to evaluate the ventilation of diaper. *Proceedings of Korea-Japan Joint Symposium on Human-Environment System, Cheju, Korea, November, 2008.*
102. Ghaddar N, Ghali K, Othmani M, Holmer I and Kuklane K. Experimental and Theoretical Study of Ventilation and Heat Loss from Clothed Vertical Isothermally-Heated Cylinder in Uniform Flow Field. *ASME Journal of Applied Mechanics* 2010; 77: 1-8.
103. Ismail N, Ghaddar N and Ghali K. Effect of Inter-segmental Air Exchanges on Local and Overall Clothing Ventilation. *Textile Research Journal* 2015; 0(00):1-17.
104. Salloum M, Ghaddar N and Ghali K. A new transient bioheat model of the human body and its integration to clothing models. *International Journal of Thermal Sciences* 2007; 46: 371-384.
105. Burke R and McGuffin R. Development of an advanced thermal manikin for vehicle climate evaluation. In: *Proceedings of 4th international meeting on thermal manikins, 2001, pp.14-18.*
106. Blood K and Burke R. Further Validation of the model-controlled Newton thermal manikin against historical human studies. In: *Proceedings of the 8th International Meeting for Thermal Manikin and Modeling (8I3M), Victoria, Canada. 2010.*
107. Yang J, Wenguo W., and Ming F. A coupling system to predict the core and skin temperatures of human wearing protective clothing in hot environments. *Applied Ergonomics* 2015; 51: 363-369.

108. Sherman M. Tracer-gas techniques for measuring ventilation in a single zone. *Building and Environment* 1990; 25: 365-374.
109. Nakamura M, Yoda T, Crawshaw L, Yasuhara S, Saito Y, Kasuga M and Nagashima K. Regional differences in temperature sensation and thermal comfort in humans. *Journal of Applied Physiology* 2008; 105: 1897-1906.
110. Caroline J and Havenith G. Body mapping of sweating patterns in male athletes in mild exercise-induced hyperthermia. *Journal of Applied Physiology* 2011; 111: 1391-1404.
111. Ouzzahra Y, Havenith G and Redortier B. Regional distribution of thermal sensitivity to cold at rest and during mild exercise in males. *Journal of Thermal Biology* 2012; 37: 517-523.
112. Gerett N, Ouzzahra Y, Coleby S, Hobbs S, Redortier B, Voelcker T and Havenith G. Thermal sensitivity to warmth during rest and exercise: a sex comparison. *European Journal of Applied Physiology* 2014; 114: 1451-1462.
113. Ke ,Y., Havenith, G., Zhang, X., Li, X. and Li J. 2014, "Effects of wind and clothing apertures on local clothing ventilation rates and thermal insulation", *Textile Research Journal*, 84, pp. 941-952.
114. Birnbaum, R.R., and Crockford, G.W. 1978, "Measurement of the clothing ventilation index", *Applied Ergonomics*, 9, pp. 194-200.
115. Lotens, W. 1993 Heat transfer from humans wearing clothing, Doctoral thesis, TNO Institute for Perception, Soesterberg, The Netherlands.
116. Ghaddar, N. ,Ghali, K, and Othmani, M. 2010, "Effect of Moisture Transport on Mixed Convection in Vertical Annulus of a Heated Clothed Vertical Wet Cylinder in Uniform Cross Wind". *Proceedings of 14th International Heat Transfer Conference (IHTC14)*, Washington D.C. August 7-13 in 2010. Paper Number: IHTC14-22342.
117. Ghaddar, N., Ghali, K. M. Al-Othmani, K. , Holmer, I., Kuklane, K. 2010, "Experimental and theoretical study of ventilation and heat loss from isothermally heated clothed vertical cylinder in uniform flow field" *Journal of Applied Mechanics*, 77, pp. 031011.
118. Ismail, N., Ghaddar, N. and Ghali, K., 2016. "Effect of inter-segmental air exchanges on local and overall clothing ventilation". *Textile Research Journal*, 86(4), pp.423-439.

119. Ismail, N., Ghaddar, N. and Ghali, K., 2016. "Improving Local Ventilation Prediction by Accounting for Inter-segmental Ventilation Rate". *Textile Research Journal*, 00 pp.1-17.
120. Ismail, N. Ghaddar, N. and K. Ghali, 2014. "Predicting segmental and overall ventilation of ensembles using an integrated bioheat and clothed cylinder ventilation models". *Textile Research Journal*, 84 (2014) 2198–2213.
121. Ghaddar, N. , Ghali, N. , Al-Othmani, M. , Holmer, I., Kuklane, K. 2010"Experimental and theoretical study of ventilation and heat loss from isothermally heated clothed vertical cylinder in uniform flow field" *Journal of Applied Mechanics*. 77 pp. 031011
122. Itani, M. , Ouahrani, D. , Ghaddar, N. Ghali, K. Chakroun, W. 2016. "[The effect of PCM placement on torso cooling vest for an active human in hot environment]", *Building and Environment*. 107 pp.29–42.
123. Itani, M. , Ghaddar, N. , Ghali, K., Ouahrani, D. , Chakroun, W. 2017 "Cooling vest with optimized PCM arrangement targeting torso sensitive areas that trigger comfort when cooled for improving human comfort in hot conditions" *Energy and Buildings*. 139 pp. 417–425.
124. Zhang, H. 2003. "Human thermal sensation and comfort in transient and non-uniform thermal environments", dissertation.
125. Cotter, J.D. Taylor, N.A.S, 2005. "The distribution of cutaneous sudomotor and alliesthesial thermosensitivity in mildly heat-stressed humans: an open-loop approach". *The Journal of Physiology*. 565 pp. 335–345.
126. Norfin, <http://www.norfin.info/norfin-verity-review/>
127. Arcteryx
<http://www.arcteryx.com/product.aspx?country=lb&language=en&gender=mens&model=Norvan-Jacket>
128. Sierra Design Stretchs, <http://www.outdoorgearlab.com/Rain-Jacket-Womens-Reviews/Sierra-Designs-Stretch-Womens>
129. Gerarde, H.W., 1960. *TEXTBOOK OF TOXICOLOGY*. *Journal of Occupational and Environmental Medicine*, 2(8), pp.402-403.
130. Ismail, N. Ghaddar, N., Ghali, K. 2016. "Determination of segmental and overall ventilation of clothed walking human by means of electric circuit analogy". *Textile Research Journal*. Accepted for publication.

131. Ismail, N. Ghaddar, N. and Ghali, K. 2017, “A clothing ventilation and heat loss electric circuit model for a walking human”. *International Journal of Thermal Sciences* 2017, under review.
132. Ghali, K., Othmani, M. , Jreije, B., Ghaddar, N. 2009. “Simplified heat transport model of a wind-permeable clothed cylinder subject to swinging motion” *Textile Research Journal*, 79, pp. 1043–1055.
133. Ghaddar, N., Ghali, K., Harathani, J. and Jaroudi, E., 2005. “Ventilation rates of micro-climate air annulus of the clothing-skin system under periodic motion”. *International Journal of Heat and Mass Transfer*, 48(15), pp. 3151-3166.
134. Meyns, P., Bruijn, S.M. , Duysens, J., 2013. “The how and why of arm swing during human walking”. *Gait & Posture*, 38, pp. 555–562.
135. American Society for Testing and Materials. ASTM D737-75, Standard test method for air permeability of textile fabrics, (IBR) approved 1983.
136. Fransson, J. , Konieczny, P. Alfredsson, P. 2004. “Flow around a porous cylinder subject to continuous suction or blowing”, *Journal of Fluids and Structures*. 19 pp. 1031–1048.
137. Lotens, W.A., Havenith, G. 1991. “Calculation of clothing insulation and vapor resistance”, *Ergonomics*. 34 pp. 233–254.
138. U. Danielsson, Convection coefficients in clothing air layers, P.h.D. dissertation, 1993.
139. WA. Lotens 1993. Heat transfer from humans wearing clothing. Soesterberg, Netherlands: TNO-Institute for Perception, PhD dissertation.
140. Burke R and McGuffin R. 2011. “Development of an advanced thermal manikin for vehicle climate evaluation”. In: *Proceedings of 4th international meeting on thermal manikins*, pp.14-18.
141. Y, Ke , Li J and Havenith G. 2014. “An improved experimental method for local clothing ventilation measurement”. *International Journal of Industrial Ergonomics* 44 pp. 75-81.
142. A. Mohanty, M. Dubey, Buoyancy induced flow and heat transfer through a vertical annulus, *International Journal of Heat and Mass Transfer*. 39 (1996) 2087–2093.
143. N., Galanis, A., Behzadmehr, Mixed convection in vertical ducts. In *Proceedings of 6th IASME/WSEAS International Conference on Fluid Mechanics and Aerodynamics*, Rhodes, Greece, 2008: pp. 35-43.

144. Ozkok, U.; Icoğlu, H. I.; Kirecci, A. *J. Mater. Sci. Eng.* **2011**, *5*, 227-280.